2011

Exotic Ground States: A Study in the Structural Effects on Frustration and Dimensionality

Melissa C. Menard
Louisiana State University and Agricultural and Mechanical College, mmenard81@gmail.com

EXOTIC GROUND STATES:
A STUDY IN THE STRUCTURAL EFFECTS ON FRUSTRATION AND DIMENSIONALITY

A Dissertation

Submitted to the Graduate Faculty of the
Louisiana State University and
Agricultural and Mechanical College
in partial fulfillment of the
requirements for the degree of
Doctor of Philosophy

in

The Department of Chemistry

by
Melissa C. Menard
B.S., University of Louisiana at Lafayette, 2005
December 2011

ACKNOWLEDGEMENTS

Above all I thank God, for without whom all would be meaningless. I would also like to thank my family. My father never let anything slide. My mother always wanted the best for me and supported me through thick and thin. My brothers taught me the value of a good argument, so I learned to defend myself early in life. My grandmother, in all her wisdom, told me to read everything I could. To the rest of my very large, extended family, thanks for all your support throughout the years.

I would like to acknowledge my academic family. I would like to especially thank my mentor, Dr. Julia Chan, for accepting nothing but the best from me in research and in life. She has always pushed me to greater heights by continually asking thoughtful questions. As a solid state materials scientist, she has been a shining example for me. I hope she knows how much I appreciate the all unique opportunities she laid in my path. From the conferences in Bangalore, India and Madrid, Spain to the science fair judging at local schools, I have experienced the sense of accomplishment that comes from presenting one's work but also from working with young scientists.

I would like to thank my committee members for all their prodding and support. Especially Dr. George Stanley, Dr. David Young, and Dr. Andrew Maverick, I would like to thank for all the reference letters written for me, without which my research and I would have been trapped inside the confines of LSU. I would like to thank my academic uncle, Dr. Frank Fronczek, not only for sharing his boundless knowledge of crystal structure determination but also for his patience. Without the work of Dr. Nakatsuji Satoru, Dr. Rieko Ishii, Dr. David Young, Dr. John DiTusa, Dr. Amar Karki, Dr. Neel Haldolaarachchige, Dr. Phil Adams, and Dr.

Yimin Xiong, the physical property measurements and structure-property correlations of my single crystals would not have been possible.

A pleasant working environment made the years of research at LSU pass in an instant. For coffee at the union, I would especially like to thank my academic brothers Devin, Brad, and Gregory. For insightful discussions, careful editing, and cheerful collaboration, I would like to thank Gregory McCandless. For enlightening discussions, I would like to thank Brenton, Adam, and Michael. To my protégé, Kristin, I would like to thank for all her thoughtful questions and hard work. She will be a shining star in a sea of mundane complacency. For their knowledge of the German, Russian, and French languages, I would like to thank Darina Schelonka, Ekaterina Kalashnikova, and Adrien Connangle, respectively.

Most importantly, I would like to thank my husband, Wesley J. Menard, for supporting me through late night experiments, long conferences, and the craziness that comes from marrying a very unique, eclectic, and driven individual. This achievement is as much his as it is mine.

TABLE OF CONTENTS

LIST OF TABLES

LIST OF FIGURES

ABSTRACT

Structural disorder and dimensionality play central roles in the characterization of structure and properties of crystalline materials. Although structural disorder is commonly considered an undesirable quality, structural disorder may be desirable when searching for new materials with exotic properties. Disorder can be used as a tunable parameter when considering atomic sizes, coordination preferences, and electronegativity differences can be varied by substituting elements into a given structure. Dimensionality can be viewed as another adjustable parameter when searching for new materials presenting unique challenges when characterizing new materials. One way to tune dimensionality is by chemical doping to affect coupling between layers/chains. The growth of phases with inherent structural disorder often involves tuning at the edge of structural stability which necessitates careful adjustment of synthetic parameters and presents unique characterization challenges. Understanding the effects of disorder and dimensionality could lead to better understanding of complex behavior.

Many materials with exotic magnetic ground states exhibit magnetic frustration in one form or another. Magnetic frustration is a term which loosely describes the suppression of long-range magnetic ordering to temperatures much lower than the Weiss temperature in phases with magnetic correlations. Three parameters linked to magnetic frustration include: geometry of the magnetic sublattice, site disorder, and the effective dimensionality of the magnetic sublattice. Often these three parameters are inseparable in real systems, and investigating the fundamental differences between these geometrical frustration, structural disorder, and dimensionality would be of significant interest. This dissertation presents the growth, structure, and properties of single crystals of 3-*d* structurally disordered intermetallic phases $Ln_2Ag_{1-x}Ga_{10-y}$ (*Ln* = La, Ce) and β-*Ln*$NiGa_4$ (*Ln* = Tb-Er), 2-*d* frustrated spin glasses MAl_2S_4 (*M* = Mn, Fe, Co, Ni), and

quasi-1-*d* quantum, antiferromagnet $K_4Cu(MoO_4)_3$ to highlight the effects of structural disorder and dimensionality on magnetic ground states.

CHAPTER 1. INTRODUCTION

1.1 Single Crystal Growth and the Search for Exotic Ground States

The search for new materials is ultimately driven by the desire to discover exotic behavior. Careful structure determination of new, exotic materials is necessary to investigate emergent phenomena, which are due to the interaction of many parameters and cannot be understood by considering the each parameter individually. Synthesizing and characterizing new materials support problem driven research as opposed to technique driven research. By focusing on the problem, instead of focusing on specific techniques, materials growth and characterization is not limited by the given technique. This holistic approach yields many opportunities to discover new phenomena.

The search for new materials is not a game of darts targeted towards the periodic table, but more akin to fishing in an area known to be filled with interesting possibilities.[1-2] Although discovery often happens serendipitously, the search for emergent behavior is made simpler by deriving generalizations from examples which exhibit desired behavior. By comparing families of structurally related materials, a knowledge-base is built from which correlations between structural parameters, such as structural motifs, dimensionality, site disorder, and structural distortion, can be correlated to behavior. The comparison of these structurally-related materials may help in directing the growth of new materials.

To improve our understanding of the exotic properties associated with multifunctional materials, the growth of high quality single crystals from which detailed structure-property relationships can be elucidated is vital. Crystal growth methods of solid state inorganic materials are varied with the choice determined not only by the chemical properties but also by the physical properties of the desired material. High temperature methods, such as solid state reaction methods, are defined by the application of very high reaction temperatures (~3000 °C)

over short time scales, which necessitate successive grinding to allow for sufficient diffusion of reactants and to increase the reactant surface area for a reaction to take place. These "beat and heat" methods are not conducive to single crystal growth but yield polycrystalline material.[3]

The flux growth method has been utilized in the growth of many classes of materials including intermetallic phases and oxides. Melt methods, such as the flux growth technique, overcome the slow diffusion of reactants and homogenize the reaction mixture by using molten solids as solvents. The melting point depression that results from the combination of the flux with the other reactant metals allows for the search for new materials at intermediate temperatures. Therefore flux growth reactions generally involve lower reaction temperatures (~ 1000 °C). The flux can also be used as one of the components of the desired phase (reactive flux) which is termed the self-flux method.[4-5]

Vapor phase transport methods are often used in the synthesis of chalcogenides and halides.[6] These methods have been successful for the purification of known compounds, for the growth of single crystals from a polycrystalline precursor via a volatile intermediate, and for the discovery of new compounds. The chemical vapor transport method employs a transport agent, such as Cl_2 or I_2, with reactants typically placed in an evacuated fused-silica ampoule. Transport reactions are carried out in a temperature gradient for ~weeks using a transport agent concentration of 3 mg/cm^3 iodine.

Regardless of the crystal growth method employed, the factors affecting the crystal quality can be classified as either extrinsic or intrinsic effects. Extrinsic effects, such as grain boundaries, are not inherent to a phase and can be attributed to growth conditions or mechanical treatment. One extrinsic parameter which measures crystal quality is mosaicity, the degree of alignment among grains (domains of unit cells) in a crystal. Intrinsic effects, on the other hand,

are due to the chemistry of the phase under investigation. Since both extrinsic and intrinsic effects can significantly impact the physical properties of a material, high quality single crystals are necessary to study intrinsic structure-property correlations.

1.2 Structure Determination by X-ray Diffraction

X-rays are generated when a high energy electron beam (55 keV for a Mo target) strikes a metal target. The subsequent rapid deceleration of the electrons produces mostly heat and electromagnetic radiation consisting of < 1 % of polychromatic X-rays. The ejection of an inner shell electron from an atom of the metal target results in an electron vacancy and leaves the atom in an excited state. The atom returns to the ground state by movement of a higher energy electron into the vacancy. To release the excess energy due to the movement of a higher energy electron falling into a lower energy state, an atom can release X-rays with a wavelength characteristic of the metal target or an electron (Auger effect) with energy equal to the energy difference between the two states. For the characterization of crystalline materials with atomic number greater than 31, the emission of Auger electrons, as compared to X-rays, is not significant.[7]

When X-rays interact with electrons in a material, the X-rays are scattered in all directions. Scattered X-ray beams interact constructively or destructively depending on the difference between the distances traveled by two/more X-rays from the X-ray source to the detector. When the difference between the distances traveled by two or more scattered X-rays equals an integral number of the wavelength, the X-rays interact constructively with an intensity proportional N^2A^2 (where N is the number of scattered rays and A is the amplitude of the scattered X-rays). This can be mathematically described by Bragg's law $n\lambda = 2d\sin\theta$. n is the order of diffraction, λ is the wavelength ($Å^{-1}$) of incoming X-rays, d is the spacing (Å) between

lattice planes, and θ is the angle of incidence/reflection. The reinforcement of the scattered X-ray beam due to the periodicity of the electrons in a crystal results in an *N*-fold increase in the intensity of the scattered beam as compared to the scattering expected for noncrystalline materials. The reinforced, scattered X-rays observed in symmetrically unique directions produce an array of bright "reflections" known as a diffraction pattern.[7] Therefore X-rays are used to "see" the atoms in a crystalline material.

Structure determination by X-ray diffraction (XRD) has been hailed as the ultimate analytical technique for structure determination. The symmetry of the unit cell is determined by the symmetry of the diffraction pattern, the dimensions of the unit cell are determined by the spacing of the reflections, and the identity and position of the atoms are determined by the intensity and position of the reflections. The interatomic distances and angles, as determined by the refined structural model, lend insight to the nature of the interactions between atoms (ions). However powder and single crystal X-ray diffraction provide only an average picture of the crystal structure. The structure of many interesting compounds lacks the usual periodic order. Structural disorder can be attributed to anomalies observed at specific crystallographic sites (site disorder) in a crystal structure or may extend systematically throughout the structure. The characterization of structurally disordered crystals is driven by determining the nature of the disorder and understanding the structural effects of disorder on physical properties. Understanding interactions at the local environment may illuminate the nature of the structural disorder which is necessary to correlate crystal structure to physical properties.

1.3 Challenges in the Characterization of Complex Crystal Structures

Site disorder is defined as the deviation at specific crystallographic sites from an ordered atomic arrangement in a crystalline material and has intrinsic effects on physical properties.

Although by definition site disorder is associated with specific crystallographic sites, disorder at one site will perturb the atoms in the immediate surroundings. The nature of site disorder can be classified by whether or not the disorder is due to physical motion in a crystal, known as dynamic disorder.[8] Statistical disorder can be classified as either the statistical distribution of one atom/ion at different crystallographic sites in a unit cell (positional disorder) or the statistical occupation of the same crystallographic site by different types of atoms/ions (substitutional disorder).[8] Disordered structures often exhibit both dynamic and statistical disorder which is manifested as diffuse disorder scattering in the X-ray diffraction patterns with smeared, unusually shaped, or directionally oriented reflections. Although the distinction between dynamic and static disorder is not always clear, the degree of dynamic and statistical disorder present in a crystal structure can be probed by comparing the refined structural models of both high and low temperature data collections.[8] The best-fit model of a dynamically disordered structure will not be significantly affected the by thermal fluctuations, and both high and low temperature structural models will be indistinguishable. The best-fit model of a statistically disordered structure may be affected by thermal fluctuations, and differences in the structural models may be observed at different temperatures.

Structural disorder which extends beyond specific crystallographic sites may be observed as split peaks in X-ray and electron diffraction patterns. The presence of characteristic satellite peaks, which cannot be indexed to the unit cell as determined by the main reflections, could indicate twinning, superlattice formation, or structural modulation. The split reflections due to twinning may be indexed as a separate component(s) and result from the mutual orientation of each twin component.[8] Structure determination of a twinned crystal requires the determination of the twin law(s), a symmetry operation that brings the split peaks into coincidence with the

main reflections characteristic of the unit cell, and the determination of the fractional contribution from each twin component.

The difference between twinning and superlattice formation or structural modulation can be attributed to the symmetry of the non-integral peaks in a diffraction pattern. The observation of weak satellite peaks in a diffraction pattern, due to the long-range ordering of specific atoms or motifs in a structure can be attributed to superlattice formation or structural modulation.[8-9] Long-range ordering of specific atoms or motifs in a crystal structure results in overall lower symmetry of the diffraction pattern. A supercell is a multiple, not necessarily integral, of the subcell, which is determined from the symmetry of the strong reflections in the diffraction pattern. Structural modulation is observed as the presence of reflections along a particular direction which appear out-of-phase with the symmetry of the unit cell as determined by the main reflections and is characterized as a four dimensional repeating pattern in three-dimensional space. [8-9] The difference between structural modulation and superlattice formation is illustrated by the relationship between the strong peaks and the weak peaks in the diffraction pattern. The symmetry of the weak peaks in a diffraction pattern, due to the presence of a supercell, can be modeled by in three-dimensional space whereas structural modulation requires the application of a four dimensional point group.

Often these warning signs, diffuse disorder scattering or satellite peaks, observed in X-ray diffraction experiments are very weak which make probing the nature of the structural disorder challenging. Usually the satellite peaks, due to supercell formation or structural modulation, are not of sufficient intensity to accurately measure with in-house X-ray diffraction methods. Although the presence of a supercell and structural modulations are difficult to accurately measure with XRD methods, the manifestation of structural disorder is evident as

anomalous atomic displacement parameters, unrealistic interatomic distances, and unusual residual electron density peaks. Complete structural elucidation of complex materials is necessary to probe the nature of the disorder and to determine structure-property relations since properties are determined by the relative positions of atoms which are close enough to interact. Through comparison with known structures, we use our own chemical intuition to guide our interpretation of the local interactions that yield the overall crystal structure from which correlations between structure and properties can be drawn for complex materials.

1.4 The Search for Emergent Phenomena by Investigation of Frustration

Magnetism is often correlated with other interactions in a material, where coupling between spin, orbital, and/or lattice parameters, makes predicting behavior a complex task. The study of low-temperature magnetic behavior allows for fundamental understanding of magnetic ground states which ultimately affects interactions at application temperatures. A viable method in the search for exotic magnetic ground states centers on investigating the interplay of competing interactions on the overall magnetic state of a material.

Many materials with exotic magnetic ground states exhibit frustration in one form or another. Frustration is a term which loosely describes the suppression of long-range magnetic ordering to temperatures much lower than the Weiss temperature in phases with magnetic correlations.[10-12] There are three parameters linked to magnetic frustration: the geometry of the magnetic sublattice, site disorder, and the effective dimensionality of the magnetic sublattice. Often these three parameters are inseparable in real systems. Investigating the fundamental differences between geometrical frustration, site disorder, and dimensionality and the resulting emergent phenomena would be of significant interest. My research involves the growth and characterization of three seemingly different types of materials: ternary intermetallics, frustrated

sulfides, and low dimensional oxides which highlight the complex interplay of geometrical frustration, site disorder, and dimensionality on magnetic and transport properties.

1.5 Three Dimensional Distorted Intermetallics

Ternary intermetallic compounds of *Ln : M : X* (*Ln* = lanthanide; *M* = transition metal; *X* = main group metal) are good candidates for highly correlated electronic behavior, such as materials that exhibit heavy fermion behavior, large magnetoresistance, magnetically mediated superconductivity, and ferromagnetically ordered materials. Several ternary phases of Ce-*M*-Ga (*M* = Ni, Pd, Cu) have been reported exhibiting heavy fermion antiferromagnetism and large magnetoresistance.[13-19] The idea is to build structurally similar compounds by substituting metals and/or structural motifs found in materials with interesting behavior. Novel materials are expected due to differing coordination preferences, electronegativities, and atomic sizes among transition metals. In Chapters 2 and 3, the growth, structure and properties of defect variants of the Ce_2NiGa_{10} structure type, $Ce_2Ag_{1-x}Ga_{10-y}$[20] and β–*Ln*$Ni_{1-x}Ga_4$ (*Ln* = Tb-Er)[21] are reported and compared to investigate the effects of site disorder on magnetic frustration.

1.6 Two Dimensional Spin Glasses

Primary interest in two-dimensional (2-*d*) triangular lattice antiferromagnets arises from the inherent lattice frustration resulting in the suppression of long range magnetic order to temperatures much lower than expected due to competing interactions between magnetic moments.[10, 22-24] The combination of frustration and 2-*d* magnetism can suppress magnetic ordering and allow for the investigation of the quantum fluctuations that determine the possible ground states of the system.[25] The recently reported, $NiGa_2S_4$, is the first S= $^1/_2$ antiferromagnet with Ni^{2+} moments on an exact 2-*d* triangular sublattice and exhibits unusual spin glass behavior.[24, 26] Together the $NiGa_2S_4$ and $FeGa_2S_4$ phases serve as examples of frustration due to

the geometry of the 2-*d* magnetic sublattice without site disorder.[24, 26] In Chapter 4, the structures of the Al-analogues, MAl$_2$S$_4$ (M^{2+} = Mn^{2+}, Fe^{2+}, Co^{2+})[27] and Ni$_{0.68(1)}$Al$_2$S$_{3.78(1)}$[28] are discussed and compared to highlight the effects of site disorder, two-dimensionality, and geometrical frustration on the magnetic ground states.

1.7 One Dimensional Quantum Magnets

The low dimensionality and quantum fluctuations found in quantum magnets with S = $^1/_2$ and S = 1 present a unique opportunity to discover new states of matter. Spin-$^1/_2$ quantum magnets present the simplest models for the study of low dimensional materials with enhanced quantum fluctuations. The structure and properties of $K_4Cu(MoO_4)_3$ are discussed in Chapter 5 as well as a comparison of the quasi-1-*d* quantum antiferromagnets, $A_4Cu(MoO_4)_3$ (A = K, Rb),[29-30] to study the effects of structural distortion and one-dimensionality on magnetic behavior.

1.8 References

(1) Canfield, P. C., Fishing the Fermi sea. *Nat. Phys.* **2008,** *4*, 167-169.

(2) Canfield, P. C., A cook's tale. *Nat. Phys.* **2009,** *5*, 529-530.

(3) Canfield, P. C., High-temperature solution growth of intermetallic single crystals and quasicrystals. *J. Cryst. Growth* **2001,** *225*, 155-161.

(4) Canfield, P. C.; Fisk, Z., Growth of single crystals from metallic fluxes. *Philos. Mag. B.* **1992,** *65*, 1117-1123.

(5) Kanatzidis, M. G., The metal flux: a preparative tool for the exploration of intermetallic compounds. *Angew. Chem. Int. Ed. Engl.* **2005,** *44*, 6996-7023.

(6) West, A. R., *Basic Solid State Chemistry*. 2nd ed.; John Wiley & Sons Inc: West Sussex, **1999**.

(7) Cullity, B. D., *Elements of X-ray Diffraction*. 2nd ed.; Addison-Wesley Publishing Company, Inc.: Reading, Massachusetts, **1978**.

(8) Giacovazzo, C., *Fundamentals in Crystallography*. 2nd ed.; Oxford University Press.: Oxford, **2002**.

(9) de Wolf, P. M., The pseudo-symmetry of modulated crystal structures. *Acta Crystallogr. A.* **1974,** *30*, 777-785.

(10) Greedan, J. E., Frustrated rare earth magnetism: spin glasses, spin liquids and spin ices in pyrochlore oxides. *J. Alloys Compd.* **2006,** *408-412*, 444-455.

(11) Ramirez, A. P., Strongly geometrically frustrated magnets. *Annu. Rev. Mater. Sci.* **1994,** *24*, 453-480.

(12) Binder, K.; Young, A. P., Spin glasses: experimental facts, theoretical concepts, and open questions. *Rev. Mod. Phys.* **1986,** *58*, 801-976.

(13) Macaluso, R. T.; Nakatsuji, S.; Lee, H.; Fisk, Z.; Moldovan, M.; Young, D. P.; Chan, J. Y., Synthesis, structure, and magnetism of a new heavy-fermion antiferromagnet, $CePdGa_6$. *J. Solid State Chem.* **2003,** *174*, 296-301.

(14) Millican, J. N.; Macaluso, R. T.; Young, D. P.; Moldovan, M.; Chan, J. Y., Synthesis, structure, and physical properties of Ce_2PdGa_{10}. *J. Solid State Chem.* **2004,** *177*, 4695-4700.

(15) Macaluso, R. T.; Millican, J. N.; Nakatsuji, S.; Lee, H.-O.; Carter, B.; Moreno, N. O.; Fisk, Z.; Chan, J. Y., A comparison of the structure and localized magnetism in Ce_2PdGa_{12} with the heavy fermion $CePdGa_6$. *J. Solid State Chem.* **2005,** *178*, 3547-3553.

(16) Cho, J. Y.; Millican, J. N.; Capan, C.; Sokolov, D. A.; Moldovan, M.; Karki, A. B.; Young, D. P.; Aronson, M. C.; Chan, J. Y., Crystal growth, structure, and physical properties of Ln_2MGa_{12} (*Ln* = La, Ce; *M* = Ni, Cu). *Chem. Mater.* **2008,** *20*, 6116-6123.

(17) Cho, J. Y.; Moldovan, M.; Young, D. P.; Lowhorn, N. D.; Chan, J. Y., Physical properties of $LnAg_yX_{4-y}$ (*Ln* = La, Ce; *X* = Al, Ga; *y* = 0.72). *Physica B* **2008,** *403*, 795-796.

(18) Cho, J. Y.; Thomas, E. L.; Nambu, Y.; Capan, C.; Karki, A. B.; Young, D. P.; Kuga, K.; Nakatsuji, S.; Chan, J. Y., Crystal growth, structure, and physical properties of $Ln(Cu,Ga)_{13-x}$ (*Ln* = La-Nd, Eu; $x \sim 0.2$). *Chem. Mater.* **2009,** *21*, 3072-3078.

(19) Thomas, K. R.; Cho, J. Y.; Millican, J. N.; Hembree, R. D.; Moldovan, M.; Karki, A.; Young, D. P.; Chan, J. Y., Crystal growth and physical properties of Ln_2MGa_{12} (*Ln* = Pr, Nd, and Sm; *M* = Ni, Cu). *J. Cryst. Growth* **2010,** *312*, 1098-1103.

(20) Menard, M. C.; Xiong, Y.; Karki, A. B.; Drake, B. L.; Adams, P. W.; Fronczek, F. R.; Young, D. P.; Chan, J. Y., Synthesis, structure, and characterization of $Ln_2Ag_{1-x}Ga_{10-y}$ (*Ln* = La, Ce). *J. Solid State Chem.* **2010,** *183*, 1935-1942.

(21) Menard, M. C.; Drake, B. L.; Thomas, K. R.; Hembree, R. D.; Karki, A.; Li, Y.; Young, D. P.; Ditusa, J.; Zhang, J.; Chan, J. Y., A tale of two polymorphs: growth and characterization of α-$LnNiGa_4$ (*Ln* = Y, Gd-Yb) and β–$LnNi_{1-x}Ga_4$ (*Ln* = Tb-Er). *Eur. J. Inorg. Chem.* **2011,** *In Press.*

(22) Moessner, R.; Ramirez, A. P., Geometrical frustration. *Phys. Today* **2006,** *2006*, 24-29.

(23) Levi, B. G., New candidate emerges for a quantum spin liquid. *Phys. Today* **2007,** *2007*, 16-19.

(24) Nakatsuji, S.; Nambu, Y.; Tonomura, H.; Sakai, O.; Jonas, S.; Broholm, C.; Tsunetsugu, H.; Qiu, Y.; Maeno, Y., Spin disorder on a triangular lattice. *Science* **2005,** *309*, 1697-1700.

(25) Affleck, I. J., Quantum spin chains and the haldane gap. *J. Phys.-Condens. Mat.* **1989,** *1*, 3047-3072.

(26) Nakatsuji, S.; Tonomura, H.; Onuma, K.; Nambu, Y.; Sakai, O.; Maeno, Y.; Macaluso, R. T.; Chan, J. Y., Spin disorder and order in quasi-2d triangular heisenberg antiferromagnets: comparative study of $FeGa_2S_4$, $Fe_2Ga_2S_5$, and $NiGa_2S_4$. *Phys. Rev. Lett.* **2007,** *99*, 157203.

(27) Menard, M. C.; Ishii, R.; Higo, T.; Nakatsuji, S.; Nishibori, E.; Sawa, H.; Chan, J. Y., High-resolution synchrotron studies and magnetic properties of frustrated antiferromagnets $M Al_2S_4$ (M^{2+} = Mn^{2+}, Fe^{2+}, Co^{2+}). *Chem. Mater.* **2011,** *23*, 3086-3094.

(28) Higo, T.; Ishii, R.; Menard, M. C.; Chan, J. Y.; Yamaguchi, H.; Hagiwara, M.; Nakatsuji, S., Magnetic properties of the quasi-two-dimensional antiferromagnet $Ni_{0.7}Al_2S_{3.7}$. *Phys. Rev. B* **2011,** *In Press.*

(29) Ishii, R.; Gautreaux, D.; Onuma, K.; Machida, Y.; Maeno, Y.; Nakatsuji, S.; Chan, J. Y., Low-dimensional structure and magnetism of the quantum antiferromagnet $Rb_4Cu(MoO_4)_3$ and the structure of $Rb_4Zn(MoO_4)_3$. *J. Am. Chem. Soc.* **2010,** *132*, 7055-7061.

(30) Menard, M. C.; Ishii, R.; Onuma, K.; Nakatsuji, S.; Chan, J. Y., Structure and magnetism of the quasi-1-*d* $K_4Cu(MoO_4)_3$ and the structure of $K_4Zn(MoO_4)_3$. *Inorg. Chem.* **2011,** *Submitted*.

CHAPTER 2. CRYSTAL GROWTH AND PROPERTIES OF $Ln_2Ag_{1-x}Ga_{10-y}$ (*Ln* = La, Ce), A DEFECT VARIANT OF THE Ce_2NiGa_{10} STRUCTURE TYPE[*]

2.1 Introduction

Intermetallic phases with complex Ga-networks have been a popular subject due to the observation of a wide variety of exotic phenomena found in these systems: superconductivity in $PuCoGa_5$,[1-3] large magnetoresistance in Ln_4PtGa_{12} (*Ln* = Dy-Er),[4] heavy fermion behavior in $CePdGa_6$,[5] charge density wave formation in $LnCo_xGa_3Ge$ (*Ln* = Y, Gd),[6-7] spin density wave formation in $U_3Ga_2Si_3$,[8] the observation of zero thermal expansion of YbGaGe[9] and negative thermal expansion of $YbGa_{1+x}Ge_x$.[10] Identification of structural subunits associated with specific phenomena serves as a guide to focus crystal growth on targeted motifs in new materials likely to exhibit a desired property. In all cases novel materials and behaviors, with targeted motifs, are expected due to differing coordination preferences, electronegativities, atomic sizes, and disorder among transition metals.

We have recently grown and characterized single crystals of several ternary phases of Ce-*M*-Ga (*M* = Ni, Pd, Cu) and discovered unusual magnetic and electrical properties.[5, 11-16] $CePdGa_6$ is a heavy fermion antiferromagnet ($\gamma \sim 400$ mJ/mol-K^2)[5] with a layered structure of alternating face-sharing $CeGa_{8/4}$ rectangular prisms and staggered edge-sharing Pd rectangular prismatic layers, and is structurally similar to the magnetically mediated superconductors $CeMIn_5$ (*M* = Co, Rh, Ir).[17-19] The structural similarity of $CePdGa_6$ to the magnetically mediated superconductors $CeMIn_5$ (*M* = Co, Rh, Ir)[17-19] has driven the continued investigation of ternary systems of *Ln*:*M*:Ga (*Ln* = lanthanide, *M* = transition metal) to make connections between structural motifs and unique physical properties. Subsequent investigation resulted in the growth of antiferromagnetic Ce_2PdGa_{12}, which is an intergrowth of $CePdGa_6$- and CaF_2-type structure

[*]Reprinted by permission of Elsevier: Menard, M. C.; Xiong, Y.; Karki, A. B.; Drake, B. L.; Adams, P. W.; Fronczek, F. R.; Young, D. P.; Chan, J. Y., Synthesis, structure, and characterization of $Ln_2Ag_{1-x}Ga_{10-y}$ (*Ln* = La, Ce). *J. Solid State Chem.* **2010,** *183*, 1935-1942. "Copyright 2010 Elsevier."

segments, with Ce and Pd in rectangular prismatic environments and shows moderate heavy ($\gamma \sim$ 140 mJ/mol-K^2) fermion behavior.[12] A related phase, Ce_2PdGa_{10}, is paramagnetic down to 2 K, shows large magnetoresistance of 290 % at 9 T, and can be described as an intergrowth of $BaAl_4$- and CaF_2-type structure segments.[11] A copper analogue, Ce_2CuGa_{12},[13] exhibits large magnetoresistance up to 65 % at 9 T. The isostructural Ni-analogue, Ce_2NiGa_{12}, orders antiferromagnetically at 10 K and undergoes a metamagnetic transition at 3 T.[13]

Transition metal substitution led to the investigation of Ag-containing intermetallic compounds. Although the structure of several *Ln*:Ag:Ga (*Ln* = lanthanide) intermetallic compounds such as $Ln(Ag,Ga)_4$ (*Ln* = La - Nd, Sm, Yb),[20-21] $Ln_3(Ag,Ga)_{11}$ (*Ln* = Y, Gd -Yb),[22-23] *Ln*$AgGa_2$ (*Ln* = Gd, Yb, Y),[23-25] *Ln*AgGa (*Ln* = Tb - Ho),[26] $Ln(Ag,Ga)_2$ (*Ln* = La-Nd, Sm-Lu, Y),[23, 27-28] $Ln_5(Ag,Ga)_{19-x}$ (*Ln* = Gd, Tb; $x \sim 2.2$),[29] $CeAg_{4.12}Ga_{6.88}$,[30] $CeAg_{1.25}Ga_{4.25}$,[30] $Gd_{14}(Ag,Ga)_{51}$,[25] Gd(Ag,Ga),[25] and $Ln(Ag,Ga)_3$ (*Ln* = Sm, Gd, Tb-Tm, Lu)[31] have been reported, the structure determination of most are from polycrystalline samples and the physical properties of most of these compounds have not been investigated. Here we report the flux growth and characterization of $Ln_2Ag_{1-x}Ga_{10-y}$ (*Ln* = La, Ce), a disordered variant of the Ce_2NiGa_{10} structure-type[32]. We will compare $Ce_2Ag_{1-x}Ga_{10-y}$ ($x \sim 0.3$; $y \sim 0.9$) to Ce_2NiGa_{10} to examine the structural changes with transition metal substitution and to the structurally related $YbGa_5$[33] to investigate the nature of the disordered Ga-network.

2.2 Experimental

2.2.1 Synthesis of $La_2Ag_{1-x}Ga_{10-y}$ ($x \sim 0.3$; $y \sim 0.6$) and $Ce_2Ag_{1-x}Ga_{10-y}$ ($x \sim 0.3$; $y \sim 0.9$)

Single crystals of $La_2Ag_{1-x}Ga_{10-y}$ ($x \sim 0.3$; $y \sim 0.6$) and $Ce_2Ag_{1-x}Ga_{10-y}$ ($x \sim 0.3$; $y \sim 0.9$) were grown by the self-flux method. La or Ce rod (3N), Ag powder (3N), and Ga pellets (6 N) were used as received, placed in an alumina crucible in a mole ratio of 2:1:20, and sealed in

evacuated fused silica tubes. The reaction profile involved heating the reaction ampoule to 1150 °C at a rate of 200 °C/hour. After dwelling for 12 hours, the tube was cooled to 500 °C at 200 °C/hour and then cooled to 400 °C at 2 °C/hour. After dwelling at 400 °C for 5 days, the tube was inverted and spun to remove excess flux. Hot water and dilute HCl were used to remove excess Ga from the surface of the crystals. Using the above described reaction profile, several batches of $Ln_2Ag_{1-x}Ga_{10-y}$ (*Ln* = La and Ce) crystals were grown as layered aggregates (0.5 x 10 x 10 mm^3) with typical single crystal size of approximately 0.025 x 0.5 x 0.5 mm^3 and a typical yield of 80% and showed no noticeable oxidation in air.

The slow cooling step of 2 °C/hour to 400 °C is the determining factor in the growth of $Ln_2Ag_{1-x}Ga_{10-y}$ (*Ln* = La, Ce) over the robust $BaAl_4$-type $Ln(Ag,Ga)_4$ phase. Systematic investigation of the reaction profile through adjustments of the dwell time at the highest dwelling temperature (1150 °C), the cooling rate of the fast step (200 °C/hour), the cooling rate of the slow step (2 °C/hour), the spin temperature (400 °C), or the final dwell time (5 days) led to the formation of the $Ln(Ag,Ga)_4$ ($BaAl_4$-type) phase except for the reaction profile given in the previous paragraph. The slow cooling step was systematically varied by cooling at a rate of 8 °C/hr (or 4 °C/hr) to 400 °C followed by dwelling for 5 days. One-step fast cooling sequences used included cooling at a rate of 200 °C/hour to 400 °C and cooling at a rate of 200 °C/hour to 650 K. Both of these one-step cooling sequences resulted in the growth of the $BaAl_4$-type $Ln(Ag,Ga)_4$ phase. Annealing of $Ln_2Ag_{1-x}Ga_{10-y}$ (*Ln* = La, Ce) crystals at 650 °C (or 400 °C) for several hours to several days resulted in the growth of $Ln(Ag,Ga)_4$ ($BaAl_4$-structure type).

Systematic investigation of the reaction ratio was also explored to establish the homogeneity range by varying the composition of each reactant separately. This compound exhibits a very narrow phase width, consistent with the composition determined by EDXS

(Energy-Dispersive X-ray Spectroscopy) ($La_2Ag_{0.67(5)}Ga_{9.17(13)}$ and $Ce_2Ag_{0.67(9)}Ga_{9.25(8)}$) and with the composition determined by single crystal X-ray diffraction ($La_2Ag_{0.7(1)}Ga_{9.4(1)}$ and $Ce_2Ag_{0.7(1)}Ga_{9.1(1)}$).

2.2.2 Single Crystal and Powder X-ray Diffraction

Ground aggregates of $Ln_2Ag_{1-x}Ga_{10-y}$ (*Ln* = La, Ce) were characterized by X-ray powder diffraction using a Bruker AXS D8 Advance diffractometer with Cu Kα radiation (λ = 1.5418 Å) to ensure phase purity of each batch and consistency with the single crystal X-ray diffraction refined model. Silver-colored fragments of single crystals of $La_2Ag_{1-x}Ga_{10-y}$ ($x \sim 0.3$; $y \sim 0.6$) and $Ce_2Ag_{1-x}Ga_{10-y}$ ($x \sim 0.3$; $y \sim 0.9$) (0.03 x 0.05 x 0.06 and 0.03 x 0.03 x 0.03 mm^3, respectively) were glued to glass fibers with epoxy and mounted on the goniometer of a Nonius Kappa CCD diffractometer equipped with Mo Kα radiation (λ = 0.71703 Å). High-resolution data were collected up to θ = 31 ° at 298 K and 100 K for both analogues. SIR 92[34] was used to obtain a starting model (Laue class *4/mmm*), and SHELXL-97[35] was used for structure refinement. The room temperature structures for $Ln_2Ag_{1-x}Ga_{10-y}$ (*Ln* = La, Ce) were refined anisotropically in space group *I*4*/mmm* (No. 139) with $R_1 = 0.0211$ and $R_1 = 0.0263$ for La and Ce at 298 K. The 100 K data for $Ln_2Ag_{1-x}Ga_{10-y}$ (*Ln* = La, Ce) were modeled with isotropic atomic displacement parameters for Ga2 and Ga6 and anisotropic displacement parameters for the remaining atomic positions. No missing symmetry elements were found for this solution using PLATON[36]. Further crystallographic parameters are provided below in Table 2.1.

2.2.3 Refinement of Structural Disorder

The presence of anomalous atomic displacement parameters, anomalies in the electron difference maps, and anomalous residual electron density indicated disorder at the *M*1 (4*d*) (*M* = Ag + Ga), Ga2 (8*g*), Ga5 (2*b*), and Ga6 (16*n*) sites. Low temperature data collections were used

to determine the nature of the disorder, statistical or dynamic, which is best described as static disorder for both $La_2Ag_{1-x}Ga_{10-y}$ ($x \sim 0.3$; $y \sim 0.6$) and $Ce_2Ag_{1-x}Ga_{10-y}$ ($x \sim 0.3$; $y \sim 0.9$) phases since both 100 K and 298 K data collections yield the same structural model with no splitting of

Table 2.1 Crystallographic Data of $Ln_2Ag_{1-x}Ga_{10-y}$ (*Ln* = La, Ce) (Tetragonal, *I*4/*mmm*)

Crystal data				
Composition	$La_2Ag_{0.7(1)}Ga_{9.4(1)}$	$La_2Ag_{0.7(1)}Ga_{9.4(1)}$	$Ce_2Ag_{0.7(1)}Ga_{9.1(1)}$	$Ce_2Ag_{0.7(1)}Ga_{9.1(1)}$
a (Å)	4.3381(6)	4.3236(6)	4.2928(6)	4.2769(6)
c (Å)	26.1630(18)	26.1020(18)	26.1240(15)	26.0750(15)
V (Å^3)	492.36(10)	487.94(10)	481.42(10)	476.96(10)
Z	2	2	2	2
Crystal size (mm^3)	0.03 x 0.05 x 0.06	0.03 x 0.05 x 0.06	0.03 x 0.03 x 0.03	0.03 x 0.03 x 0.03
Data Collection				
Temperature (K)	298	100	298	100
Measured reflections	1069	708	6752	4104
Independent reflections	376	266	280	279
Reflections with I >2σ(I)	314	223	265	245
R_{int}	0.0331	0.0278	0.0252	0.0425
h	-6 → 6	-6 → 6	-4 → 6	-6 → 6
k	-4 → 6	-4 → 6	-6 → 6	-4 → 4
l	-41 → 42	-36 → 35	-37 → 37	-37 → 37
Refinement				
θ range (˚)	1.56-34.95	1.56-30.01	3.12-30.86	4.69-30.96
[a]$R_1[F^2>2\sigma F^2)]$	0.0211	0.0339	0.0263	0.0279
[b]$wR_2(F^2)$	0.0453	0.0723	0.0497	0.0677
Parameters	25	20	25	20
GooF on F^2	1.432	1.937	1.110	1.154
μ (mm^{-1})	34.769	35.084	35.503	35.871
Δp_{max} (eÅ^{-3})	2.043	2.193	1.358	2.108
Δp_{min} (eÅ^{-3})	-1.327	-2.585	-1.183	-1.334
Extinction coefficient (x10^{-4})	46(4)	28(5)	26(2)	26(4)

[a]$R_1 = \Sigma||F_0| - |F_c||/\Sigma|F_0|$

[b]$wR_2 = [\Sigma w(F_o^2 - F_c^2)^2/\Sigma w(F_0^2)^2]^{1/2}$; $P = (F_o^2 + 2F_c^2)/3$; $w = 1/[\sigma^2(F_o^2) + 8.9P]$, $w = 1/[\sigma^2(F_o^2) + (0.0114P)^2 + 8.9P]$, $w = 1/[\sigma^2(F_o^2) + 9.8P]$, and $w = 1/[\sigma^2(F_o^2) + (0.0235P)^2 + 8.9P]$ for $La_2Ag_{0.7(1)}Ga_{9.4(1)}$ (298 K), $La_2Ag_{0.7(1)}Ga_{9.4(1)}$ (100 K), $Ce_2Ag_{0.7(1)}Ga_{9.1(1)}$ (298 K), $Ce_2Ag_{0.7(1)}Ga_{9.1(1)}$ (100 K), respectively.

disordered sites or significant changes in the sizes of the atomic displacement parameters in the 100 K data collection. There are two types of statistical disorder present in these phases: substitutional disorder due to the mixing of Ag and Ga at the *M*1 (4*d*) site (*M*1 = Ag1 + Ga1) and positional disorder due to the partial occupancy of Ga at the Ga2 (8*g*), Ga5 (2*b*), and Ga6 (16*n*)

sites. Mixing between Ag and Ga at the same crystallographic site has been reported previously in AgGa-containing intermetallic compounds due to the similar size, electronegativity, and

Table 2.2 Positional and Atomic Displacement Parameters of $Ln_2Ag_{1-x}Ga_{10-y}$ (*Ln* = La, Ce)

$La_2Ag_{0.7(1)}Ga_{9.4(1)}$

298 K

Atom	Wyckoff position	*x*	*y*	*z*	Occ.[a]	U_{eq} (Å^2)[b]
La	4*e*	0	0	0.35258(3)	1.00	0.0081(2)
*M*1	4*d* (0.31(2) Ag + 0.69(2) Ga)	0	½	¼	1.00	0.0103(3)
Ga2	8*g*	0	½	0.9520(4)	0.34(4)	0.022(3)
Ga3	4*e*	0	0	0.09907(5)	1.00	0.0112(3)
Ga4	4*e*	0	0	0.19412(5)	1.00	0.0101(3)
Ga5	2*b*	0	0	½	0.15(2)	0.026(4)
Ga6	16*n*	0	0.383(2)	0.4561(3)	0.29(3)	0.0238(18)

100K

Atom	Wyckoff position	*x*	*y*	*z*	Occ.[a]	U_{eq} (Å^2)[b]
La	4*e*	0	0	0.35263(5)	1.00	0.0051(4)
*M*1	4*d* (0.31(2) Ag + 0.69(2) Ga)	0	½	¼	0.31(2)	0.0053(3)
Ga2	8*g*	0	½	0.9524(2)	0.34(4)	0.0061(9)
Ga3	4*e*	0	0	0.09888(9)	1.00	0.0063 (6)
Ga4	4*e*	0	0	0.19408(9)	1.00	0.0053(5)
Ga5	2*b*	0	0	½	0.15(2)	0.007(4)
Ga6	16*n*	0	0.3732(9)	0.45563(16)	0.29(3)	0.0047(7)

$Ce_2Ag_{0.7(1)}Ga_{9.1(1)}$

298 K

Atom	Wyckoff position	*x*	*y*	*z*	Occ.[a]	U_{eq} (Å^2)[b]
Ce	4*e*	0	0	0.35251(2)	1.00	0.00865(19)
*M*1	4*d* (0.35(3) Ag + 0.65(3) Ga)	0	½	¼	1.00	0.0118(2)
Ga2	8*g*	0	½	0.9525(5)	0.19(4)	0.019(4)
Ga3	4*e*	0	0	0.09842(4)	1.00	0.0123(3)
Ga4	4*e*	0	0	0.19319(4)	1.00	0.0112(3)
Ga5	2*b*	0	0	½	0.06(3)	0.029(7)
Ga6	16*n*	0	0.3769(9)	0.45631(13)	0.37(3)	0.0185(9)

100K

Atom	Wyckoff position	*x*	*y*	*z*	Occ.[a]	U_{eq} (Å^2)[b]
Ce	4*e*	0	0	0.35253(3)	1.00	0.0053(3)
*M*1	4*d* (0.35(3) Ag + 0.65(3) Ga)	0	½	¼	1.00	0.0064(3)
Ga2	8*g*	0	½	0.9528(2)	0.19(4)	0.0059(10)
Ga3	4*e*	0	0	0.09831(5)	1.00	0.0067(4)
Ga4	4*e*	0	0	0.19312(5)	1.00	0.0065(3)
Ga5	2*b*	0	0	½	0.06(3)	0.008(6)
Ga6	16*n*	0	0.3709(5)	0.45618(7)	0.37(3)	0.0041(4)

[a]Occupancy

[b]U_{eq} is defined at one third of the trace of the orthogonalized U_{ij} tensor.

coordination preferences of Ag and Ga.[20-25, 27-31, 37] The occupancy and atomic displacement parameters of *M*1 (Ag1 + Ga1), Ga2, Ga5, and Ga6 sites were first refined separately and then together to yield the occupancies shown below in Table 2.2.

2.2.4 Energy-Dispersive X-ray Spectroscopy (EDXS) of $Ln_2Ag_{1-x}Ga_{10-y}$ (*Ln* = La, Ce)

The composition of aggregates (0.5 x 10 x 10 mm^3) of $Ln_2Ag_{1-x}Ga_{10-y}$ (*Ln* = La, Ce) were characterized with the Energy-Dispersive X-ray Spectroscopy (EDXS) option of a JEOL JSM-5060 scanning electron microscope using an accelerating voltage of 15 kV and a beam to sample distance of 20 mm. Several aggregates of $La_2Ag_{1-x}Ga_{10-y}$ ($x \sim 0.3$; $y \sim 0.6$) and $Ce_2Ag_{1-x}Ga_{10-y}$ ($x \sim 0.3$; $y \sim 0.9$) were scanned at 10 different areas on the smooth surface of each aggregate. Several aggregates of $Ln_2Ag_{1-x}Ga_{10-y}$ (*Ln* = La, Ce) were also scanned along the cross-section to investigate the formation a silver concentration gradient during crystal growth. The average compositions, standardized to *Ln* (*Ln* = La, Ce), are $La_2Ag_{0.67(5)}Ga_{9.17(13)}$ and $Ce_2Ag_{0.67(9)}Ga_{9.25(8)}$ and are consistent with refined compositions as obtained from single crystal X-ray diffraction. Measurement from multiple batches of $Ln_2Ag_{1-x}Ga_{10-y}$ (*Ln* = La, Ce) yielded the same concentrations, within experimental error, with no indication of the formation of a silver concentration gradient.

2.2.5 Property Measurements

The temperature-dependent magnetic susceptibility, χ, of aggregates of $La_2Ag_{1-x}Ga_{10-y}$ ($x \sim 0.3$; $y \sim 0.6$) and $Ce_2Ag_{1-x}Ga_{10-y}$ ($x \sim 0.3$; $y \sim 0.9$) were measured from 3 – 265 K at H = 0.1 T using a Quantum Design Physical Property Measurement System (PPMS). At temperatures between 30 and 265 K, susceptibility data were fit using a modified Curie-Weiss equation. Field-dependent magnetization of the sample was measured from 0 T – 5 T at 1.9 K and from 0 T – 9 T at 3 K. Specific heat was measured using the thermal relaxation option of the PPMS down to 0.4 K.

2.3 Results and Discussion

2.3.1 Structure of $Ln_2Ag_{1-x}Ga_{10-y}$ (*Ln* = La, Ce), a Disordered Variant of the Ce_2NiGa_{10} Structure Type.

$Ln_2Ag_{1-x}Ga_{10-y}$ (*Ln* = La, Ce) crystallize in the tetragonal *I*4/*mmm* space group (No. 139) with crystallographic parameters provided in Table 2.1. The crystal structures of $Ln_2Ag_{1-x}Ga_{10-y}$ (*Ln* = La, Ce) are disordered variants of the Ce_2NiGa_{10} structure type.[32, 38] The structure of Ce_2NiGa_{10} can be described as an inhomogeneous linear intergrowth of $BaAl_4$-type $CeGa_4$ segments and CaF_2-type $NiGa_2$ segments.[38-39] The $BaAl_4$-type segment, which is also a structural subunit in structurally related $YbGa_5$,[33] consists of layers of face-sharing tetragonal antiprisms $^2_\infty[Ce_{4/8}Ga_{8/4}]_2 = CeGa_4$. Unlike $YbGa_5$, which has a $PtHg_2$-type segment[33], the CaF_2-type segment in Ce_2NiGa_{10} consists of face-sharing rectangular prisms $^2_\infty[Ga_{8/4}Ni] = Ga_2Ni$. Combination of the two segments yields $2CeGa_4 + Ga_2Ni$ (Figure 2.1b) = Ce_2NiGa_{10}. In the case of $Ln_2Ag_{1-x}Ga_{10-y}$ (*Ln* = La, Ce) (Figure 2.1a), the $BaAl_4$-type $Ce(Ag,Ga)_4$ segment (Figure 2.1d) is built of layers of face-sharing tetragonal antiprisms $^2_\infty[Ce_{4/8}(Ag,Ga)_{8/4}]_2 = CeAg_xGa_{4-x}$ with Ag (~ 40 %) and Ga (~ 60 %) mixing at the 4*d* (-4*m*2) site, and the distorted CaF_2-type gallium segment (Figure 2.1c) consists of face-sharing cubes $^2_\infty[Ga_{8/4}Ga] = Ga_{3-y}$ with the center of the cubes partially occupied with 6 - 10 % Ga. The combination of the two segments yields $2CeAg_xGa_{4-x}$ (Figure 2.1d) + Ga_{3-y} (Figure 2.1c) = $Ce_2Ag_{1-x}Ga_{10-y}$ (Figure 2.1a).

There are six different types of *M*/Ga sites in $Ln_2Ag_{1-x}Ga_{10-y}$ (*Ln* = La, Ce) with coordination environments ranging from 4, 5, 7 and 10. *M*1 (*M* = Ag + Ga) is in the center of a tetrahedron of four Ga4 atoms, and Ga3 is in the center of a tetrahedron of Ga4 and positionally disordered Ga2/Ga6 atoms. Ga4 is in the center of a distorted square pyramid with short contacts between Ga3-Ga4 (~ 2.48 Å) and long contacts between *M*-Ga4 (~ 2.61 Å). The Ga2/Ga6 sites are positionally disordered and have a summed occupancy of unity within

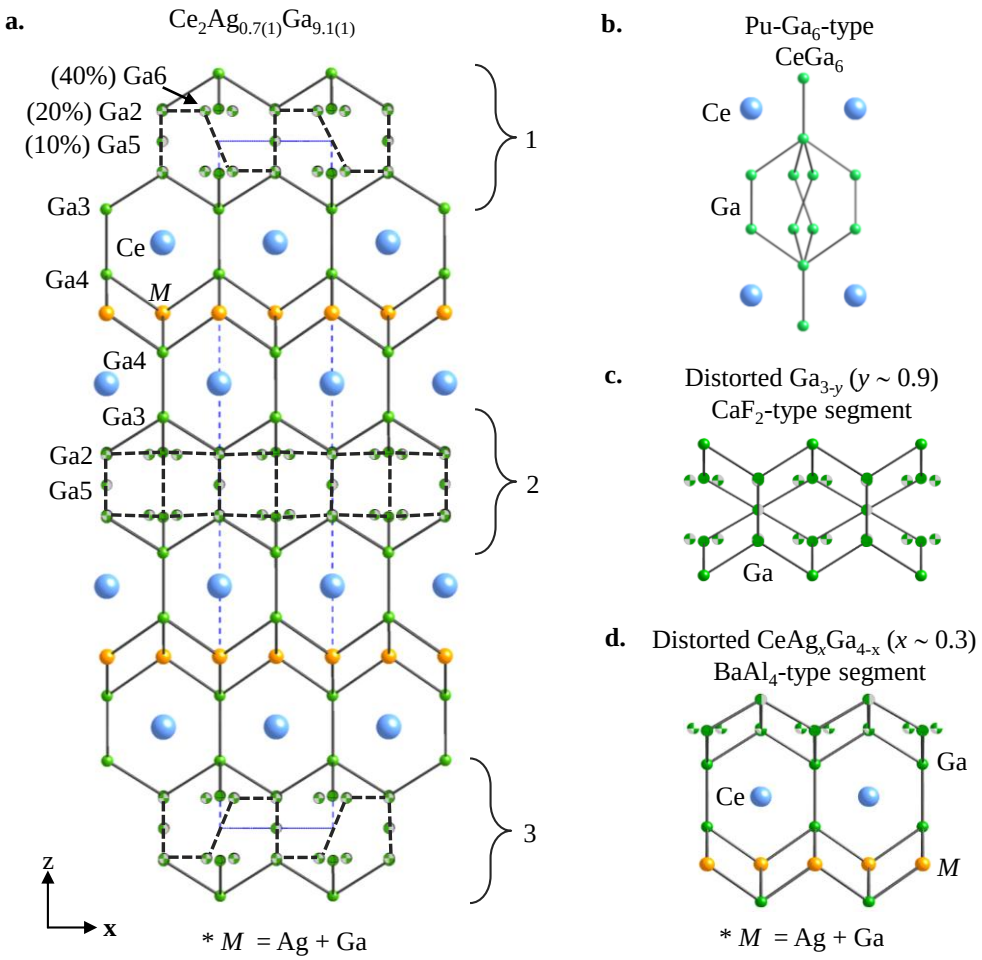

Figure 2.1 **a.** $Ce_2Ag_{0.7(1)}Ga_{9.1(1)}$ can be described as a distorted variant of the Ce_2NiGa_{10} structure with the **c.** distorted gallium segments best described as variants of **b.** $CeGa_6$ ($PuGa_6$-structure type). **d.** The distorted $Ce(Ag,Ga)_4$-type segments are built of layers of face-sharing tetragonal antiprisms. Here M = Ag + Ga and the shaded atoms are partially occupied.

experimental error, which indicates the presence of either a Ga2 or Ga6 at each position in a unit cell. Each Ga2/Ga6 atom is surrounded by 5 Ga2/Ga6 atoms and 2 Ga3 atoms for a total coordination of seven. The average Ga5-centered bicapped rectangular prism is shown in Figure 2.1c.

Understanding the disordered gallium network is critical for understanding the magnetic ground state of $Ce_2Ag_{1-x}Ga_{10-y}$ (Ln = La, Ce). The disordered CaF_2-type gallium segments, shown in brackets 1-3 of Figure 2.1a, can be best visualized as the average of three structural subunits of the (Figure 2.1b) $PuGa_6$-type $CeGa_6$ segments. The disorder in this segment occurs around the site Ga5 (2*b*, 4/*mmm*) where Ni is replaced by Ga in the Ce_2NiGa_{10} structure. The

Ga2 (8*g*) and Ga6 (16*n*) sites represent the vertices of a cube and are both partially occupied with short contacts (~ 2.4 Å) between the vertices and the center, Ga5 (2*b*), of the cube as shown in Figure 2.1c. Similar disordered gallium networks have been observed in the structurally related phases $YbGa_5$ (Ce_2NiGa_{10}-type structure),[33] $CeAg_xGa_{4-x}$ ($BaAl_4$-type structure),[20] $CeGa_6$ ($PuGa_6$-type structure),[40] and Ce_2NiGa_{10} (own-type structure). $YbGa_5$, like $Ln_2Ag_{1-x}Ga_{10-y}$ (*Ln* = La, Ce), is a disordered variant of Ce_2NiGa_{10}-structure type. In the distorted bicapped rectangular prismatic Ga environments of $YbGa_5$ the authors suggested that the intrinsic disorder and split atom positions stem from the tendency of Ga to achieve the optimum coordination of four.[33] Previously published *Ln*:Ga (*Ln* = lanthanide) binary and *Ln*:Ag:Ga (*Ln* = lanthanide) ternary phases depict Ga atoms in four coordinate environments with Ga-*T* (T = transition metal or Ga) interatomic distances ranging from 2.5 to 2.6 Å.[20-32] A coordination of four can be obtained for all the Ga atoms in $YbGa_5$ by applying limits on interatomic distances ~ 2.5 - 2.6 Å consistent with previously published *Ln*:Ga (*Ln* = lanthanide) binary and *Ln*:Ag:Ga (*Ln* = lanthanide) ternary phases.[20-32] This approach applied to $Ce_2Ag_{0.7(1)}Ga_{9.1(1)}$ results in the three most-likely components, shown in brackets 1-3 of Figure 2.1a, which when superposed on each other give the average crystal structure of $Ce_2Ag_{0.7(1)}Ga_{9.1(1)}$. The components in brackets 1 and 3 each represent ~ 40 % of the total average structure and can be considered the majority components, whereas the component in bracket 2 represents ~ 20 % of the average structure and can be considered the minority component. The dashed lines connecting hatched spheres in Figure 2.1a represent likely bonds between disordered sites.

The disorder in the CaF_2-type gallium segment can be rationalized as the tendency of gallium to adopt a coordination of four. Analysis of the structures of $LaNi_{1-x}Ga_6$[38], $CeAg_{1.25}Ga_{4.25}$,[30] $YbGa_5$,[33] $Ln_5(Ag,Ga)_{19-x}$ (*Ln* = Gd, Tb; $x \sim 2.2$),[29] ε-$SmGa_6$,[41] and $YbGa_{3.34}$[42]

indicates that these disordered gallium networks can also be rationalized considering the tendency of gallium to be four coordinate. Select interatomic distances of $La_2Ag_{0.7(1)}Ga_{9.4(1)}$ and $Ce_2Ag_{0.7(1)}Ga_{9.1(1)}$ are provided in Table 2.3. The Ga-Ga and *M*-Ga (*M* = Ag + Ga) interatomic distances of fully occupied sites are ~ 2.5 Å and ~ 2.6 Å which are consistent with other AgGa-containing intermetallic compounds and with similar distorted gallium networks.[20-33, 37, 42]

Table 2.3 Interatomic Distances (Å) of $Ln_2Ag_{1-x}Ga_{10-y}$ (*Ln* = La, Ce)

		$La_2Ag_{0.7(1)}Ga_{9.4(1)}$ **298K**	$Ce_2Ag_{0.7(1)}Ga_{9.1(1)}$	$La_2Ag_{0.7(1)}Ga_{9.4(1)}$ **100K**	$Ce_2Ag_{0.7(1)}Ga_{9.1(1)}$
Tetragonal antiprisms		Distances (Å)			
Ln-*M*1	(x4)	3.4507(7)	3.4320(5)	3.4423(10)	3.4235(5)
Ln-Ga2	(x4)	3.387(8)	3.380(10)	3.385(4)	3.378(4)
Ln-Ga3	(x4)	3.3181(7)	3.2951(6)	3.3089(11)	3.2847(6)
Ln-Ga4	(x4)	3.3019(7)	3.2618(6)	3.2913(10)	3.2501(6)
Ln-Ga5	(x1)	3.8569(8)	3.8530(6)	3.8467(13)	3.8453(6)
Ln-Ga6	(x4)	3.178(9)	3.158(4)	3.136(4)	3.134(2)
Tetrahedra [*] *M*					
*M*1-*M*1	(x4)	3.0675(4)	3.0355(4)	3.0572(4)	3.0242(4)
*M*1-Ga4	(x4)	2.6157(8)	2.6095(7)	2.6085(14)	2.6024(8)
Gallium network					
Ga2-Ga2	(x1)	2.512(19)	2.48(2)	2.486(10)	2.49(3)
Ga2-Ga3	(x2)	2.547(5)	2.525(6)	2.542(3)	2.520(3)
Ga2-Ga5	(x2)	2.506(5)	2.479(6)	2.494(3)	2.467(3)
Ga2-Ga6	(x2)	0.519(8)	0.537(4)	0.555(4)	0.559(2)
Ga2-Ga6	(x2)	2.457(4)	2.440(8)	2.463(5)	2.6641(14)
Ga3-Ga4	(x1)	2.4870(19)	2.4759(15)	2.485(3)	2.4723(18)
Ga3-Ga6	(x8)	2.655(3)	2.6326(18)	2.646(3)	2.6260(12)

[*] *M* = Ag + Ga.

2.3.2 Structural Comparison of $Ln_2Ag_{1-x}Ga_{10-y}$ (*Ln* = La, Ce) and $YbGa_5$, disordered variants of the Ce_2NiGa_{10} structure type.

The $YbGa_5$ structure is very similar to $Ln_2Ag_{1-x}Ga_{10-y}$ (*Ln* = La, Ce), yet there are two differences between $Ln_2Ag_{1-x}Ga_{10-y}$ (*Ln* = La, Ce) and $YbGa_5$. In $YbGa_5$ the symmetry of the compound is reduced with respect to the Ce_2NiGa_{10} parent structure due to a displacement of the Ga2 atom from the 4-fold axis on the 4*mm* site, whereas in $Ln_2Ag_{1-x}Ga_{10-y}$ (*Ln* = La, Ce) the equivalent gallium site (4*mm*, 4*e*) remains on the 4-fold axis. In $Ln_2Ag_{1-x}Ga_{10-y}$ (*Ln* = La, Ce),

the Ga5 (4/*mmm*, 2*b*) site is partially occupied (~10 %) whereas in $YbGa_5$ the 4/*mmm* (2*b*) site (the center of the cube) is vacant. The partial occupancy at the 4/*mmm* (2*b*) site in $Ln_2Ag_{1-x}Ga_{10-y}$ (*Ln* = La, Ce) coincides with a larger available volume of the disordered cube in which to accommodate a gallium atom compared to $YbGa_5$. $Ln_2Ag_{1-x}Ga_{10-y}$ (*Ln* = La, Ce) is not the first reported gallium-rich intermetallic phase with a distorted gallium network. Several gallium-rich intermetallic phases with a distorted gallium networks include $LaNi_{1-x}Ga_6$,[38] $CeAg_{1.25}Ga_{4.25}$,[30] $YbGa_5$,[33] $Ln_5(Ag,Ga)_{19-x}$ (*Ln* = Gd, Tb; x ~2.2),[29] ε-$SmGa_6$,[41] $Sm_2Ga_{1.8}Ge_{5.2}$,[43] $Sm_4Ga_{5.24}Ge_{5.76}$,[43] $Ca_3Au_{6.61}Ga_{4.39}$,[44] and $YbGa_{3.34}$.[42] In addition to *Ln*:Ga (*Ln* = lanthanide) binary and *Ln*:Ag:Ga (*Ln* = lanthanide) ternary phases, complex GaGe-containing networks including YbGaGe,[10] $Ln_2MGa_9Ge_2$ (*Ln* = Ce, Sm; *M* = Ni, Co),[45] $Ln_3Ni_3Ga_8Ge_3$ (*Ln* = lanthanide),[46] $LnMGa_3Ge$ (*Ln* = lanthanide; *M* = Ni, Co)[6-7, 46] and $Ln_4FeGa_{12-x}Ge_x$ (*Ln* = Sm, Tb; x = 2.5)[47] have been the focus of recent work.

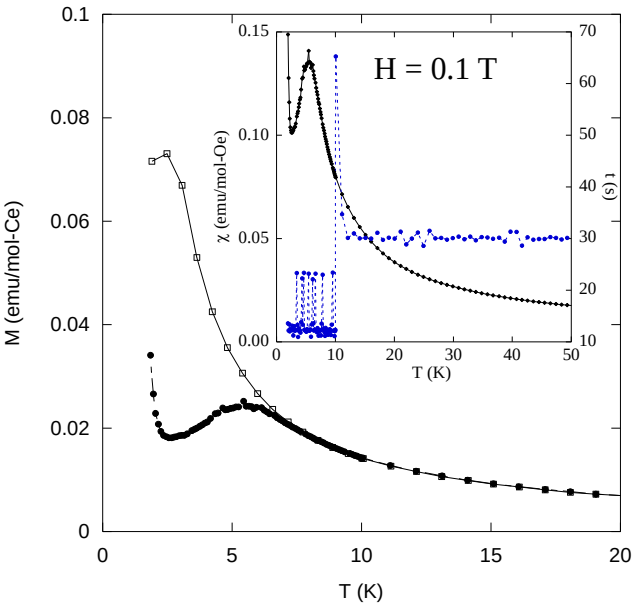

Figure 2.2 The two measurements of the magnetic susceptibility on the same crystal aggregate. (inset) Time-dependence of the magnetic susceptibility of $Ce_2Ag_{0.7(1)}Ga_{9.1(1)}$ at 0.1 T can be attributed to spin glass behavior of Ce^{3+} moments due to the varying local Ce^{3+} environment.

2.3.3 Physical Properties of $Ce_2Ag_{0.7(1)}Ga_{9.1(1)}$

Previously reported $LnAg_xGa_{4-x}$ (*Ln* = La - Nd, Sm and Yb) with $0.3 < x < 0.7$ show property dependence on silver concentration,[20-21] so property measurements on $Ce_2Ag_{0.7(1)}Ga_{9.1(1)}$ were performed on multiple aggregates to determine reproducibility. No noticeable differences

were observed, indicating that the range of silver concentration does not influence the physical properties in this phase.

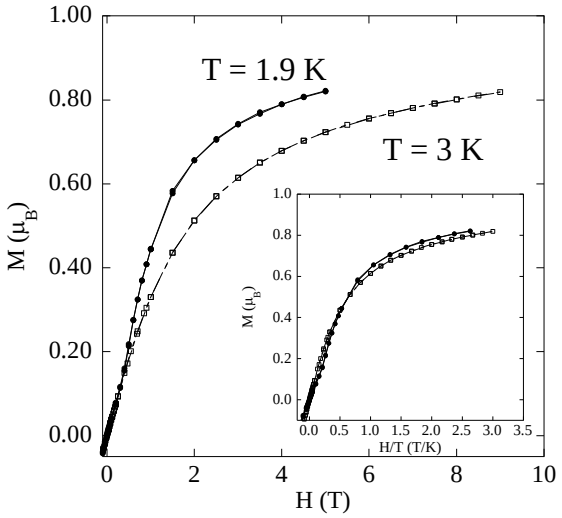

Figure 2.3 The field-dependent magnetization of $Ce_2Ag_{0.7(1)}Ga_{9.1(1)}$ at 1.9 K from 0 to 5 T and at 3 K from 0 to 9 T. As shown in the bottom-right inset, the temperature-normalized, field-dependent magnetization curves superpose on each other, with the slight deviation due to measurement time differences, which can be attributed to spin glass-like behavior.

The magnetic susceptibility χ of $Ce_2Ag_{0.7(1)}Ga_{9.1(1)}$ at 0.1 T, shown in Figure 2.2, was fit with the modified Curie-Weiss equation in the linear region of the inverse magnetic susceptibility from 30 to 265 K. The calculated effective moment of 2.49 μ_B is consistent with localized Ce^{3+} moments and the θ_W of -17.3(9) indicates antiferromagnetic coupling between magnetic moments with the onset of antiferromagnetic ordering below 3 K. Multiple measurements of magnetic susceptibility χ on the same aggregate of $Ce_2Ag_{0.7(1)}Ga_{9.1(1)}$ at 0.1 T yielded inconsistent results. Probing the relationship between the magnetic susceptibility and the time between data points, shown in the inset of Figure 2.2, illustrates a time-dependence of the magnetic susceptibility in $Ce_2Ag_{0.7(1)}Ga_{9.1(1)}$ with glassiness observed below 7 K.

Figure 2.3 shows the field-dependent magnetization at 1.9 K and 3 K. The magnetization of Ce^{3+} moments in $Ce_2Ag_{0.7(1)}Ga_{9.1(1)}$ is ~ 0.82 μ_B at 5 T when measured at 1.9 K and ~ 0.71 μ_B at 5 T when measured at 3 K. The field-dependent magnetization at 1.9 K is linear from -0.4 to 0.4 T, as seen in the top-left inset, which is indicative of antiferromagnetic ordering. The change in slope before -0.4 T and after 0.4 T can be attributed to a spin-flop transition. There is

evidence of time-dependent magnetism shown in the bottom- right inset of Figure 2.3 where the temperature-normalized, field-dependent magnetization curves superpose, with the slight deviation due to measurement time differences. The superposition of temperature-normalized, field-dependent magnetization curves can be attributed to spin glass-like behavior.

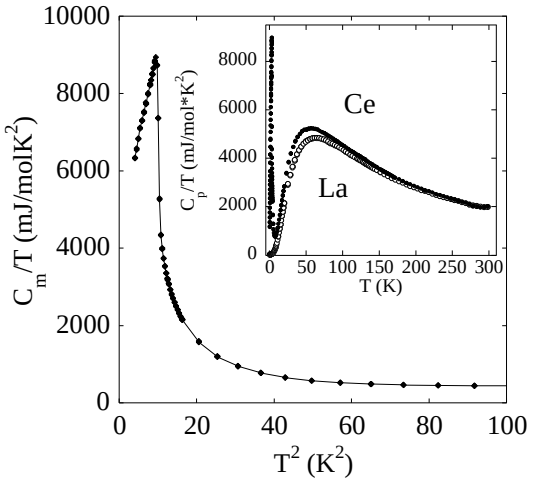

Figure 2.4 The magnetic heat capacity of $Ce_2Ag_{0.7(1)}Ga_{9.1(1)}$ shown below 10 K features a large peak due to the onset of antiferromagnetic ordering. The inset shows the heat capacity of $Ln_2Ag_{1-x}Ga_{10-y}$ (*Ln* = La, Ce).

Figure 2.4 shows the magnetic specific heat, C_m/T, of $Ce_2Ag_{0.7(1)}Ga_{9.1(1)}$ as obtained by subtracting C_p/T of $La_2Ag_{0.7(1)}Ga_{9.4(1)}$. The inset shows the total specific heat of both $Ce_2Ag_{0.7(1)}Ga_{9.1(1)}$ and $La_2Ag_{0.7(1)}Ga_{9.4(1)}$. The large peak at 3 K is consistent with the onset of antiferromagnetic ordering. The Sommerfeld parameter, γ, was determined experimentally by extrapolation to the y-intercept of C_m/T vs. T^2 from $C_m = \gamma T + \beta T^3$. The Sommerfeld parameter γ is ~ 585 mJ/molCe-K^2, fit from 6 to 11 K. The expected magnetic entropy (Rln2) for a Ce^{3+} atom is recovered under the transition. The Sommerfeld parameter for $La_2Ag_{0.7(1)}Ga_{9.4(1)}$ is ~ 0.01 mJ/molLa-K^2 and the Debye temperature is 204.3 K.

2.4 Conclusion

$La_2Ag_{0.7(1)}Ga_{9.4(1)}$ and $Ce_2Ag_{0.7(1)}Ga_{9.1(1)}$ phases were grown as part of our investigations of structural effects on magnetic behavior. The tendency for split sites and partial occupancy follows from the coordination preference of Ga[33]. The transition metal atoms occupy a different crystallographic site in $Ce_2Ag_{0.7(1)}Ga_{9.1(1)}$ than Ce_2MGa_{10} (*M* = Ni, Pd)[11, 32]. In $Ce_2Ag_{0.7(1)}Ga_{9.1(1)}$,

the Ag atoms share the 4*d* (-4*m*2) site with Ga, which is the equivalent site of mixing in $Ce(Ag,Ga)_4$. The spin glassiness of $Ce_2Ag_{0.7(1)}Ga_{9.1(1)}$ can be attributed to the inhomogeneous environment surrounding the Ce^{3+} moments.

2.5 References

(1) Sarrao, J. L.; Morales, L. A.; Thompson, J. D.; Scott, B. L.; Stewart, G. R.; Wastin, F.; Rebizant, J.; Boulet, P.; Colineau, E.; Lander, G. H., Plutonium-based superconductivity with a transition temperature above 18 K. *Nature* **2002,** *420*, 297-299.

(2) Curro, N. J.; Caldwell, T.; Bauer, E. D.; Morales, L. A.; Graf, M. J.; Bang, Y.; Balatsky, A. V.; Thompson, J. D.; Sarrao, J. L., Unconventional superconductivity in $PuCoGa_5$. *Nature* **2005,** *434*, 622-625.

(3) Opahle, I.; Oppeneer, P. M., Superconductivity caused by the pairing of plutonium 5f electrons in $PuCoGa_5$. *Phys. Rev. Lett.* **2003,** *90*, 157001.

(4) Cho, J. Y.; Moldovan, M.; Young, D. P.; Chan, J. Y., Crystal growth and magnetic properties of Ln_4MGa_{12} (*Ln* = Dy-Er; *M* = Pd, Pt). *J.Phys.: Condens. Matter* **2007,** *19*, 266224.

(5) Macaluso, R. T.; Nakatsuji, S.; Lee, H.; Fisk, Z.; Moldovan, M.; Young, D. P.; Chan, J. Y., Synthesis, structure, and magnetism of a new heavy-fermion antiferromagnet, $CePdGa_6$. *J. Solid State Chem.* **2003,** *174*, 296-301.

(6) Gray, D. L.; Francisco, M. C.; Kanatzidis, M. G., Distortion and charge density wave in the Ga square net coupled to the site occupancy wave in $YCo_{0.88}Ga_3Ge$. *Inorg. Chem.* **2008,** *47*, 7243-7248.

(7) Zhuravleva, M. A.; Evain, M.; Petricek, V.; Kanatzidis, M. G., $GdCo_{1-x}Ga_3Ge$: charge density wave in a Ga square net. *J. Am. Chem. Soc.* **2007,** *129*, 3082-3083.

(8) Troc, R.; Rogl, P.; Tran, V. H.; Czopnik, A., Magnetotransport and heat capacity in ternary compounds $U_3M_2M'_3$, *M* = Al, Ga; *M*' = Si, Ge *J. Solid State Chem.* **2001,** *158*, 227-235.

(9) Salvador, J. R.; Guo, F.; Hogan, T.; Kanatzidis, M. G., Zero thermal expansion in YbGaGe due to an electronic valence transition. *Nature* **2003,** *425*, 702-705.

(10) Margadonna, S.; Prassides, L.; Fitch, A. N.; Salvador, J. R.; Kanatzidis, M. G., Valence instabilties, phase transitions, and abrupt lattice expansion at 5 K in the YbGaGe system. *J. Am. Chem. Soc.* **2004,** *126*, 4498-4499.

(11) Millican, J. N.; Macaluso, R. T.; Young, D. P.; Moldovan, M.; Chan, J. Y., Synthesis, structure, and physical properties of Ce_2PdGa_{10}. *J. Solid State Chem.* **2004,** *177*, 4695-4700.

(12) Macaluso, R. T.; Millican, J. N.; Nakatsuji, S.; Lee, H.-O.; Carter, B.; Moreno, N. O.; Fisk, Z.; Chan, J. Y., A comparison of the structure and localized magnetism in Ce_2PdGa_{12} with the heavy fermion $CePdGa_6$. *J. Solid State Chem.* **2005,** *178*, 3547-3553.

(13) Cho, J. Y.; Millican, J. N.; Capan, C.; Sokolov, D. A.; Moldovan, M.; Karki, A. B.; Young, D. P.; Aronson, M. C.; Chan, J. Y., Crystal growth, structure, and physical properties of Ln_2MGa_{12} (*Ln* = La, Ce; *M* = Ni, Cu). *Chem. Mater.* **2008,** *20*, 6116-6123.

(14) Cho, J. Y.; Moldovan, M.; Young, D. P.; Lowhorn, N. D.; Chan, J. Y., Physical properties of $LnAg_yX_{4-y}$ (*Ln* = La, Ce; *X* = Al, Ga; *y* = 0.72). *Physica B* **2008,** *403*, 795-796.

(15) Cho, J. Y.; Thomas, E. L.; Nambu, Y.; Capan, C.; Karki, A. B.; Young, D. P.; Kuga, K.; Nakatsuji, S.; Chan, J. Y., Crystal growth, structure, and physical properties of $Ln(Cu,Ga)_{13-x}$ (*Ln* = La-Nd, Eu; $x \sim 0.2$). *Chem. Mater.* **2009,** *21*, 3072-3078.

(16) Thomas, K. R.; Cho, J. Y.; Millican, J. N.; Hembree, R. D.; Moldovan, M.; Karki, A.; Young, D. P.; Chan, J. Y., Crystal growth and physical properties of Ln_2MGa_{12} (*Ln* = Pr, Nd, and Sm; *M* = Ni, Cu). *J. Cryst. Growth* **2010,** *312*, 1098-1103.

(17) Hegger, H.; Petrovic, C.; Moshopoulou, E. G.; Hundley, M. F.; Sarrao, J. L.; Fisk, Z.; Thompson, J. D., Pressure-induced superconductivity in quasi-2d $CeRhIn_5$. *Phys. Rev. Lett.* **2000,** *84*, 4986-4989.

(18) Petrovic, C.; Movshovich, R.; Jaime, M.; Pagliuso, P. G.; Hundley, M. F.; Sarrao, J. L.; Fisk, Z.; Thompson, J. D., A new heavy-fermion superconductor $CeIrIn_5$: a relative of the cuprates. *Europhys. Lett.* **2001,** *53*, 354-359.

(19) Petrovic, C.; Pagliuso, P. G.; Hundley, M. F.; Movshovich, R.; Sarrao, J. L.; Thompson, J. D.; Fisk, Z.; Monthoux, P., Heavy-fermion superconductivity in $CeCoIn_5$ at 2.3 K. *J. Phys. Condens. Matter* **2001,** *13*, L337-L342.

(20) Grin, Y.; Hiebl, K.; Rogl, P.; Eibler, R., Ternary gallides $REAg_xGa_{4-x}$ (*RE* = La,Ce, Pr, Nd, Sm). *J. Less-Common Met.* **1986,** *115*, 367-372.

(21) Grin, Y.; Ellner, M.; Heibel, K.; Rogl, P., New ytterbium compounds with the $BaAl_4$ type of structure: crystal chemistry and magnetic properties of $Yb(Cu, Ag, Au, Pd, Pt)_xGa_{4-x}$. *J. Alloys Compd.* **1993,** *196*, 207-212.

(22) Grin, Y.; Ellner, M.; Hiebl, K.; Rogl, P.; Sichevich, O. M.; Myakush, O. M., Crystal chemistry and magnetic jproperties of the ternary compounds $RE_3Ag_xGa_{11-x}$ (*RE* = Y, Gd, Tb, Dy, Ho, Er, Tm, and Yb). *J. Solid State Chem.* **1993,** *105*, 399-405.

(23) Krachan, T.; Stel'makhovych, B.; Kuz'ma, Y., The Y-Ag-Ga system. *J. Alloys Compd.* **2005,** *386*, 147-150.

(24) Grin, Y.; Ellner, M.; Hiebl, K.; Baumgartner, B.; Rogl, P., $YbAgGa_2$: synthesis, crystal structure and magnetic behaviour. *J. Alloys Compd.* **1995,** *221*, 125-128.

(25) Gumeniuk, R. V.; Taras, I. B.; Kuzma, Y. B., The interactions between the components in the Gd-Ag-Ga system. *J. Alloys Compd.* **2006,** *416*, 131-134.

(26) Zygmunt, A.; Szytula, A.; Kolenda, M.; Tomkowicz, Z.; Stüsser, N.; Leciejewicz, J., Magnetic properties of *R*AgGa (*R* = Tb, Dy, Ho) compounds. *J. Magn. Magn. Mater.* **1996,** *161*, 127-132.

(27) Rossi, D.; Macciò, D., Ternary rare earth (*R*) alloys occurring in the RAg_2-RGa_2 section. *J. Alloys Compd.* **1998,** *281*, 222-227.

(28) Rossi, D.; Ferro, R., Ternary intermetallic *R*AgGa, *R*AuGa alloys (*R*=light rare earth and Yb). *J. Alloys Compd.* **2001,** *317-318*, 521-524.

(29) Gumeniuk, R. V.; Akselrud, L. G.; Kuz'ma, Y. B., Compounds $Ln_5(Ag,Ga)_{19-x}$ (*Ln* = Gd, Tb) - defective partially ordered representatives of the Rb_5Hg_{19} structure type. *Z. Naturforsch. B.* **2005,** *60*, 929-932.

(30) Gumeniuk, R. V.; Akselrud, L. G.; Stel'makhovych, B.; Kuzma, Y. B., The gallium rich region of the Ce-Ag-Ga system. *J. Alloys Compd.* **2005,** *389*, 127-132.

(31) Gumeniuk, R. V.; Prots, Y.; Schnelle, W.; Burkhardt, U.; Kuzma, Y. B.; Grin, Y. N., Crystal chemistry and magnetic properties of ternary compounds $REAg_xGa_{3-x}$ (*RE* = Sm, Gd, Tb, Dy, Ho, Er, Tm, Lu). *J. Alloys Compd.* **2009,** *469*, 28-33.

(32) Yarmolyuk, Y. P.; Grin, Y. N.; Rozhdestvenskaya, I. V.; Usov, O. A.; Kuzmin, A. M.; Bruskov, V. A.; Gladyshevskij, E. I., Crystal chemistry of series of inhomogeneous linear structures. III. the crystal structures of $Ce_2Ga_{10}Ni$ and $La_2Ga_{10}Ni$. *Kristallografiya* **1982,** *27*, 599-600.

(33) Giedigkeit, R.; Niewa, R.; Schnelle, W.; Grin, Y.; Kniep, R., On the binary compound $YbGa_5$. *Z. Anorg. Allg. Chem.* **2002,** *628*, 1692-1696.

(34) Altomare, A.; Burla, M. C.; Camalli, M.; Cascarano, G.; Giacovazzo, C.; Guagliardi, A.; Polidori, G., SIR92 - a program for automatic solution of crystal structures by direct methods. *J. Appl. Crystallogr.* **1994,** *27*, 435.

(35) Sheldrick, G. M., A short history of SHELX. *Acta Crystallogr. Sect. A.: Found Crystallogr.* **2008,** *A64*, 112-122.

(36) Spek, A. L., PLATON, a multipurpose crystallographic tool. *J. Appl. Crystallogr.* **2003,** *36*, 7-13.

(37) Gumeniuk, R. V.; Stel'makhovych, B.; Kuzma, Y. B., The Tb-Ag-Ga system. *J. Alloys Compd.* **2003,** *352*, 128-133.

(38) Grin, Y.; Yarmolyuk, Y. P.; Gladyshevskii, E. I., The crystal chemistry of series of inhomogeneous linear structures. I. symmetry and numberic symbols of the structures composed of fragments of the strucutre types $BaAl_4$, CaF_2, AlB_2, Cu, α-Fe, and α-Po. *Sov. Phys. Crystallogr.* **1982,** *27*, 413-417.

(39) Parthe, E., *Modern perspectives in inorganic chemistry*. Kluwer Academic Publishers: Boston, 1992; Vol. 382, p 77-95.

(40) Pelleg, J.; Kimmel, G.; Dayan, D., *R*Ga_6 (*R* = Rare Earth Atom), a common intermetallic compound of the *R*-Ga systems. *J. Less-Common Met.* **1981,** *81*, 33-44.

(41) Tillard, M.; Zitoun, D.; Belin, C., Structural versatility of the ε-$SmGa_x$ phase: x-ray, electron diffraction, and dft studies. *Inorg. Chem.* **2009,** *48*, 2399-2406.

(42) Tillard, M.; Belin, C., Investigation in the binary system Yb-Ga: crystal structure of the Ga-rich compound $YbGa_{3.34}$. *Inorg. Chem.* **2009** *48*, 9250-9257

(43) Tokaychuk, Y. O.; Filinchuk, Y. E.; Fedorchuk, A. O.; Kozlov, A. Y.; Mokra, I. R., New representatives of the linear structure series containing empty Ga/Ge cubes in the Sm-Ga-Ge system. *Journal of Solid State Chemistry* **2006,** *179* (5), 1323-1329.

(44) Kubmann, D.; Hoffman, R. D.; Pottgen, R., $Ca_3Au_{6.61}Ga_{4.39}$-a new gallide with a three dimensional gold gallium network. *Z. Anorg. Allg. Chem* **2001,** *627*, 2053-2056.

(45) Zhuravleva, M. A.; Kanatzidis, M. G., Polygallide $Re_2MGa_9Ge_2$ (*Re* = Ce, Sm; *M* = Ni, Co) phases grown in molten gallium. *Inorg. Chem.* **2008,** *47*, 9471-9477.

(46) Zhuravleva, M. A.; Pcionek, R. J.; Wang, X.; Schultz, A. J.; Kanatzidis, M. G., *ReM*Ga_3Ge and $Re_3Ni_3Ga_8Ge_3$ (*M* = Ni, Co; *Re* = rare-earth element): new intermetallics synthesized in liquid gallium. x-ray, electron, and neutron strucutre determination and magnetism. *Inorg. Chem.* **2003,** *42*, 6412-6424.

(47) Zhuravleva, M. A.; Wang, X.; Schultz, A. J.; Bakas, T.; Kanatzidis, M. G., Isolation of the new cubic phases $Re_4FeGa_{12-x}Ge$ (*Re* = Sm, Tb; *x* = 2.5) from molten gallium: single-crystal neutron diffraction study of the Ga/Ge distribution. *Inorg. Chem.* **2002,** *41*, 6056-6061.

CHAPTER 3. A TALE OF TWO POLYMORPHS: GROWTH AND CHARACTERIZATION OF α-*Ln*NiGa$_4$ (*Ln* = Y, Gd-Yb) AND β–*Ln*Ni$_{1-x}$Ga$_4$ (*Ln* = Tb-Er)[*]

3.1 Introduction

Unusual electronic and magnetic behavior in systems containing disordered Ga-networks may be due to the inhomogeneous electronic environment surrounding localized magnetic moments in structurally distorted networks.[1-6] The structural modulation discovered in *Ln*Co$_x$Ga$_3$Ge (*Ln* = Y, Gd) suggests that a charge density wave may be caused by modulations in its structure.[1-2] Atomic site disorder can also affect the magnetic properties of materials, including Ce$_2$Ag$_{1-x}$Ga$_{10-y}$ which exhibits time-dependent magnetism tentatively associated with a disorder induced spin glass-like coupling of the Ce^{3+} moments with long range antiferromagnetic ordering developing below 3 K.[6] This behavior is similar to the spin glass behavior observed in Ce$_2$CuSi$_3$ and Ce$_2$CuGe$_3$, where the atomic site disorder, a mixing of the transition metal (Cu) and the main group metal (Si or Ge), is analogous to applying chemical pressure in order to alter the electronic environment around the Ce^{3+} moments.[7-8] Similarly, disorder and Ag substitution suppress magnetic ordering by 9 K in Gd(Ag,Al,Si)$_2$ as compared to the parent Gd(Al,Si)$_2$.[9] Other examples of disorder controlled physical properties include the heavy fermion metal CePd$_2$Al$_3$ where random occupation of two Al sites leads to a varying electronic environment around the Ce^{3+} moments which prevents long range magnetic order.[10] These examples illustrate the effects of atomic disorder on magnetic ordering.

Orthorhombic α-*Ln*NiGa$_4$ (*Ln* = Y, Gd-Yb) and tetragonal β-*Ln*Ni$_{1-x}$Ga$_4$ (*Ln* = Tb-Er), were synthesized serendipitously while attempting to grow the latter lanthanide analogues of the Sm$_2$NiGa$_{12}$-structure type.[11] The structure and properties of the orthorhombic α-*Ln*NiGa$_4$ have

[*]Reprinted by permission of Wiley-VCH: Menard, M. C.; Drake, B. L.; McCandless, G. T.; Thomas, K. R.; Hembree, R. D.; Haldolaarachchige, N.; Young, D. P.; DiTusa, J.; Chan, J. Y., A tale of two polymorphs: growth and characterization of α-*Ln*NiGa$_4$ (*Ln* = Y, Gd-Yb) and β–*Ln*Ni$_{1-x}$Ga$_4$ (*Ln* = Tb-Er). *Eur. J. Inorg. Chem.* **2011,** *In Press.* "Copyright 2011 Wiley."

been previously reported.[12] The structure of the orthorhombic α-*Ln*$NiGa_4$ was characterized by X-ray powder diffraction from polycrystalline arc-melted samples as being isostructural to $YNiAl_4$.[13] Magnetic susceptibility measured over the range of 78 – 300 K indicates (- θ_W) antiferromagnetic correlations for Nd and Gd and ferromagnetic correlations (+ θ_W) for Tb – Tm. Three analogues, Y, Yb, and Lu, exhibit diamagnetic behavior with the Sm analogue showing Van Vleck paramagnetism. All analogues indicate that Ni does not carry a moment in α-*Ln*$NiGa_4$ (*Ln* = Y, Nd, Sm, and Gd-Lu). The tetragonal β-*Ln*$Ni_{1-x}Ga_4$ is a new defect variant of the Ce_2NiGa_{10}-structure type.[14] Below we report the growth, structure, and properties of tetragonal β-*Ln*$Ni_{1-x}Ga_4$ (*Ln* = Tb-Er).

3.2 Experimental

3.2.1 Synthesis of α-$LnNiGa_4$ (Ln = Y, Gd-Yb) and β-$LnNi_{1-x}Ga_4$ (Ln = Tb-Er)

Single crystals of the two polymorphs, orthorhombic α-*Ln*$NiGa_4$ (*Ln* = Y, Gd-Yb) and tetragonal β-*Ln*$Ni_{1-x}Ga_4$ (*Ln* = Tb-Er), were grown using the self-flux method where *Ln* (3*N*, Alfa Aesar), Ni powder (5*N*, Alfa Aesar) and Ga shot (7*N*, Alfa Aesar) were placed into alumina crucibles in 1.5:1:15 mole ratios. The only exception to this prescribed mole ratio is the Tm-analogue, which required a 2:1:15 stoichiometric ratio of Tm: Ni: Ga to grow large crystals of α-$TmNiGa_4$. The former stoichiometric ratio yielded smaller crystals of α-$TmNiGa_4$ up to ~ 2 mm in length. Each crucible was covered with quartz wool, sealed in an evacuated silica tube, and placed into a high temperature furnace for heat treatment. The reaction profiles, shown in Figure 3.1, for the growth of α-*Ln*$NiGa_4$ (*Ln* = Y, Gd-Yb)[12] and β-*Ln*$Ni_{1-x}Ga_4$ (*Ln* = Tb-Er) are very similar to that of Ln_2NiGa_{12} (*Ln* = Pr, Nd, Sm)[15] with differences in the cooling sequences resulting in the growth of α-*Ln*$NiGa_4$ or a mixture of α-*Ln*$NiGa_4$ and β-*Ln*$Ni_{1-x}Ga_4$. All samples were heated to 1423 K at 170 K/h and annealed at 1423 K for 24h.

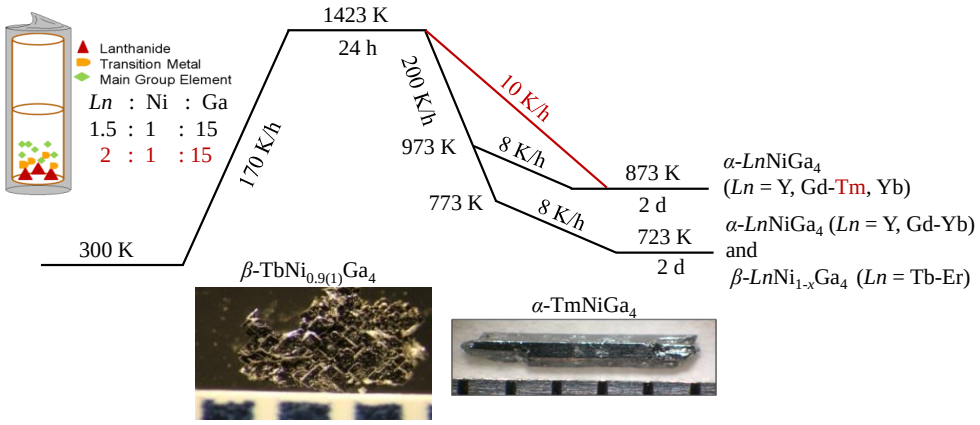

Figure 3.1 The growth profiles for α-*Ln*$NiGa_4$ (*Ln* = Y, Gd-Yb) and β-*Ln*$Ni_{1-x}Ga_4$ (*Ln* = Tb-Er) are shown with crystal pictures of α-$TmNiGa_4$ and β-$TbNi_{0.9(1)}Ga_4$. The synthesis ratio and profile adjustments required for the growth of large crystals of α-$TmNiGa_4$ are indicated in red. Surface roughness is due to etching and crystal deformities incurred while separating the crystals.

The cooling sequence, shown in Figure 3.1, for α-*Ln*$NiGa_4$ (*Ln* = Y, Gd-Yb) requires fast cooling (~ 200 K/h) to 973 K, followed by slow cooling (8 K/h) to 873 K, and dwelling for 2 days prior to centrifugation. The growth of large single crystals of α-$TmNiGa_4$ proved to be a synthetic anomaly and required elimination of the fast-cooling step in the temperature profile, which is shown as the red line in Figure 3.1. After dwelling at 1423 K for 24 h, the α-$TmNiGa_4$ was slow cooled from 1423 K to 873 K at 10 K/h followed by dwelling for 2 days and centrifugation. All growths with *Ln* = Y, Gd, Tm-Yb utilizing a cooling sequence of fast cooling (~ 200 K/h) to 773 K and slow cooling (8 K/h) to 723 K resulted in the growth of three different phases, α-*Ln*$NiGa_4$ (*Ln* = Y, Gd, Tm, Yb), $BaAl_4$-type *Ln*$(Ni,Ga)_4$,[16] and an unknown phase with stoichiometry determined by elemental analysis to be *Ln*$Ni_{1.3(1)}Ga_{4.3(1)}$. Optimum growth conditions for the orthorhombic phase are consistent with the initial reports of formation of orthorhombic α-*Ln*$NiGa_4$ (*Ln* = Y, Gd-Yb) via peritectic reaction at 1151 K.[17] Slow-cooling below 723 K led to the formation of multiple phases, instead of the α-*Ln*$NiGa_4$ (*Ln* = Y, Gd-Yb) phase, including $PuGa_6$-type *Ln*Ga_6 (*Ln* = Y, Gd-Yb)[18] and $BaAl_4$-type *Ln*$(Ni,Ga)_4$,[16] and the

unknown phase with stoichiometry determined by elemental analysis to be $Ln\text{Ni}_{1.3(1)}\text{Ga}_{4.3(1)}$ (*Ln* = Y, Gd-Yb).

β-$Ln\text{Ni}_{1-x}\text{Ga}_4$ (*Ln* = Tb-Er) was grown by fast cooling (~ 200 K/h) to 773 K and slow cooling (8 K/h) to 723 K. Following a dwell time of 2 days, each sample was inverted and centrifuged to remove excess Ga flux. All growths of β-$Ln\text{Ni}_{1-x}\text{Ga}_4$ (*Ln* = Tb-Er) yielded ~ 15% α-$Ln\text{NiGa}_4$ (*Ln* = Tb-Er) impurity phase and interestingly, when a sample of β-$Ln\text{Ni}_{1-x}\text{Ga}_4$ (*Ln* = Tb-Er) was allowed to slow-cool (10 K/h) from 823 K to 723 K, the product contained ~ 60% β-$Ln\text{Ni}_{1-x}\text{Ga}_4$ (*Ln* = Tb-Er) and ~ 40% α-$Ln\text{NiGa}_4$ (*Ln* = Tb-Er).[12] These growth experiments indicate the two-step cooling sequence with fast-cooling to 773 K followed by slow-cooling to 723 K is important for impurity phase reduction.

Although grown concurrently, orthorhombic α-$Ln\text{NiGa}_4$ (*Ln* = Tb-Er)[12] and tetragonal β-$Ln\text{Ni}_{1-x}\text{Ga}_4$ (*Ln* = Tb-Er) phases are easily separated by crystal morphology. As shown in Figure 3.1, the orthorhombic α-$Ln\text{NiGa}_4$ phase grows as rods ~ 6 mm in length, and the tetragonal β-$Ln\text{Ni}_{1-x}\text{Ga}_4$ phase grows as plate-like aggregates up to 2 mm × 1 mm × 0.025 mm. Crystals of both polymorphs did not show signs of degradation in air and only dilute HCl was needed to remove excess Ga flux from the surface of the crystals**.** Each crystal used for physical property measurements was checked via single crystal X-ray diffraction for phase identification.

3.2.2 Powder X-ray Diffraction, Single Crystal X-ray Diffraction, and Elemental Analysis

Several crystals of both the α-$Ln\text{NiGa}_4$ (*Ln* = Y, Gd-Yb)[12] and β-$Ln\text{Ni}_{1-x}\text{Ga}_4$ (*Ln* = Tb-Er) phases were ground for characterization by X-ray powder diffraction using a Bruker AXS D8 Advance diffractometer to confirm phase purity. Powder diffraction patterns from different batches were also compared to confirm phase purity. Independent powder diffraction on rods or

plates confirmed the phase purity of α-*Ln*NiGa$_4$ (*Ln* = Y, Gd-Yb) and β-*Ln*Ni$_{1-x}$Ga$_4$ (*Ln* = Tb-Er), respectively and indicated that the α- and β-phases can be separated by crystal morphology.

Silver-colored fragments of β-*Ln*Ni$_{1-x}$Ga$_4$ (*Ln* = Tb-Er) with approximate dimensions 0.03 × 0.03 × 0.04 mm^3 were cleaved from single crystals and mounted on the goniometer of a Nonius Kappa CCD diffractometer equipped with Mo Kα radiation (λ = 0.71073 Å). Data were collected up to θ = 31 ° at 100 K for β-*Ln*Ni$_{1-x}$Ga$_4$ (*Ln* = Tb-Er). SIR92[19] was used to obtain a starting model for all the samples, and SHELXL-97[20] was used for structure refinement. The data for all the samples were corrected for absorption, extinction and refined with anisotropic displacement parameters, except for the Ga5 position which was refined with isotropic displacement parameters. All the refinement models were checked for missing symmetry elements using PLATON.[21]

Preliminary lattice checks of β-*Ln*Ni$_{1-x}$Ga$_4$ (*Ln* = Tb-Er) indicated a tetragonal cell for each phase with a ~ 4 Å, c ~ 23 Å, V ~ 400 Å^3. Data were collected on single crystals of β-*Ln*Ni$_{1-x}$Ga$_4$ (*Ln* = Tb-Er) at 298 and 100 K to investigate the nature of the disorder at the Ni2, Ga2, Ga3, Ga4, and Ga5 sites. Here we report the 100 K data, since the structural model did not change with temperature which is consistent with statistical disorder. Each data collection encompassed a full sphere of reciprocal space. The atomic positions of YNiGa$_3$Ge[22] were used as a starting model. Crystallographic data, atomic positions, and interatomic distances are provided in Tables 3.1, 3.2, and 3.3, respectively.

A Hitachi S-3600N scanning electron microscope with an energy dispersive X-ray spectrometer (SEM-EDXS) was used to analyze the elemental content of single crystals of α-*Ln*NiGa$_4$ (*Ln* = Y, Gd-Yb) and β-*Ln*Ni$_{1-x}$Ga$_4$ (*Ln* = Tb-Er). Experimental parameters included an accelerating voltage of 15 kV and a beam-to-sample distance of 15 mm. Several crystals from

multiple growths were scanned at 5 areas/crystal for 100 seconds/area. The average composition was normalized to *Ln* (*Ln* = lanthanide) to yield $LnNi_{1.0(1)}Ga_{4.0(1)}$ for α-$LnNiGa_4$ (*Ln* = Y, Gd-Yb), $LnNi_{0.9(1)}Ga_{4.0(1)}$ for *β*-$LnNi_{1-x}Ga_4$ (*Ln* = Tb-Ho), and $ErNi_{0.8(1)}Ga_{4.0(1)}$ for *β*-$ErNi_{1-x}Ga_4$. The composition of each phase obtained by SEM analysis is consistent, within error, with the refined composition determined by single crystal X-ray diffraction studies.

Table 3.1 Crystallographic Data of *β*-$LnNi_{1-x}Ga_4$ (*Ln* = Tb-Er), tetragonal, *I*4/*mmm*

Composition	***β*-$TbNi_{0.9(1)}Ga_4$**	***β*-$DyNi_{0.9(1)}Ga_4$**	***β*-$HoNi_{0.9(1)}Ga_4$**	***β*-$ErNi_{0.8(1)}Ga_4$**
a (Å)	4.1980(6)	4.1790(6)	4.1680(2)	4.1620(6)
c (Å)	23.7890(14)	23.6450(16)	23.5370(14)	23.4650(16)
V (Å^3)	419.24(9)	412.94(2)	408.89(4)	406.47(9)
Z	4	4	4	4
Size (mm^3)	0.03 x 0.03 x 0.04	0.03 x 0.03 x 0.04	0.03 x 0.03 x 0.02	0.03 x 0.03 x 0.03
θ range (˚)	3.43-29.81	3.45-29.97	3.46-30.92	3.47-30.99
μ (mm^{-1})	45.845	47.513	49.060	50.038
Temperature (K)	100(2)	100(2)	100(2)	100(2)
Reflections with $I > 2\sigma(I)$	224	223	241	229
R_{int}	0.0174	0.0201	0.0273	0.0250
h	-5 → 5	-5 → 5	-5 → 6	-6 → 6
k	-4 → 4	-4 → 5	-5 → 6	-4 → 6
l	-32 → 32	-32 → 32	-34 → 33	-32 → 33
[a]$R_1[F^2 > 2\sigma F^2)]$	0.0452	0.0295	0.0370	0.0284
[b]$wR_2(F^2)$	0.1226	0.0807	0.1008	0.0792
Parameters	25	25	25	25
GooF	1.141	1.134	1.158	1.204
Δp_{max} (e Å^{-3})	4.057	2.954	2.869	2.209
Δp_{min} (e Å^{-3})	-2.302	-1.968	-1.523	-1.905
Extinction coeff.	0.0030(8)	0.0075(8)	0.0061(9)	0.0099(9)

[a] $R_1 = \Sigma||F_o| - |F_c||/\Sigma|F_o|$
[b] $wR_2 = [\Sigma w(F_o^2 - F_c^2)^2/\Sigma w(F_o^2)^2]^{1/2}$; $w = 1/[\sigma^2(F_o^2) + 0.0833P^2 + 16.5470P]$, $w = 1/[\sigma^2(F_o^2) + 0.0408P^2 + 13.7110P]$, $w = 1/[\sigma^2(F_o^2) + 0.0574P^2 + 13.3851P]$, and $w = 1/[\sigma^2(F_o^2) + 0.0432P^2 + 9.6559P]$ at 100K for *β*-$TbNi_{0.9(1)}Ga_4$, *β*-$DyNi_{0.9(1)}Ga_4$, *β*-$HoNi_{0.9(1)}Ga_4$, and *β*-$ErNi_{0.8(1)}Ga_4$, respectively.

3.2.3 Refinement of Structural Disorder

Anomalous atomic displacement parameters and unusual residual electron density were observed for the Ni2 (4*e*), Ga2 (4*e*), and Ga4 (4*d*) positions in the initial model of *β*-$LnNi_{1-x}Ga_4$ (*Ln* = Tb-Ho). Due to unrealistic interatomic distances between Ni2 and Ga3 (~ 1.76 Å), the occupancy of the Ni2 (4*e*) site was refined freely and found to be ~ 40% for each analogue.

Table 3.2 Positional and Atomic Displacement Parameters of *β*-*Ln*$Ni_{1-x}Ga_4$ (*Ln* = Tb-Er) @ 100 K

Atom		*x*	*y*	*z*	Occ.[a]	U_{eq} ($Å^2$)[b]
***β*-$TbNi_{0.9(1)}Ga_4$**						
Tb	4*e*	0	0	0.14717(3)	1.00	0.0159(5)
Ni1	2*a*	0	0	0	1.00	0.0162(9)
Ni2	4*e*	0	0	0.2827(3)	0.43(2)	0.0343(19)
Ga1	8*g*	$^1/_2$	0	0.44519(7)	1.00	0.0198(6)
Ga2	4*e*	0	0	0.3819(3)	0.51(5)	0.0216(13)
Ga3	4*e*	0	0	0.3567(4)	0.49(5)	0.0236(16)
Ga4	4*d*	0	$^1/_2$	$^3/_4$	0.38(2)	0.033(2)
Ga5	16*n*	0	0.629(4)	0.7372(6)	0.15(2)	0.051(3)
***β*-$DyNi_{0.9(1)}Ga_4$**						
Dy	4*e*	0	0	0.14754(2)	1.00	0.0059(3)
Ni1	2*a*	0	0	0	1.00	0.0056(6)
Ni2	4*e*	0	0	0.2821(2)	0.43(2)	0.0264(13)
Ga1	8*g*	$^1/_2$	0	0.44471(5)	1.00	0.0085(4)
Ga2	4*e*	0	0	0.3801(3)	0.50(5)	0.0133(9)
Ga3	4*e*	0	0	0.3539(2)	0.50(5)	0.0092(9)
Ga4	4*d*	0	$^1/_2$	$^1/_4$	0.60(2)	0.0287(11)
Ga5	16*n*	0	0.626(4)	0.7381(7)	0.10(2)	0.044(3)
***β*-$HoNi_{0.9(1)}Ga_4$**						
Ho	4*e*	0	0	0.14766(3)	1.00	0.0171(4)
Ni1	2*a*	0	0	0	1.00	0.0164(7)
Ni2	4*e*	0	0	0.2821(3)	0.43(2)	0.0390(17)
Ga1	8*g*	$^1/_2$	0	0.55563(6)	1.00	0.0194(4)
Ga2	4*e*	0	0	0.3790(4)	0.49(5)	0.0279(12)
Ga3	4*e*	0	0	0.3535(2)	0.51(5)	0.0184(11)
Ga4	4*d*	0	$^1/_2$	$^3/_4$	0.40(2)	0.0234(19)
Ga5	16*n*	0	0.592(5)	0.7437(9)	0.15(2)	0.056(4)
***β*-$ErNi_{0.8(1)}Ga_4$**						
Er	4*e*	0	0	0.14817(2)	1.00	0.0083(3)
Ni1	2*a*	0	0	0	1.00	0.0066(5)
Ni2	4*e*	0	0	0.2835(3)	0.32(2)	0.0113(11)
Ga1	8*g*	$^1/_2$	0	0.44385(5)	1.00	0.0107(3)
Ga2	4*e*	0	0	0.3831(4)	0.30(3)	0.0130(13)
Ga3	4*e*	0	0	0.35379(17)	0.70(3)	0.0158(6)
Ga4	4*d*	0	$^1/_2$	$^3/_4$	0.84(2)	0.0332(8)
Ga5	16*n*	0	0.629(8)	0.7411(15)	0.04(2)	0.028(6)

[a]Occupancy
[b]U_{eq} is defined at one third of the trace of the orthogonalized U_{ij} tensor.

Similar to the refinement of the Ge position in $YNiGa_3Ge$,[22] the Ga2 (4*e*) was refined as a split position with ~ 50% occupancy on the Ga2 (4*e*) and Ga3 (4*e*) sites for each analogue.

Table 3.3 Interatomic Distances (Å) of β-*Ln*$Ni_{1-x}Ga_4$ (*Ln* = Tb-Er)

		β-$TbNi_{0.9(1)}Ga_4$	β-$DyNi_{0.9(1)}Ga_4$	β-$HoNi_{0.9(1)}Ga_4$	β-$ErNi_{0.8(1)}Ga_4$
Ln-*Ln*	(x4)	4.1980(6)	4.1790(6)	4.1680(2)	4.1620(6)
Ln-Ga1	(x4)	3.0386(13)	3.0206(2)	3.0058(11)	2.9988(9)
Ln-Ga2	(x4)	3.0479(17)	3.0264(3)	3.013(2)	3.033(2)
Ln-Ga3	(x4)	2.9699(4)	2.9552(3)	2.9473(2)	2.9433(3)
Ln-Ga4	(x4)	3.2233(6)	3.1993(2)	3.1852(5)	3.1686(4)
Ln-Ga5	(x8)	3.047(10)	3.0378(2)	3.10(2)	3.06(3)
Ln-Ga5	(x4)	3.161(12)	3.1232(3)	3.07(2)	3.02(3)
Ln-Ga5	(x4)	3.813(10)	3.7624(3)	3.55(2)	3.69(2)
Ni1-Ga1	(x8)	2.4710(9)	2.4648(3)	2.4612(8)	2.4630(7)
Ni2-Ga2		2.360(10)	2.3172(3)	2.280(12)	2.33(1)
Ni2-Ga3		1.760(12)	1.6977(3)	1.681(8)	1.649(8)
Ni2-Ga4	(x4)	2.239(3)	2.2231(3)	2.217(2)	2.224(2)
Ni2-Ga5	(x8)	2.423(10)	2.3928(3)	2.304(9)	2.368(16)
Ni2-Ga5	(x4)	1.628(17)	1.6343(2)	1.81(2)	1.65(3)
Ni2-Ga5	(x4)	2.683(10)	2.6593(4)	2.54(2)	2.680(7)

Refinement of the Ga (4*e*) as a single site resulted in a large atomic displacement parameter and *R* values (~ 15% higher than split site model). The disorder observed at the Ni2, Ga2 and Ga3 sites is similar to that found at equivalent sites in $YNiGa_3Ge$. An additional disordered area not seen in $YNiGa_3Ge$ was observed at the Ga4 (4*d*) site in β-*Ln*$Ni_{1-x}Ga_4$ (*Ln* = Tb-Er). The Ga4 (4*d*) was refined as split between Ga4 (4*d*) and Ga5 (16*n*) sites for the *Ln* = Tb-Ho analogues. The refinement of Ga4 as a fully occupied site resulted in large cigar-shaped thermal ellipsoids for Ga4 and a residual electron density peak (~ 6 e/Å^3) at a distance of ~ 0.8 Å from Ga4. The short interatomic distances between neighboring Ni2, Ga4, and Ga5 sites are consistent with the partially occupied model.

The occupancies of the disordered sites in β-$ErNi_{0.8(1)}Ga_4$ are noticeably different compared to β-*Ln*$Ni_{1-x}Ga_4$ (*Ln* = Tb-Ho). The Ni occupancy at the Ni2 site is decreased from ~ 43% in β-*Ln*$Ni_{1-x}Ga_4$ (*Ln* = Tb-Ho) to ~ 32% in β-$ErNi_{0.8(1)}Ga_4$. In conjunction with the decrease of Ni occupation at the Ni2 site, the occupation of Ga at the Ga4 (4*d*) site is much larger (~ 84%)

and at the Ga5 (16*n*) site is much smaller (~ 4%) when compared to *β*-*Ln*$Ni_{1-x}Ga_4$ (*Ln* = Tb-Ho). The split positions, Ga2 (4*e*) and Ga3 (4*e*), are occupied ~30 % and ~ 70 %, respectively. The differences in occupancies of the disordered sites illustrate the effects of the lanthanide contraction and mark the end of the series *β*-*Ln*$Ni_{1-x}Ga_4$ (*Ln* = Tb-Er) due to increasing structural instability with decreasing lanthanide size.

The disorder in *β*-*Ln*$Ni_{1-x}Ga_4$ (*Ln* = Tb-Er) is very similar to that found in *LnM*Ga_3Ge (*Ln* = Y, Sm, Gd, Yb; *M* = Ni, Co),[22] which was attributed to complex modulations in the $[NiGa]_2$ nets. The reciprocal lattice of *LnM*Ga_3Ge (*Ln* = Y, Sm, Gd, Tb, Er, Tm; *M* = Ni, Co) featured satellite reflections with incommensurate spacing due to structural modulation in the $[MGa]_2$ nets in the *ab* plane seen in electron diffraction.[2, 22] Although structurally very similar to *LnM*Ga_3Ge, symmetry forbidden, supercell reflections were not observed in reciprocal lattice precession images of single crystal X-ray diffraction of *β*-*Ln*$Ni_{1-x}Ga_4$ (*Ln* = Tb-Er) in data collected at long integration times (150 s/°) without overflow scans.

3.2.4 Property Measurements

Magnetization data on *β*-*Ln*$Ni_{1-x}Ga_4$ (*Ln* = Tb-Er) were obtained using a Quantum Design Physical Property Measurement System. The temperature-dependent magnetization was measured under zero-field cooled conditions from 2 K to 300 K with an applied field 0.1 T. Field-dependent magnetization was measured at 3 K sweeping between 0 to 9 T. Electrical resistance was measured on aggregates of *β*-*Ln*$Ni_{1-x}Ga_4$ (*Ln* = Tb-Er) using the standard four-probe AC technique from 3 K to 300 K at 27 Hz with excitation currents ~ 0.5 mA.

3.3 Results and Discussion

3.3.1 Structure of *β*-*Ln*$Ni_{1-x}Ga_4$ (*Ln* = Tb-Er)

β-*Ln*$Ni_{1-x}Ga_4$ (*Ln* = Tb-Er), the tetragonal polymorph, is a new, disordered variant of the Ce_2NiGa_{10} structure type as shown in Figure 3.2 (a).[14] The linear intergrowth of Ce_2NiGa_{10} consists of $BaAl_4$-type $CeGa_4$ segments of face-sharing tetragonal antiprisms $^2_\infty[Ce_{4/8}Ga_{8/4}]_2$ and CaF_2-type Ga_2Ni segments of face-sharing rectangular prisms $^2_\infty[Ga_{8/4}Ni]$.[23-24] The combination of the two segments yields $2CeGa_4 + Ga_2Ni = Ce_2NiGa_{10}$. In the case of *β*-*Ln*$Ni_{1-x}Ga_4$ (*Ln* = Tb-Er), the distorted $BaAl_4$-type segment consists of $^2_\infty[Ln_{4/8}(Ni,Ga)_{8/4}]_2$ = *Ln*$Ni_{1-x}Ga_3$ tetragonal antiprisms, where *x* represents ~ 60% Ni deficiency at the 4*e* site for *Ln* = Tb-Ho and ~ 70% Ni deficiency for *β*-$ErNi_{0.8(1)}Ga_4$, and the CaF_2-type segment consists of face-sharing rectangular prisms of $^2_\infty[NiGa_{8/4}] = NiGa_2$. The combination of these two segments yields $2LnNi_{1-x}Ga_3 + NiGa_2 = Ln_2Ni(Ni_{2-2x}Ga_8)$.

This particular distorted variant of the Ce_2NiGa_{10} structure type[14] is isotypic with $YNiGa_3Ge$[22] and $Ce_2NiAl_{6-x}Ge_{4-y}$.[25] In order to highlight the structural similarity between *Ln*MGa_3Ge (*Ln* = Y, Sm, Gd, Tb, Er, Tm; *M* = Ni, Co)[22] and *β*-*Ln*$Ni_{1-x}Ga_4$ (*Ln* = Tb-Er), the structure of *β*-*Ln*$Ni_{1-x}Ga_4$ (*Ln* = Tb-Er) can described as a stacking of *Ln*Ga planes with Ga occupational disorder, $NiGa_6$ bicapped cubes with Ga occupational disorder on the capping sites, and puckered Ni_xGa_2 square nets with a split Ga position. The disordered *Ln*Ga plane, shown in Figure 3.2 (b), is defective with only a 50% occupied Ga3 site. *Ln*-*Ln* interatomic distances are equal to the length of the crystallographic *a*-axis and are not within a typical bonding distance. The *Ln*-Ga3 interatomic distances are in good agreement with those found in *Ln*-Ga binaries (*Ln* = Tb-Er).[26-28] The Ni1-Ga1 distances in Figure 3.2 (c) are consistent with Ni-Ga atomic radii (~ 2.49 Å)[29] and with Ni-Ga binaries which range between ~ 2.47 Å to ~ 2.61 Å.[30-34] The $NiGa_6$ bicapped cubes in Figure 3.2 (c), are very similar to the bicapped MGa_6 (*M* = Ga or transition metal) cubes found in Ce_2NiGa_{10},[14] Ln_3NiGa_{10} (*Ln* = Ce-Nd),[35] $Ce_4Ni_{1.24}Ga_{17.76}$,[36] Sm_2NiGa_{12},[11]

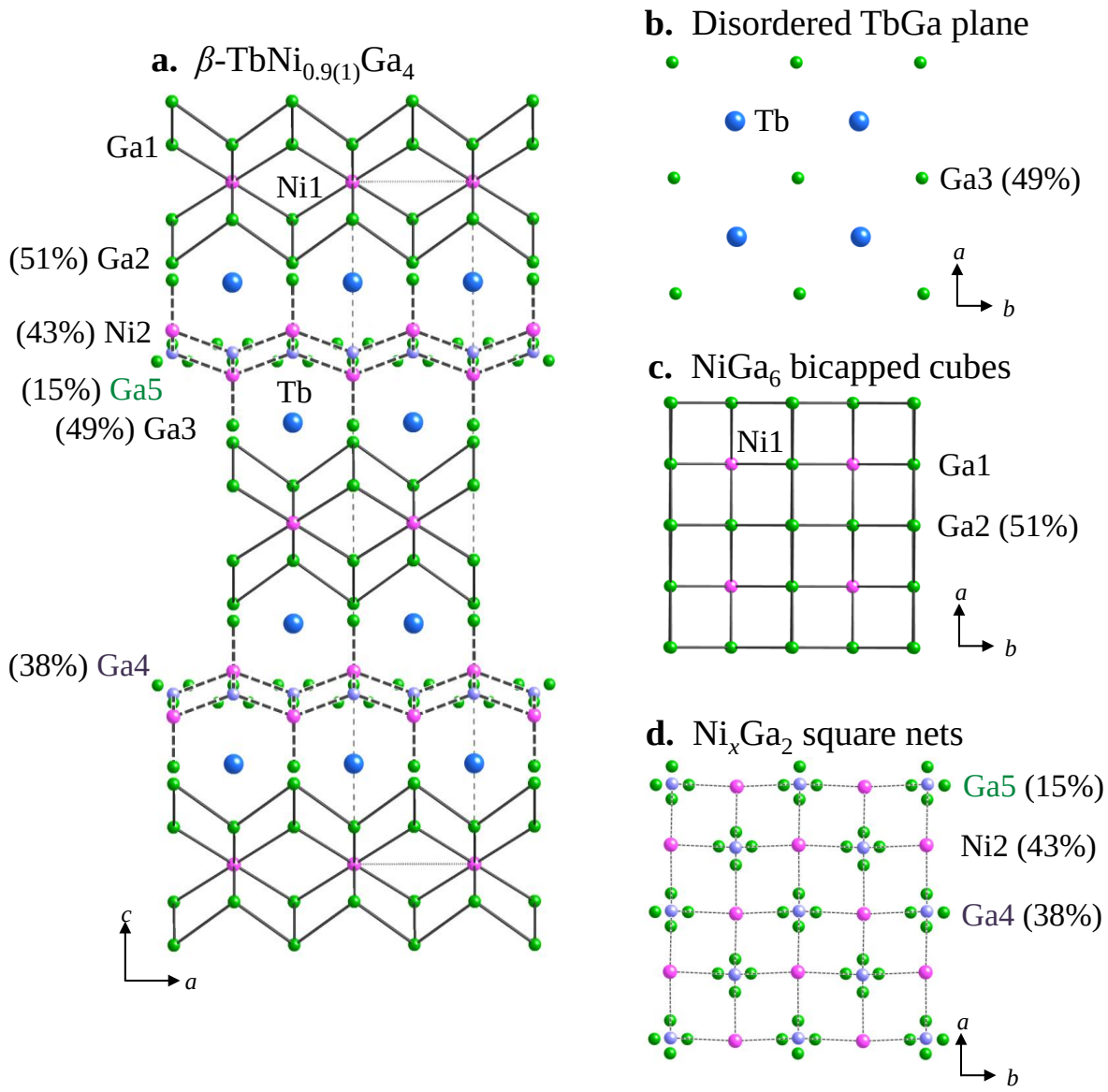

Figure 3.2 **a.** The crystal structure of β-$TbNi_{0.9(1)}Ga_4$ is shown with Tb and Ni atoms represented as blue and pink spheres. The Ga atoms are represented with green and purple spheres to highlight the disorder in this phase. **b.** Disordered TbGa planes have Ga3 49% occupied. **c.** $NiGa_6$ bicapped cubes have Ga2 51% occupied. **d.** Puckered Ni_xGa_2 square nets have Ni2, Ga4, and Ga5 occupied 43%, 38%, and 15%, respectively. Dashed lines indicate bonding between disordered sites and unless otherwise indicated, sites are 100% occupied.

$Sm_2Ni(Ni_xSi_{1-x})Al_4Si_6$,[37] $YNiGa_3Ge$,[22] $Ce_2NiAl_{6-x}Ge_{4-y}$,[25] $YbGa_5$,[38] and $Ce_2Ag_{1-x}Ga_{10-y}$.[6] The puckered Ni_xGa_2 square nets, occupied ~ 43% by Ni for *Ln* = Tb-Ho and ~ 32% for *Ln* = Er have Ni2-Ga interatomic distances between ~ 1.63 and ~ 2.68 Å as shown in Figure 3.2 (d). The shortest Ni2-Ga5 (~ 1.6 Å) and Ni2-Ga4 (~ 2.2 Å) interatomic distances are consistent with the

partial occupancy of these sites which yields empty puckered square nets in ~ 57 to 68% of the unit cells. It is important to note that the shortest Ni2-Ga5 distance and the Ni2-Ga4 distances are shorter than expected and indicate that when Ni2 is present in a unit cell, the Ga4 or closest Ga5 atoms are not present.

The two crystallographically unique Ni environments in β-*Ln*$Ni_{1-x}Ga_4$ (*Ln* = Tb-Er) make for an interesting comparison between coordination environment and the degree of structural disorder in this polymorph. Ni1 (2*a*) is in an ordered rectangular prismatic environment and the occupationally disordered Ni2 (4*e*) is in a distorted, puckered square planar environment. In the ordered Ce_2NiGa_{10} structure, the 4*e* site is occupied by Ga instead of Ni. The Ni2-Ga distances observed in β-*Ln*$Ni_{1-x}Ga_4$ (*Ln* = Tb-Er) range between ~ 1.6 Å (when Ni2 is absent) to ~ 2.5 Å (when Ni2 is present). In the ordered parent structure type, Ce_2NiGa_{10}, Ga occupies the equivalent position that Ni2 occupies in β-*Ln*$Ni_{1-x}Ga_4$ (*Ln* = Tb-Er). When Ni is present at the 4*e* site in β-*Ln*$Ni_{1-x}Ga_4$ (*Ln* = Tb-Er), the disorder observed in the Ni2 environment can be attributed to the partial occupancy of Ni and the split Ga position (4*d*/16*n*) which demonstrates a response to the presence or absence of Ni. The decreasing occupancy at the Ni2 position results in increased occupancy of Ga4 and decreased occupancy of Ga5 resulting in shorter Ni2-Ga4 and longer Ni2-Ga5 distances compared to the other β-*Ln*$Ni_{1-x}Ga_4$ (*Ln* = Tb-Ho) analogues. The degree of disorder and the observation that the β-$ErNi_{0.8(1)}Ga_4$ analogue shows a notable decrease in occupancy at the Ni2 position, coupled with all unsuccessful attempts to grow a β-$TmNi_{1-x}Ga_4$ analogue, suggest that β-$ErNi_{0.8(1)}Ga_4$ is the terminal stable member. The decrease in the structural frustration can be seen in the increasing *Ln*-Ga5 and Ni2-Ga4/Ga5 interatomic distances when comparing β-$HoNi_{0.9(1)}Ga_4$ and β-$ErNi_{0.8(1)}Ga_4$. As the 4*e* – 4*d*/16*n* (Ni2 – Ga4/Ga5) environment in β-*Ln*$Ni_{1-x}Ga_4$ is limited in its degree of disorder, the Ga4/Ga5 positions

become increasing restricted which effectively render Ni incapable of populating the 4*e* position in the β-$TmNi_{1-x}Ga_4$ analogue.

The disorder in the local environment of the *Ln* in β-*Ln*$Ni_{1-x}Ga_4$ (*Ln* = Tb-Er) results in a varying local electronic environment of the *Ln* which manifests as magnetic frustration; the spin-glass behavior observed in $Ce_2Ag_{1-x}Ga_{10-y}$,[6] Ce_2CuSi_3,[7] and Ce_2CuGe_3[8] has been attributed to such structural disorder in the local Ln^{3+} environments. Frustration due to structural disorder in β-*Ln*$Ni_{1-x}Ga_4$ (*Ln* = Tb-Er) is consistent with the large discrepancy between T_N and θ_W in β-*Ln*$Ni_{1-x}Ga_4$ (*Ln* = Tb-Er), as shown below in Table 3.4.

3.3.2 Magnetic and Transport Properties of β-*Ln*$Ni_{1-x}Ga_4$ (*Ln* = Tb-Er)

Figure 3.3 shows the temperature dependent magnetic susceptibility, χ_m, of β-*Ln*$Ni_{1-x}Ga_4$ (*Ln* = Tb-Er) measured under zero-field-cooled conditions from 2 K to 300 K with an applied field of 0.1 T perpendicular to the direction of the plate, and the inset of Figure 3.3 shows the inverse susceptibility, χ_m^{-1}, for the same series. All analogues, Tb-Er, were fit with a modified Curie-Weiss equation of the form: $\chi(T) = \chi_0 + C/(T - \theta_W)$ where C is the Curie constant, θ_W is the Weiss temperature (K), and χ_0 is a constant, representative of any Larmor diamagnetic, Pauli paramagnetic, and background contributions to the magnetic susceptibility. In all cases, the

Table 3.4 Magnetic Properties of β-*Ln*$Ni_{1-x}Ga_4$ (*Ln* = Tb-Er)

	T_N (K)	μ_{eff} (μ_B) calculated	μ_{eff} (μ_B) experimental	θ_W (K)	T (K)
β-$TbNi_{0.9(1)}Ga_4$	7	9.72	9.8(1)	-43.6(5)	25-300
β-$DyNi_{0.9(1)}Ga_4$	3.5	10.65	10.5(1)	-22.7(2)	25-300
β-$HoNi_{0.9(1)}Ga_4$	-----	10.61	10.5(2)	-14.1(5)	20-300
β-$ErNi_{0.8(1)}Ga_4$	7	9.58	8.9(2)	-6.1(1)	20-300

modified Curie-Weiss equation was fit over the linear region of χ_m^{-1}. Table 3.4 gives a summary of the magnetic properties of β-*Ln*$Ni_{1-x}Ga_4$ (*Ln* = Tb-Er), including the T_N, μ_{eff} (calculated and

experimental), θ_W, and fit range. When making reference to the applied field and its direction relative to the *c*-axis, crystals grew as plate-like aggregates, and directions were assigned as the *c*-axis being perpendicular to the plates for β-*Ln*$Ni_{1-x}Ga_4$ (*Ln* = Tb-Er).

β-*Ln*$Ni_{1-x}Ga_4$ (*Ln* = Tb-Er) undergoes an antiferromagnetic transition (T_N) at ~7, 3.5, and 7 K, respectively, with the Ho analogue remaining paramagnetic down to 2 K with H = 0.1 T. The inset of Figure 3.3 shows the inverse magnetic susceptibility, $\chi_m^{-1}(T)$. Above 20 K for $H \| c$, the series exhibits paramagnetic Curie-Weiss type behavior. The magnetic properties of β-$TbNi_{0.9(1)}Ga_4$ are similar to that of $TbNiGa_3Ge$ (T_N ~ 5 K and observed μ_{sat} ~ 3 μ_B).[22] Fitting the data above 25 K for Tb and Dy and above 20 K for Ho and Er, respectively, resulted in θ_W = –43.6(5), –22.7(2), –14.1(5), and –6.1(1) K for Tb, Dy, Ho, and Er, respectively. The negative θ_W values indicate that antiferromagnetic coupling dominates and are consistent with the ordering observed for $TbNi_{0.9(1)}Ga_4$, $DyNi_{0.9(1)}Ga_4$, and $ErNi_{0.9(1)}Ga_4$. The magnetic moments recovered, 9.8(1), 10.5(1), 10.5(2), and 8.9(2) μ_B for Tb, Dy, Ho, and Er analogues of β-*Ln*$Ni_{1-x}Ga_4$ are in good agreement with the calculated spin-only effective moments of 9.72, 10.65, 10.61, and 9.5 μ_B for trivalent Tb, Dy, Ho, and Er, respectively. In all cases, the recovered moment is reflective of the respective Ln^{3+} (*Ln* = Tb-Er) moment, which

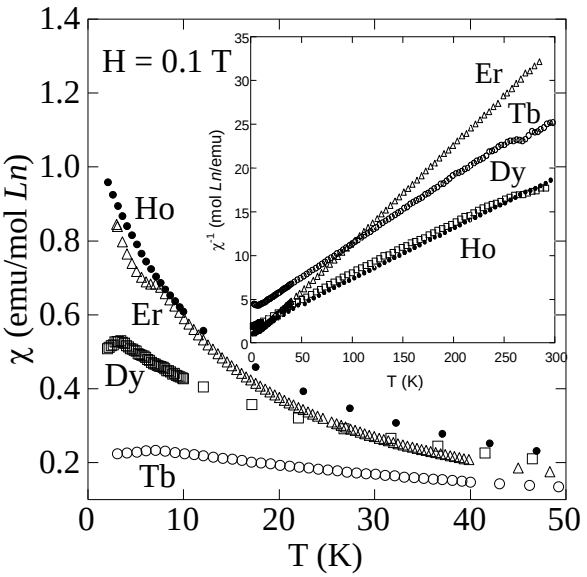

Figure 3.3 Magnetic susceptibility, χ_m = M/H (emu/mol *Ln*), as a function of temperature, T (K), is plotted with an applied field of H = 0.1 T for β-$TbNi_{0.9(1)}Ga_4$ (open circles), β-$DyNi_{0.9(1)}Ga_4$ (open squares), β-$HoNi_{0.9(1)}Ga_4$ (closed circles), and β-$ErNi_{0.8(1)}Ga_4$ (open triangles). The inset shows the inverse magnetic susceptibility, χ_m^{-1} = H/M (mol *Ln*/emu).

indicates that Ni atoms show no localized magnetic moment and their contribution to the magnetism is diamagnetic. Frustration values, $|\theta_W|/T_N$, of 2-5 are considered typical for an antiferromagnetic system.[39] The frustration parameters, 6.2, 6.5, >10, and 0.9 for Tb, Dy, Ho and Er analogues respectively, indicate increasing magnetic frustration across the series β-*Ln*$Ni_{0.9(1)}Ga_4$ (*Ln* = Tb-Ho) followed by a decrease in magnetic frustration in β-$ErNi_{0.8(1)}Ga_4$.[39] The decrease in magnetic frustration on moving across the series β-*Ln*$Ni_{1-x}Ga_4$ (*Ln* = Tb, Dy, Ho and Er) is consistent with decreasing structural frustration as seen in the increasing *Ln*-Ga4/Ga5 interatomic distances when comparing β-$HoNi_{0.9(1)}Ga_4$ and β-$ErNi_{0.8(1)}Ga_4$.

3.3.3 Comparison of Defect Variants of the Ce_2NiGa_{10}-structure Type: $Ce_2Ag_{0.7(1)}Ga_{9.1(1)}$ and β-*Ln*$Ni_{1-x}Ga_4$ (*Ln* = Tb-Er).

Both $Ce_2Ag_{0.7(1)}Ga_{9.1(1)}$ and β-*Ln*$Ni_{1-x}Ga_4$ (*Ln* = Tb-Er) are defect variants of the Ce_2NiGa_{10} structure type.[14] The structural disorder in both phases can be attributed to the coordination preference of transition metals (Ag and Ni) and Ga. In $Ce_2Ag_{0.7(1)}Ga_{9.1(1)}$, Ni is replaced by Ag, and the resulting disorder can be attributed to the tendency of Ga to achieve an optimum coordination of four, which results in severe disorder surrounding the Ga5 site. In β-*Ln*$Ni_{1-x}Ga_4$ (*Ln* = Tb-Er), some of the Ga atoms are replaced by additional Ni atoms, which results in severe disorder surrounding the Ni2 site. Both $Ce_2Ag_{0.7(1)}Ga_{9.1(1)}$ and β-*Ln*$Ni_{1-x}Ga_4$ (*Ln* = Tb-Er) phases exhibit suppression of magnetic ordering below the θ_W temperature as determined by magnetic susceptibility measurements. The magnetic behavior in both $Ce_2Ag_{0.7(1)}Ga_{9.1(1)}$ and β-*Ln*$Ni_{1-x}Ga_4$ (*Ln* = Tb-Er) phases can be directly attributed to the disorder in the structures. In $Ce_2Ag_{0.7(1)}Ga_{9.1(1)}$ the magnetic frustration and subsequent spin-glassy magnetic behavior can be attributed to structural disorder in the Ga-network. The magnetic frustration in β-*Ln*$Ni_{1-x}Ga_4$ (*Ln* = Tb-Ho) phases can also be linked to the structural disorder in

the Ga-network. The decrease in the magnetic frustration on comparing β-*Ln*$Ni_{1-x}Ga_4$ (*Ln* = Ho-Er) can be attributed to the decreasing structural disorder in β-*Ln*$Ni_{1-x}Ga_4$ (*Ln* = Ho-Er).

3.4 Conclusion

We have successfully grown two polymorphs of *Ln*$NiGa_4$ (α and β).[12] β-*Ln*$Ni_{1-x}Ga_4$ (*Ln* = Tb-Er), a defect variant of the Ce_2NiGa_{10}-structure type,[14] is isotypic to *Ln*$NiGa_3Ge$ (*Ln* = Y, Sm, Gd, Tb, Er, Tm)[22] with an additional split Ga site. The structural distortion found in β-*Ln*$Ni_{1-x}Ga_4$ (*Ln* = Tb-Er) can be attributed to the Ni occupation at the 4*e* site which induces a distortion in the surrounding Ga environment. The decreasing magnetic frustration on moving from the Ho to Er analogues may be attributed to the decreasing structural frustration across the series observed as increasing *Ln*-Ga4/Ga5 interatomic distances.

3.5 References

(1) Gray, D. L.; Francisco, M. C.; Kanatzidis, M. G., Distortion and charge density wave in the Ga square net coupled to the site occupancy wave in $YCo_{0.88}Ga_3Ge$. *Inorg. Chem.* **2008,** *47*, 7243-7248.

(2) Zhuravleva, M. A.; Evain, M.; Petricek, V.; Kanatzidis, M. G., $GdCo_{1-x}Ga_3Ge$: charge density wave in a Ga square net. *J. Am. Chem. Soc.* **2007,** *129*, 3082-3083.

(3) Troc, R.; Rogl, P.; Tran, V. H.; Czopnik, A., Magnetotransport and heat capacity in ternary compounds $U_3M_2M'_3$, *M* = Al, Ga; *M*' = Si, Ge *J. Solid State Chem.* **2001,** *158*, 227-235.

(4) Salvador, J. R.; Guo, F.; Hogan, T.; Kanatzidis, M. G., Zero thermal expansion in YbGaGe due to an electronic valence transition. *Nature* **2003,** *425*, 702-705.

(5) Margadonna, S.; Prassides, L.; Fitch, A. N.; Salvador, J. R.; Kanatzidis, M. G., Valence instabilties, phase transitions, and abrupt lattice expansion at 5 K in the YbGaGe system. *J. Am. Chem. Soc.* **2004,** *126*, 4498-4499.

(6) Menard, M. C.; Xiong, Y.; Karki, A. B.; Drake, B. L.; Adams, P. W.; Fronczek, F. R.; Young, D. P.; Chan, J. Y., Synthesis, structure, and characterization of $Ln_2Ag_{1-x}Ga_{10-y}$ (*Ln* = La, Ce). *J. Solid State Chem.* **2010,** *183*, 1935-1942.

(7) Hwang, J. S.; Lin, K. J.; Tien, C., Antiferromagnetism and mass-enhanced behavior in Ce_2CuSi_3. *Solid State Commun.* **1996,** *100*, 169-172.

(8) Tien, C.; Feng, C. H.; Wur, C. S.; Lu, J. J., Ce_2CuGe_3: a nonmagnetic atom-disorder spin glass. *Phys. Rev. B* **2000,** *61* (18), 12151.

(9) Drake, B. L.; Kangas, M. J.; Haldolaarachchige, N.; Xiong, Y.; Adams, P. W.; Young, D. P.; Chan, J. Y., Crystal growth, structure, and physical properties of *Ln*$(Ag,Al,Si)_2$ (*Ln* = Ce and Gd). *J. Phys: Cond. Mat.* **2010,** *22*, 426002.

(10) Mentink, S. A. M.; Nieuwenhuys, G. J.; Menovsky, A. A.; Mydosh, J. A.; Tou, H.; Kitaoka, Y., Direct evidence for critical exchange coupling via Al layers in the heavy-fermion compound $CePd_2Al_3$. *Phys. Rev. B* **1994,** *49* (22), 15759-15763.

(11) Chen, X. Z.; Small, P.; Sportouch, S.; Zhuravleva, M.; Brazis, P.; Kannewurf, C. R.; Kanatzidis, M. G., Molten Ga as a solvent for exploratory synthesis: the new ternary polygallide Sm_2NiGa_{12}. *Chem. Mater.* **2000,** *12* (2000), 2520-2522.

(12) Romaka, V. A.; Grin, Y. N.; Yarmolyuk, Y. P., Magnetic and structural characterization of compounds of *Ln*$NiGa_4$ (*Ln* = Nd, Sm, Gd-Lu, Y). *Ukr. Fiz. Zh.* **1983,** *28*, 1095-1097.

(13) Rykhal, R. M.; Zarechnyuk, O. S.; Yarmolyuk, Y. P., Crystal structure of the compounds $YNiAl_4$ and $YNiAl_2$. *Sov. Phys. Crystallogr.* **1972** *17*, 453-455.

(14) Yarmolyuk, Y. P.; Grin, Y. N.; Rozhdestvenskaya, I. V.; Usov, O. A.; Kuzmin, A. M.; Bruskov, V. A.; Gladyshevskij, E. I., Crystal chemistry of series of inhomogeneous linear structures. III. the crystal structures of $Ce_2Ga_{10}Ni$ and $La_2Ga_{10}Ni$. *Kristallografiya* **1982,** *27*, 599-600.

(15) Thomas, K. R.; Cho, J. Y.; Millican, J. N.; Hembree, R. D.; Moldovan, M.; Karki, A.; Young, D. P.; Chan, J. Y., Crystal growth and physical properties of Ln_2MGa_{12} (*Ln* = Pr, Nd, and Sm; *M* = Ni, Cu). *J. Cryst. Growth* **2010,** *312*, 1098-1103.

(16) Grin, Y.; Hiebl, K.; Rogl, P., Magnetism and structural chemsitry of ternary gallides $RENi_xGa_{4-x}$ (RE = La, Ce, Pr, Nd, Sm, Gd, Tb) and $LaCo_{0.5}Ga_{3.5}$. *J. Less-Common Met.* **1990,** *162*, 361-369.

(17) Vasylehko, L.; Schnelle, W.; Schmidt, M.; Burkhardt, U.; Borrmann, H.; Schwarz, U.; Grin, Y. N., Valence behavior of ytterbium in $YbNiGa_4$. *J. Alloys Comp.* **2006,** *416*, 35-42.

(18) Pelleg, J.; Kimmel, G.; Dayan, D., *R*Ga_6 (*R* = Rare Earth Atom), a common intermetallic compound of the *R*-Ga systems. *J. Less-Common Met.* **1981,** *81*, 33-44.

(19) Altomare, A.; Burla, M. C.; Camalli, M.; Cascarano, G.; Giacovazzo, C.; Guagliardi, A.; Polidori, G., SIR92 - a program for automatic solution of crystal structures by direct methods. *J. Appl. Crystallogr.* **1994,** *27*, 435.

(20) Sheldrick, G. M., A short history of SHELX. *Acta Crystallogr. Sect. A.: Found Crystallogr.* **2008,** *A64*, 112-122.

(21) Spek, A. L., PLATON, a multipurpose crystallographic tool. *J. Appl. Crystallogr.* **2003,** *36*, 7-13.

(22) Zhuravleva, M. A.; Pcionek, R. J.; Wang, X.; Schultz, A. J.; Kanatzidis, M. G., *ReM*Ga_3Ge and $Re_3Ni_3Ga_8Ge_3$ (*M* = Ni, Co; *Re* = rare-earth element): new intermetallics synthesized in liquid gallium. x-ray, electron, and neutron strucutre determination and magnetism. *Inorg. Chem.* **2003,** *42*, 6412-6424.

(23) Parthe, E., *Modern perspectives in inorganic chemistry*. Kluwer Academic Publishers: Boston, 1992; Vol. 382, p 77-95.

(24) Grin, Y.; Yarmolyuk, Y. P.; Gladyshevskii, E. I., The crystal chemistry of series of inhomogeneous linear structures. I. symmetry and numberic symbols of the structures composed of fragments of the strucutre types $BaAl_4$, CaF_2, AlB_2, Cu, α-Fe, and α-Po. *Sov. Phys. Crystallogr.* **1982,** *27*, 413-417.

(25) Sieve, B.; Trikalitis, P. N.; Kanatzidis, M. G., Quaternary germanides formed in molten aluminum: $Tb_2NiAl_4Ge_2$ and $Ce_2NiAl_{6-x}Ge_{4-y}$ (x~0.24, y~1.34). *Z. Anorg. Allg. Chem* **2002,** *628*, 1568-1574.

(26) Cirafici, S.; Franceschi, E., Stacking of close-packed AB_3 layers in RGa_3 compounds (*R* = heavy rare earth) *J. Less-Common Met.* **1981,** *77*, 269-280.

(27) Palenzona, A.; Franceschi, E., The crystal structure of rare-earth gallides (RE_5Ga_3) *J. Less-Common Met.* **1968,** *14*, 47-53.

(28) Haszko, S. E., Rare-earth gallium compounds having the aluminum-boride structure. *T. Metall. Soc. Aime.* **1961,** *221*, 201-202.

(29) Emsley, J., *The Elements*. 3rd ed.; Oxford University Press: New York, 1998.

(30) Hellner, E., The system nickel-gallium. *Z. Metallkd.* **1950,** *41*, 480-484.

(31) Bhan, S.; Schubert, K., Ueber die struktur von phasen mit kupfer unterstruktur in einigen T-B legierungen (T = Ni, Pd, Pt; B = Ga, In, Tl, Pb, Sb, Bi). *J. Less-Common Met.* **1974,** *36*, 15-30.

(32) Ellner, M.; Bhan, S.; Schubert, K., Kristallstruktur von $Ni_{13}Ga_9$ und zwei isotypen. *J. Less-Common Met.* **1969,** *19*, 245-252.

(33) Häussermann, E.; Elding-Pontén, M.; Svensson, C.; Lidin, S., Compounds with the Ir_3Ge_7 structure type: interpenetrating frameworks with flexible bonding properties. *Chem.-Eur. J.* **1998,** *4*, 1007-1015.

(34) Schmetterer, C.; Flandorfer, H.; Lengauer, C. L.; Bros, J.-P.; Ipser, H., The system Ga-Ni: a new investigation of the Ga-rich part. *Intermetallics* **2010,** *18*, 277-285.

(35) Grin, Y. N.; Yarmolyuk, Y. P.; Rozhdestvenskaia, I. V., The crystal chemistry of a series of inhomogeneous linear structures: the crystal structure of the compounds $R_3Ga_{10}Ni$ (*R*= Ce, Pr, Nd). *Sov. Phys. Crystallogr.* **1983,** *28*, 477-479.

(36) Grin, Y. N.; Yarmolyuk, Y. P.; Usov, O. A.; Kuz'min, A. M.; Bruskov, V. A., The crystal chemistry of series of inhomogeneous structure. the crystal structure of the compounds $Ce_4Ga_{17}Ni_2$ and $Nd_4Ga_{17}Ni_2$. *Sov. Phys. Crystallogr.* **1983,** *28* 710-711.

(37) Chen, X. Z.; Sportouch, S.; Sieve, B.; Brazis, P.; Kannewurf, C. R.; Cowen, J. A.; Patschke, R.; Kanatzidis, M. G., Exploratory synthesis with molten aluminum as a solvent and routes to multinary aluminum silicides. $Sm_2Ni(Ni_xSi_{1-x})Al_4Si_6$ (x = 0.18−0.27): a new silicide with a ferromagnetic transition at 17.5 K. *Chem. Mater.* **1998,** *10*, 3202-3211.

(38) Giedigkeit, R.; Niewa, R.; Schnelle, W.; Grin, Y.; Kniep, R., On the binary compound $YbGa_5$. *Z. Anorg. Allg. Chem.* **2002,** *628*, 1692-1696.

(39) Greedan, J. E., Geometrically frustrated magnetic materials. *J. Mater. Chem.* **2001,** *11*, 37-53.

CHAPTER 4. HIGH RESOLUTION SYNCHROTRON STUDIES AND MAGNETIC PROPERTIES OF FRUSTRATED ANTIFERROMAGNETS MAl$_2$S$_4$ (M^{2+} = Mn^{2+}, Fe^{2+}, Co^{2+})[1] AND Ni$_{0.68}$Al$_2$S$_{3.78}$[2]

4.1 Introduction

Primary interest in two-dimensional (2-*d*) triangular lattice antiferromagnets arises from the inherent lattice frustration resulting in the suppression of long range magnetic order to temperatures much lower than expected due to competing interactions between magnetic moments.[1-4] The combination of frustration and 2-*d* magnetism can suppress magnetic ordering and allow for the investigation of the quantum fluctuations that determine the possible ground states of the system.[5] Quantum fluctuations are low temperature phenomena which leave fingerprints on room temperature physical properties. Understanding these ground states is critical for understanding the behavior at application temperatures and can lead to the design of new, exotic materials.[6-7]

Frustration when coupled with complex parameters such as the charge, spin, orbital and lattice can lead to exotic phenomena and ground states. Various polytypes of the $ZnIn_2S_4$ structure type have been investigated due to the possible geometric frustration of magnetic moments on a triangular lattice. The $CuIr_2S_4$ and $MgTi_2O_4$ phases form spin dimers and have been correlated to charge ordering and frustration.[8-9] $FeSc_2S_4$, a spin-orbital liquid with one of the largest spin-frustration parameters > 900, exhibits complex spin-orbital coupling in addition to frustration.[10] Electric polarization induced by an external magnetic field in $CdCr_2S_4$ and $HgCr_2S_4$ appears with and without complex spiral magnetic ordering, respectively.[11-12] Many

---

1. Reprinted by permission of the American Chemical Society: Menard, M. C.; Ishii, R.; Higo, T.; Nakatsuji, S.; Nishibori, E.; Sawa, H.; Chan, J. Y., High-resolution synchrotron studies and magnetic properties of frustrated antiferromagnets MAl$_2$S$_4$ (M^{2+} = Mn^{2+}, Fe^{2+}, Co^{2+}). *Chem. Mater.* **2011,** *23,* 3086-3094. "Copyright 2011 American Chemical Society."

2. Reprinted by permission of the American Physical Society: Higo, T.; Ishii, R.; Menard, M. C.; Chan, J. Y.; Yamaguchi, H.; Hagiwara, M.; Nakatsuji, S., Magnetic properties of the quasi-two-dimensional antiferromagnet $Ni_{0.7}Al_2S_{3.7}$. *Phys. Rev. B* **2011,** *In Press.*"Copyright 2011 by the American Physical Society."

spinels have been studied with various properties due to geometrical frustration of the magnetic sublattice. Structurally related to the spinel structure type, $FeGa_2S_4$[13]- and $ZnIn_2S_4$[14]-type compounds are good candidates for the investigation of quantum fluctuations given the two dimensionality of the structure in addition to the triangular magnetic sublattice. Although the Ga-analogues, MGa_2S_4 (M = Mn^{2+}, Fe^{2+}, Co^{2+}), adopt one of the $ZnIn_2S_4$ polytypes, previous attempts to grow the MAl_2S_4 (M^{2+} = Mn^{2+}, Fe^{2+}, Co^{2+}, Ni^{2+}) have failed reportedly due to the polarizing capacity of Al^{3+} in these compounds to induce structural instability in the sulfide lattice which results in the formation of a different structure.[15]

The layered $NiGa_2S_4$ ($FeGa_2S_4$-type) structure is the first reported example of a low spin quasi-2-*d* antiferromagnet with a perfect triangular lattice.[4] Very interestingly, the Ni^{2+} (S = 1) spins do not show any long range magnetic ordering down to 30 mK despite the relatively large antiferromagnetic Weiss temperature ~ 80 K. Instead, the Ni^{2+} spins exhibit spin glass freezing at T^* = 8.5 K and show a 2-*d* spin wave-like coherent behavior at T < 3 K.[7] Spin-dependent impurity effects in $Ni_{1-x}M_xGa_2S_4$ (M^{2+} = Mn^{2+}, Fe^{2+}, Co^{2+}, and Zn^{2+}) indicate the integer size of the Heisenberg spins is important for 2-*d* spin wave-like coherent behavior.[16] The high-spin (S = 2) $FeGa_2S_4$ has been described as a frustrated (θ = -160 K) quasi-2-*d* triangular Heisenberg antiferromagnet exhibiting strong spin freezing at 16 K without developing magnetic long range order.[13, 17-20] Regarding the Mn- and Co-analogues, various polytypes of $MnGa_2S_4$ and $CoGa_2S_4$ have been reported, but not of the $FeGa_2S_4$- or $ZnIn_2S_4$ (*IIIa*)-types.[21-24] In addition to geometrical frustration, magnetic frustration can arise due to site disorder as observed in the spinel-type $CoAl_{2-x}Ga_xO_4$ where doping of Ga^{3+} at both the octahedral and tetrahedral sites results in an increasingly diluted magnetic sublattice at concentrations $0.4 \leq x \leq 2.0$.[25-26]

Here we report the growth and characterization of single crystals of MAl$_2$S$_4$ (M^{2+} = Mn^{2+}, Fe^{2+}, Co^{2+}, Ni^{2+}), which exhibit magnetic dilution due to mixing of (M^{2+} = Mn^{2+}, Fe^{2+}, Co^{2+}) and Al^{3+} in two interpenetrating, triangular magnetic sublattices and partial occupancy of the Ni^{2+} and S^{2-} in the octahedral environment for the Ni-analogue. These phases are characterized and compared to investigate the effects of spin on structurally similar systems exhibiting magnetic frustration and the site disorder effects due to mixing on crystal chemistry and physical properties. Structural and magnetic comparison between MGa$_2$S$_4$ (M^{2+} = Fe^{2+}, Ni^{2+}) and MAl$_2$S$_4$ (M^{2+} = Mn^{2+}, Fe^{2+}, Co^{2+}) can be used to isolate the effects of low dimensionality and geometrical frustration from effects of site disorder.

4.2 Experimental

4.2.1 Synthesis of MAl$_2$S$_4$ (M^{2+} = Mn^{2+}, Fe^{2+}, Co^{2+}) and Ni$_{0.68}$Al$_2$S$_{3.78}$

Polycrystalline samples of MAl$_2$S$_4$ (M^{2+} = Mn^{2+}, Fe^{2+}, Co^{2+}, Ni^{2+})[27] were synthesized by annealing (M = Mn, Fe, Co, Ni) with Al and S in evacuated fused-silica ampoules for 1 - 2 days at 900 °C. Single crystals were prepared by the chemical vapor transport (CVT) method in evacuated fused-silica ampoules using the polycrystalline samples obtained by the above procedure. The transport reactions were carried out in a temperature gradient of 850 - 950 °C for 1 - 2 weeks using a transport agent concentration of 3 mg/cm^3 iodine. Crystals, shown in Figure 4.1, grew as dark brown (light brown for MnAl$_2$S$_4$), hexagonal, micaceous plates and cleave easily.

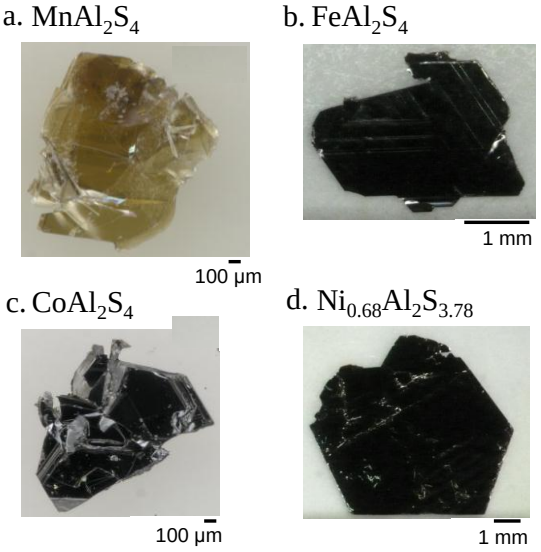

Figure 4.1 Single crystals of MAl$_2$S$_4$ (M = Mn^{2+}, Fe^{2+}, Co^{2+}) and Ni$_{0.68}$Al$_2$S$_{3.78}$.

Crystals are very hygroscopic and react readily with water in the surrounding air to yield Al_2O_3, *M*S (M^{2+} = Mn^{2+}, Fe^{2+}, Co^{2+}, Ni^{2+}), and H_2S. The distinct smell of H_2S is indicative of crystal degradation.

4.2.2 Elemental Analysis

Scanning electron microscopy with energy-dispersive X-ray (SEM-EDX) measurements were performed to confirm the exact composition of MAl_2S_4 (M^{2+} = Mn^{2+}, Fe^{2+}, Co^{2+}, Ni^{2+}).[27] Measurements were collected on JSM-5600 (JEOL) instruments. The accelerating voltage was 15 kV with a beam to sample distance of 20 mm. An average of 10 scans with a size of 10 μm x 10 μm was performed on each single crystal. The mole ratio of *M* : Al : S, normalized to an Al concentration of 2 moles, was obtained by fitting intensity as a function of energy to yield $Mn_{0.99(1)}Al_2S_{4.07(1)}$, $Fe_{0.92(1)}Al_2S_{3.97(1)}$, $Co_{0.97(1)}Al_2S_{4.02(1)}$, and $Ni_{0.72(1)}Al_2S_{3.68(1)}$ which are consistent with the refined compositions determined by X-ray diffraction.

4.2.3 Single Crystal X-ray Diffraction

Data collection on single crystals using an Enraf Nonius diffractometer equipped with a Kappa CCD detector (Mo Kα radiation, λ = 0.71703 Å) was attempted on several crystals with long scan times. Since the single crystals were weakly diffracting, synchrotron crystallographic data were collected at the Advanced Light Source Synchrotron facility in Berkeley California at the Small-Crystal Crystallography Beamline 11.3.1 (Lawrence Berkeley National Laboratory). Intensity data were collected at 150 K on a D8 goniostat equipped with a Bruker APEXII CCD detector using synchrotron radiation tuned to λ = 0.7749 Å. A series of 1 s frames measured at 0.2˚ increments of ω were collected to calculate a unit cell. Data collection frames were measured for a duration of 1 s at 0.3˚ intervals of ω with a maximum 2θ value of ~ 60˚. The data were collected using the program APEX2[28] and processed using the SAINT[28] routine within

APEX2. The data were corrected for absorption and beam corrections based on the multi-scan technique as implemented in SADABS.[29] Direct methods were used to solve the structures,[30] and the models were refined using SHELX97[31] with extinction coefficients and anisotropic displacement parameters. Crystallographic data, atomic positions, and bond distances for all compounds studied are provided in Tables 4.1, 4.2, and 4.3, respectively.

Table 4.1 Crystallographic Data of MAl_2S_4 (M^{2+} = Mn^{2+}, Fe^{2+}, Co^{2+}) and $Ni_{0.68}Al_2S_{3.78}$

Crystal data				
Refined composition	$MnAl_2S_4$	$FeAl_2S_4$	$CoAl_2S_4$	$Ni_{0.68}Al_2S_{3.78}$
Space group	*R*3*m*	*P*-3*m*1	*P*-3*m*1	*P*-3*m*1
a (Å)	3.7013(13)	3.6825(13)	3.6200(13)	3.6060(13)
c (Å)	36.4160(12)	12.1920(12)	11.9700(12)	11.98500(12)
V (Å^3)	432.1(2)	143.18(7)	135.84(7)	134.96(7)
Z	1	1	1	1
Crystal size (mm^3)	0.01 x 0.04 x 0.10	0.02 x 0.04 x 0.005	0.01 x 0.03 x 0.04	0.02 x 0.11 x 0.14
Data Collection				
Temperature (K)	150(2)	150(2)	150(2)	150(2)
Measured reflections	1071	1506	1420	1296
Independent reflections	283	148	141	140
Reflections with I > 2σ(I)	272	113	141	136
R_{int}	0.0420	0.1238	0.0477	0.0267
h	-4 → 4	-4 → 4	-4 → 4	-4 → 4
k	-4 → 4	-4 → 4	-4 → 4	-4 → 4
l	-43 → 44	-14 → 14	-14 → 14	-14 → 14
Refinement				
θ range (˚)	3.66-28.95	3.64-28.92	3.71-28.99	5.10-26.35
[a]$R_1[F^2 > 2\sigma F^2)]$	0.0210	0.0566	0.0285	0.0616
[b]$wR_2(F^2)$	0.0513	0.1262	0.0533	0.1484
Parameters	23	13	16	13
GooF on F^2	1.021	1.134	1.129	1.256
μ (mm^{-1})	4.150	5.371	5.965	4.132
Δp_{max} (e Å^{-3})	0.242	1.368	0.563	2.111
Δp_{min} (e Å^{-3})	-0.377	-0.669	-0.798	-1.795
Extinction coefficient	0.00	0.47(9)	0.00	0.28(7)

[a]$R_1 = \Sigma||F_0| - |F_c||/\Sigma|F_0|$

[b]$wR_2 = [\Sigma w(F_o^2 - F_c^2)^2/\Sigma w(F_0^2)^2]^{1/2}$; $P = (F_o^2 + 2F_c^2)/3$

4.2.4 Refinement of MAl_2S_4 (M = Mn, Fe, Co) and $Ni_{0.68}Al_2S_{3.78}$

Due to similar lattice parameters, the atomic positions of the hexagonal polymorph of $ZnIn_2S_4$ (*IIIa*)[14] were used as an initial structural model in determining the atomic positions of

Table 4.2 Positional and Atomic Displacement Parameters of MAl_2S_4 (M^{2+} = Mn^{2+}, Fe^{2+}, Co^{2+}) and $Ni_{0.68}Al_2S_{3.78}$ @ 150 K

Atom			*x*	*y*	*z*	Occ.[a]	U_{eq} ($Å^2$)[b]
$MnAl_2S_4$							
*M*1	3*a*	(Mn1 (22(1)%) + Al1 (78(1)%))	0	0	0.60228(11)	1.00	0.0129(12)
*M*2	3*a*	(Mn2 (32(2)%) + Al2 (68(2)%))	0	0	0.07142(9)	1.00	0.0131(12)
*M*3	3*a*	(Mn3 (43(2)%) + Al3 (57(2)%))	0	0	0.83723(15)	1.00	0.0133(3)
S1	3*a*		0	0	0.95996(12)	1.00	0.0207(14)
S2	3*a*		0	0	0.71512(11)	1.00	0.0174(14)
S3	3*a*		0	0	0.53910(9)	1.00	0.0175(14)
S4	3*a*		0	0	0.13459(11)	1.00	0.0162(12)
$FeAl_2S_4$							
*M*1	1*b*	(Fe1 (50(2)%) + Al1 (50(2)%))	0	0	0.5	1.00	0.0280(13)
*M*2	2*d*	(Fe2 (25(2)%) + Al2 (75(2)%))	⅓	⅔	0.7933(3)	1.00	0.0250(12)
S1	2*d*		⅓	⅔	0.1336(3)	1.00	0.0275(12)
S2	2*d*		⅓	⅔	0.6058(3)	1.00	0.0266(12)
$CoAl_2S_4$							
*M*1	1*b*	(Co1 (40(2)%) + Al1 (60(2)%))	0	0	0.5	1.00	0.0072(4)
*M*2	2*d*	(Co2 (30(1)%) + Al2 (70(1)%))	⅓	⅔	0.20719(9)	1.00	0.0075(4)
S1	2*d*		⅓	⅔	0.86581(8)	1.00	0.0078(4)
S2	2*d*		⅓	⅔	0.39502(11)	1.00	0.0076(4)
$Ni_{0.68}Al_2S_{3.78}$							
Ni1	1*b*		0	0	0.5	0.66(3)	0.0136(15)
Al1	2*d*		⅓	⅔	0.2090(4)	1.00	0.0151(16)
S1	2*d*		⅓	⅔	0.8648(4)	1.00	0.0174(15)
S2	2*d*		⅓	⅔	0.3955(3)	0.89(3)	0.0104(14)

[a]Occupancy

[b]U_{eq} is defined as one third of the trace of the orthogonalized U_{ij} tensor.

$MnAl_2S_4$, and the atomic positions of $FeGa_2S_4$[13] were used as an initial structural model in determining the atomic positions of $FeAl_2S_4$, $CoAl_2S_4$, and $Ni_{0.68}Al_2S_{3.78}$.[27, 32] Refinement of the models of MAl_2S_4 (M = Mn, Fe, Co), prior to mixing between M^{2+} and Al^{3+} at both the

tetrahedral and octahedral sites, led to anomalous atomic displacement parameters at the octahedral and tetrahedral sites and high residuals of ρ_{max} ~ 14.0, ρ_{min} ~ -3.0 and R_1 = 13.5 % for $MnAl_2S_4$, ρ_{max} ~ 1.4, ρ_{min} ~ -0.7, and R_1 ~ 0.11 for $FeAl_2S_4$, and ρ_{max} ~ 3.7, ρ_{min} ~ -1.8, and R_1 ~ 0.16 for $CoAl_2S_4$. Mixing of M^{2+} (M^{2+} = Mn, Fe, Co) and Al^{3+} at both the octahedral and tetrahedral sites resulted in smooth difference maps and overall lower residuals. The refined compositions of MAl_2S_4 (M = Mn, Fe, Co) are consistent with those determined by SEM-EDX analysis. No missing symmetry was found using PLATON.[33]

Initial refinement of $Ni_{0.68}Al_2S_{3.78}$ using fully occupied atomic positions led to anomalous atomic displacement parameters for Ni1 and S2 and R_1 = 25.2 %. Partial occupancy of both Ni1 (66 %) and S2 (89 %) sites resulted in smooth difference maps and overall lower residuals with R1 = 6.16 %. The refined composition is consistent with that determined by EDXS analysis. No missing symmetry was found using PLATON.[33] A model with mixing of Ni^{2+} and Al^{3+} on both the octahedral and tetrahedral sites did not converge.

The models of $MnAl_2S_4$ and $CoAl_2S_4$ were both refined as twins. $MnAl_2S_4$ adopts a noncentrosymmetric space group (*R3m*) and is an inversion twin with a ~ 7.2 % contribution

Table 4.3 Bond Distances (Å) of MAl_2S_4 (M^{2+} = Mn^{2+}, Fe^{2+}, Co^{2+}) and $Ni_{0.68}Al_2S_{3.78}$

	$MnAl_2S_4$		$FeAl_2S_4$	$CoAlS_4$	$Ni_{0.68}Al_2S_{3.78}$
Octahedra					
$^{\dagger}M$3-S3 (x3)	2.492(3)	$^{\dagger}M$1-S2 (x6)	2.487(2)	2.4387(9)	2.430(2)
$^{\dagger}M$3-S4 (x3)	2.506(3)				
Tetrahedra					
$^{\dagger}M$1-S3 (x1)	2.302(7)	$^{\dagger}M$2-S1 (x3)	2.304(8)	2.2653(9)	2.264(2)
$^{\dagger}M$1-S1 (x3)	2.314(3)	$^{\dagger}M$2-S2 (x1)	2.286(5)	2.48(2)	2.230(6)
$^{\dagger}M$2-S4 (x1)	2.300(6)				
$^{\dagger}M$2-S2 (x3)	2.295(3)				
	$^{\dagger}M$ = Mn + Al		$^{\dagger}M$ = Fe + Al	$^{\dagger}M$ = Co + Al	

from the inverted component. The initial refinement of the model of $CoAl_2S_4$ using fully occupied atomic positions resulted in reasonable atomic displacement parameters and goodness of fit parameter, but the residual value (R_1) remained ~ 25 % with unusually large residual electron density peaks (ρ_{max} ~ 14 and ρ_{min} ~ -6) that could not be resolved as disorder. Since the observed intensities (F_{obs}^2) for the most disagreeable reflections were symmetrically much greater than the calculated intensities (F_{calc}^2), the possibility of twinning was explored. The model of $CoAl_2S_4$ was refined with the twin law for trigonal, merohedral twinning (-1 0 0 0 -1 0 0 0 1) with a 34.6% : 65.4% distribution from the two twin components and a R_1 ~ 0.05.

4.2.5 Property Measurements

Magnetization down to 2 K was measured under magnetic fields up to 9 T with a Quantum Design MPMS SQUID magnetometer to investigate the magnetic properties of MAl_2S_4(M^{2+} = Mn^{2+}, Fe^{2+}, Co^{2+}). Specific heat C_p was measured by the thermal relaxation method down to 0.4 K using a ^{3}He refrigerator. Table 4.4 summarizes the magnetic properties of $FeGa_2S_4$, $NiGa_2S_4$, $Ni_{0.68}Al_2S_{3.78}$[32] and structurally similar MAl_2S_4 (M^{2+} = Mn^{2+}, Fe^{2+}, Co^{2+}) with varying amounts of mixing between M^{2+} and Al^{3+}.

Table 4.4 Magnetic Properties of MAl_2S_4 (M^{2+} = Mn^{2+}, Fe^{2+}, Co^{2+}), $Ni_{0.68}Al_2S_{3.78}$, $FeGa_2S_4$, & $NiGa_2S_4$.

Phase		T^* (K)	θ_W (K)	$\lvert\theta_W\rvert/T^*$	ρ_{theo} (μ_B)	ρ_{eff} (μ_B)
$MnAl_2S_4$	(*ab*)	<< 1.8	-170	> 94.4	5.91 (S = 5/2)	5.97
$MnAl_2S_4$	(*c*)	2.5	-160	64.0	5.91	5.95
$FeAl_2S_4$	(*ab*)	10.5	-225	21.4	4.9 (S = 2)	5.28
$FeAl_2S_4$	(*c*)	10.5	-225	21.4	4.9	5.33
$CoAl_2S_4$	(*ab*)	5	-234	46.8	3.87 (S = 3/2)	4.4
$CoAl_2S_4$	(*c*)	5	-280	56.0	3.87	4.5
$Ni_{0.68}Al_2S_{3.78}$	(*ab*)	4	-55	13.7	2.83 (S = 1)	2.56
$Ni_{0.68}Al_2S_{3.78}$	(*c*)	4	-56	14.0	2.83	2.45
[4]$NiGa_2S_4$		8.5	-80	9.4	2.83 (S = 1)	2.82
[18]$FeGa_2S_4$		16	-160	10.0	4.9 (S = 2)	5.45

4.3 Results and Discussion

4.3.1 Structure of MAl_2S_4 (M^{2+} = Mn^{2+}, Fe^{2+}, Co^{2+}) and $Ni_{0.68}Al_2S_{3.78}$

The $MnAl_2S_4$ structure can be described as the hexagonal polymorph (~ 3 x 36 Å) of the $ZnIn_2S_4$ structure,[14] shown in Figure 4.2a, with blue spheres representing metal ions in an octahedral environment of S^{2-} ions (yellow spheres and green spheres representing metal ions in a tetrahedral environment of S^{2-} ions. The structures of MAl_2S_4 (M^{2+} = Fe^{2+}, Co^{2+}) and $Ni_{0.68}Al_2S_{3.78}$ can be described as the trigonal polymorph (~ 3 x 12 Å) of the $ZnIn_2S_4$ structure, also known as the $FeGa_2S_4$-structure[34] type, shown in Figure 4.2b with blue spheres representing metal ions in an octahedral environment (M_{oct}) of S^{2-} ions (yellow spheres) and green spheres representing metal ions in a tetrahedral environment (M_{tet}) of S^{2-} ions. The structure of MAl_2S_4 (M^{2+} = Mn^{2+}, Fe^{2+}, Co^{2+}) consists of alternating slabs of edge-sharing octahedra that share corners with corner-sharing tetrahedra with every other octahedral slab vacant, which leads to a van der Waals gap. The structure of $Ni_{0.68}Al_2S_{3.78}$ can be described as a defect-variant of the $FeGa_2S_4$ structure type with partially occupied Ni-centered octahedra with 66 % Ni^{2+} and 89 % S^{2-} occupancy. Therefore, MAl_2S_4 (M^{2+} = Mn^{2+}, Fe^{2+}, Co^{2+}) and $Ni_{0.68}Al_2S_{3.78}$ can be described

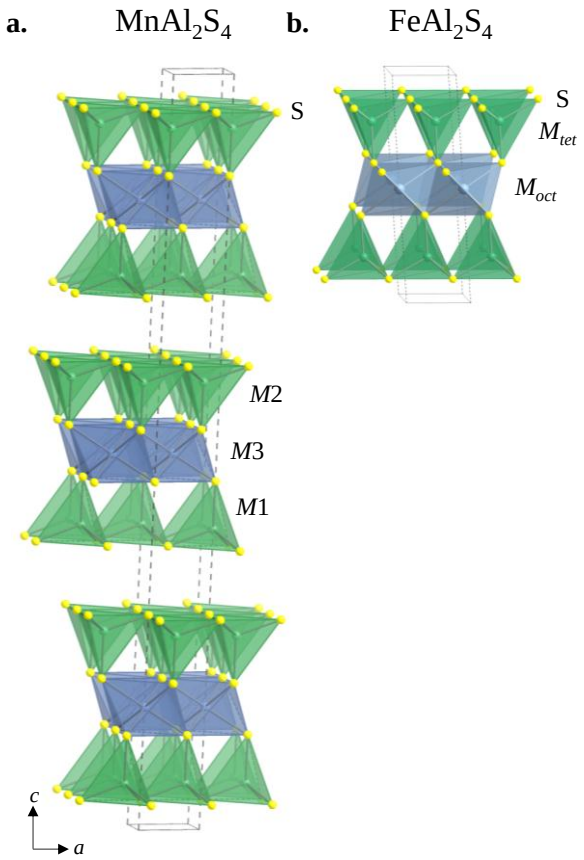

Figure 4.2 The crystal structures of **a.** $MnAl_2S_4$ with $M1$, $M2$, and $M3$ representing Mn^{2+} + Al^{3+} and **b.** $FeAl_2S_4$ with M = Fe^{2+} + Al^{3+} and yellow spheres representing S^{2-} ions.

as 2-*d* magnets with high two-dimensionality. The blue spheres (octahedral sites) and green spheres (tetrahedral sites) shown in Figure 4.2 form two planar (2-*d*), interpenetrating triangular lattices, which can result in frustrated antiferromagnetic coupling of magnetic moments due to site disorder and geometrical frustration.

4.3.2 Structure of $MnAl_2S_4$

Although the $ZnIn_2S_4$-type $MnAl_2S_4$ polymorph has been previously reported from X-ray powder diffraction measurements, here we report, for the first time, the full structure determination and magnetic properties of $ZnIn_2S_4$-type $MnAl_2S_4$.[35] The structure of $MnAl_2S_4$ exhibits mixing of Mn^{2+} and Al^{3+} on both the octahedral and tetrahedral sites. The octahedral sites are occupied by 56% Al^{3+} and 44% Mn^{2+} and surrounded by three equidistant (2.492(3) Å) S^{2-} atoms and three equidistant (2.506(3) Å) S^{2-} atoms. The octahedra are compressed along the *c*-direction with two in-plane angles of 84.46(3)˚ and 95.89(16)˚. There are two crystallographically unique tetrahedral sites, *M*1 and *M*2. The *M*1 tetrahedral site is occupied by 78% Al^{3+} and 22 % Mn^{2+}, and the *M*2 site is occupied by 68% Al^{3+} and 32% Mn^{2+}. Both tetrahedra are elongated along the *c*-direction and have apical *M*1/*M*2-S^{2-} (2.300(6) Å) bonds slightly longer than the remaining three *M*1/*M*2-S^{2-} (2.295(3) Å) bonds. The bond angles for the *M*1 tetrahedra are (S^{2-}-*M*1-S^{2-}) of 112.56(16)˚ and 106.21(18)˚, and the bond angles for the M2 tetrahedra (S^{2-}-*M*2-S^{2-}) 107.51(17)˚ and 11.37(16)˚. The observed bond distances of *M*-S^{2-} in the octahedra, where *M* = Mn^{2+} + Al^{3+}, are intermediate between high-spin, six-coordinate Mn^{2+}-S^{2-} (2.67 Å) and six-coordinate Al^{3+}-S^{2-} (2.38 Å).[36] The observed bond distances of *M*-S^{2-} in the tetrahedra, where *M* = Mn^{2+} + Al^{3+} of this phase are intermediate between high-spin, four-coordinate Mn^{2+}-S^{2-} (2.50 Å) and four-coordinate Al^{3+}-S^{2-} (2.23 Å).[36]

4.3.3 Structure of $FeAl_2S_4$

Replacing Ga^{3+} with Al^{3+} in $FeAl_2S_4$ results in mixing of Fe^{2+} and Al^{3+} on both the octahedral and tetrahedral sites. The octahedral sites M_{oct} (blue spheres in Figure 4.2b) are occupied by 50% Fe^{2+} and 50% Al^{3+} and surrounded by six equidistant (2.487(2) Å) S^{2-} atoms. These octahedra are compressed along the (111) direction, so there are two in-plane angles 95.54(10)˚ and 84.46(10)˚. The observed bond distances of M_{oct}-S^{2-}, where M = Fe^{2+} and Al^{3+} (2.487(2) Å), are intermediate between high-spin, six-coordinate Fe^{2+}-S^{2-} (2.62 Å) and six-coordinate Al^{3+}-S^{2-} (2.38 Å). The tetrahedral sites M_{tet} (green spheres in Figure 4.2b) are occupied by 25% Fe^{2+} and 75% Al^{3+} with the apical M_{tet}-S^{2-} bond (2.286(5) Å) slightly shorter than the remaining three M_{tet} -S^{2-} bonds (2.305(2) Å). These tetrahedra are compressed along the *c*-direction with angles of 106.00(10)˚ and 112.75(10)˚. The observed bond distances of M_{tet}-S^{2-}, where M = Fe^{2+} + Al^{3+} (2.286(5) Å to 2.304(8) Å), are intermediate between high-spin, four-coordinate Fe^{2+}-S^{2-} (2.46 Å) and four-coordinate Al^{3+}-S^{2-} (2.23 Å).[36]

Although isotypic $CoGa_2S_4$ and $MnGa_2S_4$ phases have not been reported, the structural effects of replacing Ga^{3+} with Al^{3+} can be investigated by comparing the isostructural $FeGa_2S_4$ and $FeAl_2S_4$. The mixing of Fe^{2+} with Al^{3+} in $FeAl_2S_4$ coincides with a larger unit cell than expected for substitution without mixing of Al^{3+} for Ga^{3+} in $FeGa_2S_4$ and results in distorted polyhedra. The bond angles of the octahedra (95.54(10)˚ and 84.46(10)˚) in $FeAl_2S_4$ indicate that the octahedra are slightly more compressed (~ 0.3% more distorted) along the (111) direction as compared with the equivalent bond angles in $FeGa_2S_4$ (95.16(10) ° and 84.83(10)˚).[13] The bond angles of the tetrahedra (112.75(10)˚ and 106.00(10)˚) in $FeAl_2S_4$ indicate that the tetrahedra are less distorted (~ 1.3 and ~1.5%, respectively) along the *c*-direction as compared to the equivalent bond angles in in $FeGa_2S_4$ (114.18(10)˚ and 104.36(10)˚).[13]

4.3.4 Structure of $CoAl_2S_4$

Replacing Ga^{3+} with Al^{3+} in $CoAl_2S_4$ results in mixing of Co^{2+} and Al^{3+} on both the octahedral and tetrahedral sites. The octahedral sites M_{oct} (blue spheres in Figure 4.2b) are occupied by 37% Co^{2+} and 63% Al^{3+} and surrounded by six equidistant (2.4388(9) Å) S^{2-} ions. These octahedra are compressed along the (111) direction, so there are two in-plane angles 95.83(4)˚ and 84.17(4)˚. The observed bond distance of M_{oct}-S^{2-}, where M = Co^{2+} and Al^{3+} (2.4388(9) Å), are intermediate between high-spin, six-coordinate Co^{2+}-S^{2-} (2.59 Å) and six-coordinate Al^{3+}-S^{2-} (2.38 Å).[36] The tetrahedral sites M_{tet} (green spheres in Figure 2b) are occupied by 29% Co^{2+} and 71% Al^{3+} with the apical M_{tet}-S^{2-} bond (2.248(2) Å) slightly shorter than the remaining three M_{tet}-S^{2-} bonds (2.654(9) Å). These tetrahedra are compressed along the *c*-direction. The observed bond distances of M_{tet}-S^{2-}, where M = Co^{2+} + Al^{3+}, are intermediate between high-spin, four-coordinate Co^{2+}-S^{2-} (2.42 Å) and four-coordinate Al^{3+}-S^{2-} (2.23 Å).[36]

4.3.5 Structure of $Ni_{0.68}Al_2S_{3.78}$

Replacement of Ga^{3+} for Al^{3+} in $Ni_{0.68}Al_2S_{3.78}$ results in occupational disorder. The Ni^{2+} octahedra (M_{oct} in Figure 4.2b) are surrounded by six equidistant (2.4301(6) Å) S^{2-} atoms and are compressed along the (111) direction so there are two in-plane angles 95.90˚ and 84.217˚. The Al^{3+} tetrahedra (M_{tet} in Figure 4.2b) are compressed along the *c*-direction with the apical Al^{3+}-S^{2-} bond (2.2339(4) Å) being slightly shorter than the remaining three Al^{3+}-S^{2-} bonds (2.2615(7) Å). The observed bond distances of Ni^{2+}-S^{2-} (2.4301(6) Å) in this phase are shorter than expected for fully occupied Ni^{2+}-S^{2-} ionic contacts (2.53 Å). The observed bond distances of Al^{3+}-S^{2-} (2.2615(7) Å and 2.2339(4) Å) are consistent with Al^{3+}-S^{2-} (2.23 Å) ionic radii, within experimental error. These bond distances are indicative of partial occupancy of Ni^{2+} (3*m*) and S^{2-} (2*d*) in this compound. A mixing model would require mixing of both Ni^{2+} and Al^{3+} at both

octahedral and tetrahedral sites and intermediate bond distances (2.38 Å) at both sites. Partial occupancy of Ni^{2+} and S^{2-} has been previously reported for various NiS-containing compounds, including NiS_{1-x},[37-39] Ni_xS_y,[40] $Ni_{2.5}MoS_{6.7}$,[41] $Ni_{0.45}ZrS_2$,[42] $Ni_{0.325}NbS_2$,[43] and $Ni_{0.95}Nb_3S_6$[44] phases. When comparing $NiGa_2S_4$ and $Ni_{0.68}Al_2S_{3.78}$ the partial occupancies of Ni^{2+} and S^{2-} coincide with a smaller unit cell than expected upon substitution of Al^{3+} for Ga^{3+} (without occupational disorder) in this phase. Previously reported NiB_2S_4 (B^{3+} = trivalent metal) polymorphs show Ni^{2+} mixing with other trivalent metals but not in the $FeGa_2S_4$-structure type.[45-48]

4.3.6 Physical Properties of $MnAl_2S_4$

Figure 4.3a shows the temperature dependence of the magnetic susceptibility of $MnAl_2S_4$ under 0.01 T and 5 T. Bifurcation at the spin freezing temperature, T^* = 2.5 K, between zero-field-cooled (ZFC) and field-cooled (FC) measurements at 0.01 T for B // c and is suppressed with increasing applied field. This spin-freezing behavior is characteristic for a spin glass system with site disorder by mixing of Mn^{2+} and Al^{3+} ions at both the octahedral and tetrahedral sites. While for B // ab, no hysteresis is observed down to 1.8 K, and T^* should be observed at T

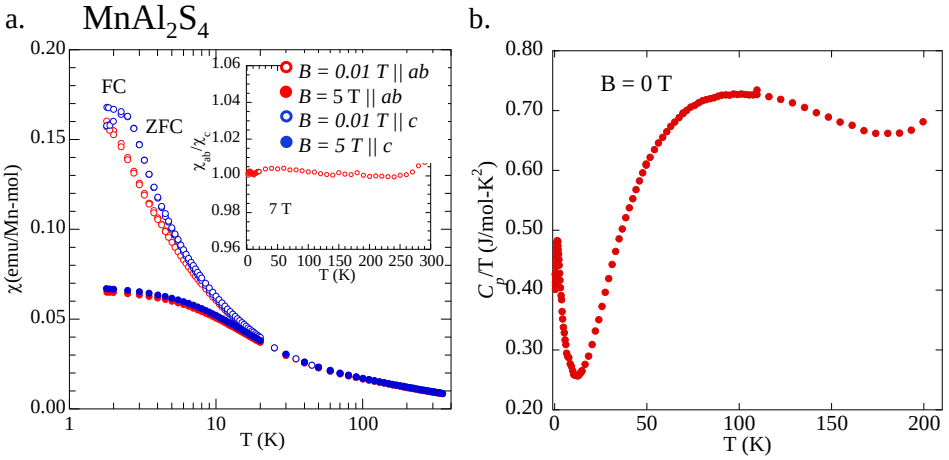

Figure 4.3 **a.** ZFC and FC temperature dependent magnetic susceptibility of $MnAl_2S_4$ at 0.01 and 5 T along both the *ab*-plane and the *c*-axis. (inset) χ_{ab}/χ_c as a function of T. **b.** The total specific heat C_p/T is shown as a function of T at 0 T. (inset) $(C_p\text{-}C_{nq})/T$ plotted as a function of T at applied fields of 0, 3, 7, and 9 T along the *c*-axis.

< 1.8 K. The hysteresis disappears with applied field. The magnetic susceptibility date were fit by the Curie-Weiss law, $\chi = C/(T - \theta_W)$, for $T > 150$ K for all analogues, and the estimated Weiss temperatures θ_W and effective moments p_{eff} are listed in Table 4. p_{eff} is estimated to be 5.95 μ_B for B // c and 5.97 μ_B for B // ab, which is consistent with the theoretical value $p_{theo} = 5.92$ μ_B for $S = {}^5/_2$. With high spin Mn^{2+} ions located at the octahedral ($(t_{2g})^3(e_g)^2$) and tetrahedral ($(e)^2(t_2)^3$) and tetrahedral sites, $MnAl_2S_4$ can be regarded as a $S = {}^5/_2$ Heisenberg antiferromagnet with no orbital order. The ratio of susceptibility of χ_c / χ_{ab} as a function of T under 5 T is ~ 1 down to 2 K as shown in the inset of Figure 3a, which indicates that this is an approximate 2-d Heisenberg system. The frustration parameter $|\theta_W| / T^* \sim 64$ for B // c is large which can be attributed primarily to strong site disorder and two-dimensionality with geometrical frustration of both the octahedral (blue spheres in Figure 4.2) and tetrahedral (green spheres in Figure 4.2) sublattices also playing a role.

Figure 4.3b shows the total specific heat C_p/T as a function of T in various fields. Unlike the structurally similar Ga-analogues, $MnGa_2S_4$, which order at low temperature (below 20 K), no magnetic long range order is observed down to 0.4 K in $MnAl_2S_4$. Due to the lack of a nonmagnetic analogue with the same crystal structure, the magnetic specific heat of MAl_2S_4 (M^{2+} = Mn, Fe, Co) have not been determined. Development of short range magnetic correlations is observed as a shallow broad maximum at T ~ 2 K. The absence of long range magnetic ordering is characteristic for spin glass systems. C_p/T exhibits a broad feature at $T = 80$ K, which may be attributed to the incoherent moment-free spin clusters. An upturn of C_p/T below 0.5 K is attributable to nuclear quadrupole specific heat C_{nq}. C_{nq} can be estimated to be $8.31 \times 10^{-4}/T^2$ (J/mol-K) at 0 T and was subtracted from C_p to show $(C_p - C_{nq})/T$ in the inset of Figure 3b.[16] (C_p-

C_{nq})/T is almost constant at 0 T, while (C_p-C_{nq})/T is suppressed at low temperatures under applied field along the c-axis.

4.3.7 Physical Properties of $FeAl_2S_4$

Figure 4.4a shows the temperature dependence of the magnetic susceptibility of $FeAl_2S_4$ at 0.01 T and 7 T. Bifurcation at the spin freezing temperature, T^* = 10.5 K, between ZFC and FC measurements for B // ab and c is observed, with site disorder by mixing of Fe^{2+} and Al^{3+} ions. The estimated effective moment p_{eff} and Weiss temperature θ_W by Cure-Weiss fitting above 150 K are shown in Table 4.4. The effective moment (p_{eff}) for $FeGa_2S_4$ is 5.45 μ_β and the anisotropic effective moments for $FeAl_2S_4$ are 5.28 μ_β in the ab-plane and 5.33 μ_B along the c-axis. The calculated effective magnetic moments are larger than the spin-only theoretical value p_{theo} = 4.90 μ_B, due to spin-orbital coupling of the Fe^{2+} ions. This is consistent with the fact that Fe^{2+} have S = 2 spins on both the octahedral ($(t_{2g})^4(e_g)^2$) and tetrahedral ($(e)^3(t_2)^3$) sites, thus $FeAl_2S_4$ can be regarded as an S = 2 system as well as $FeGa_2S_4$. χ_c/χ_{ab} is enhanced below ~90 K, which indicates $FeAl_2S_4$ has easy-axis anisotropy that can also be attributed to the spin-orbital

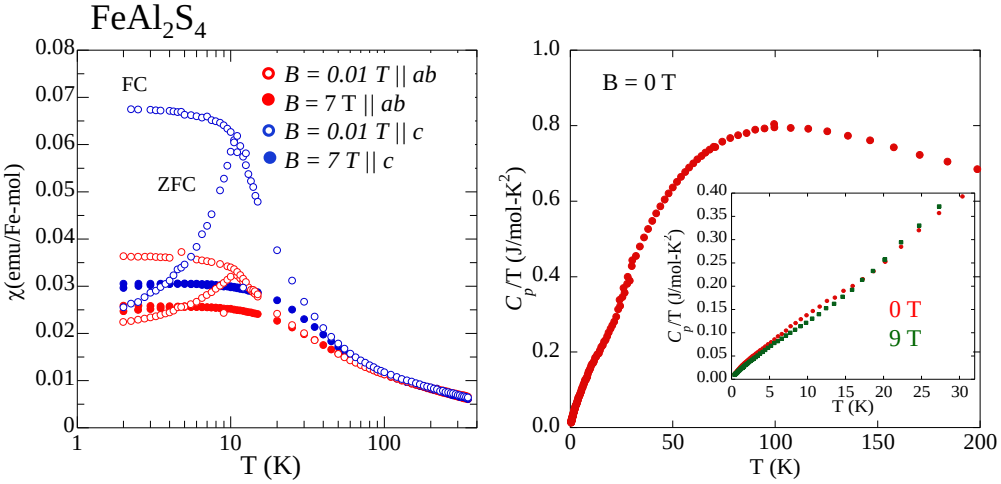

Figure 4.4 **a.** ZFC and FC temperature dependent magnetic susceptibility of $FeAl_2S_4$ at 0.01 and 7 T along both the ab-plane and c-axis. **b.** The total specific heat, C_p/T, as a function of T is plotted at 0 T. (inset) The low temperature data between 0.04 and 30 K at 0 and 9 T along the c-axis.

interaction. The frustration parameter $|\theta_W|$ / T^* ~ 21 for B // c is large which can be attributed primarily to strong site disorder and two-dimensionality with geometrical frustration of both the octahedral (blue spheres in Figure 4.2) and tetrahedral (green spheres in Figure 4.2) sublattices also playing a role. $FeAl_2S_4$ can be described as isostructural to $FeGa_2S_4$ but nominally more frustrated with a freezing temperature (T^*) of 10.5 K compared to 16 K for $FeGa_2S_4$ and a θ_W = -225 K compared to -160 K for $FeGa_2S_4$. The weak magnetic anisotropy in $FeAl_2S_4$ can be attributed to the distribution of Fe^{2+} atoms in both octahedral and tetrahedral sites of $FeAl_2S_4$ which is similar to the nearly isotropic behavior observed in the Ga-analogue, $FeGa_2S_4$.[23]

Figure 4.4b shows the total specific heat C_p/T as a function of T. No magnetic ordering is observed down to 0.4 K. There is a weak shoulder peak at around 10 K close to the freezing temperature T^* = 10.5 K, which is also found in other $M$$Ga_2S_4$ (M = Fe, Ni) compounds.[4, 18]

4.3.8 Physical Properties of $CoAl_2S_4$

Figure 4.5a shows the temperature dependent magnetic susceptibility at 0.01 T and 5 T. Hysteresis between ZFC and FC measurements is observed at T^* = 5 K, which is characteristic behavior in spin glass systems. We fit the data to Curie-Weiss law for T above 150 K and the estimated effective moment p_{eff} and Weiss temperature θ_W are listed in Table 4.4. An observed p_{eff} = 4.4 μ_B is larger than the theoretical spin-only value p_{theo} = 3.87 μ_B, and the larger moment of Co^{2+} can be attributed to spin-orbital coupling in a tetrahedral environment. This has been observed in $Co_{0.11}Zn_{0.89}O$, $CoAl_2O_4$, $Co_{0.20}Zn_{0.80}Al_2O_4$, $Co_{0.20}Mg_{0.80}Al_2O_4$, and $CoAl_{2-x}Ga_xO_4$.[25, 49] The temperature dependence of χ_c /χ_{ab} at 5 T is enhanced below ~50 K, which indicates easy-axis anisotropy similar to $FeAl_2S_4$, and is attributable to spin-orbital interaction. Although Co^{2+} ions are located on the octahedral ($(t_{2g})^5(e_g)^2$) and tetrahedral ($(e)^3(t_2)^4$), $CoAl_2S_4$ can be regarded as a S = $^3/_2$ system. The large frustration parameter $|\theta_W|$ /T^* ~ 46 for B // c can be attributed to the

combination of strong site disorder and two-dimensionality with geometrical frustration also playing a role.

Figure 4.5b shows the total specific heat C_p/T as a function of T at 0 T. Similar to γ-$CoGa_2S_4$, $CoAl_2S_4$ shows no magnetic phase transitions which correspond to the formation of long range order down to 0.4 K. C_p exhibits a broad peak at around 6.5 K, which are close to the freezing temperature T^* = 5 K found in other MAl_2S_4 compounds MGa_2S_4 (M^{2+} = Fe^{2+}, Ni^{2+}) compounds,[4, 18] which can be attributed to the development of short range magnetic ordering below 6.5 K. An upturn of C_p/T below 0.5 K is attributable to nuclear quadrupole specific heat C_{nq}. C_{nq} is estimated as $6.11 \times 10^{-4} / T^2$ (J/mole K) at 0 T. The inset of Figure 4.5b shows the temperature dependence of $(C_p\text{-}C_{nq})/T$. Consistent with the spin freezing behavior observed in susceptibility at 0.01 T, $(C_p\text{-}C_{nq})/T$ has a finite value at the lowest temperature limit.

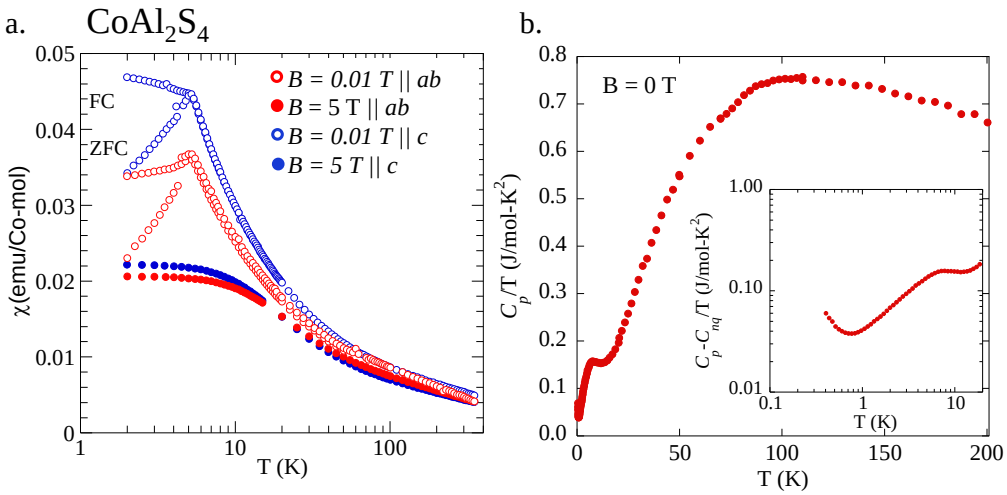

Figure 4.5 **a.** ZFC and FC temperature dependent magnetic susceptibility of $CoAl_2S_4$ at 0.01 and 5 T along both the *ab*-plane and the *c*-axis. **b.** The total specific heat, $(C_p\text{-}C_{nq})/T$, is plotted as a function of T at 0 T. (inset) The low temperature data (0.04 to 20 K) at 0 T.

4.3.9 Physical Properties of $Ni_{0.68}Al_2S_{3.78}$

Figure 4.6a shows the temperature dependence of susceptibility of $Ni_{0.68}Al_2S_{3.78}$ at 0.01 T and 7 T. There is a bifurcation at T^* = 4 K between ZFC and FC measurements at 0.01 T, which

is characteristic behavior in spin-glass systems with randomness of 30 % defects at Ni sites. The hysteresis disappears with increasing applied field. The data were fit to Curie-Weiss for $T > 200$ K and the estimated Weiss temperature θ_W and effective moment p_{eff} are listed in Table 4.4. p_{eff} is estimated to be 2.45 μ_B for $B // c$ and 2.56 μ_B for $B // ab$, which are smaller than the theoretical value $p_{theo} = 2.83$ μ_B for S = $^1/_2$. This smaller effective moment is consistent with the defects at the Ni sites as discussed above in the crystal structure analysis. χ_{ab}/χ_c is enhanced below 70 K, thus $Ni_{0.68}Al_2S_{3.78}$ has an easy-plane anisotropy.

Figure 4.6b shows the total specific heat C_p/T as a function of T at 0 T. No magnetic phase transitions which correspond to the formation of long-range order are observed down to 0.4 K. The inset of Figure 4.6b shows the temperature dependence of $(C_p\text{-}C_{nq})/T$. The magnetic heat capacity exhibits a broad feature at $T \sim 90$ K attributed to the incoherent moment-free spin clusters and a low temperature feature at $T \sim 10$ K due to short-range correlations. Despite the absence of long-range order in $Ni_{0.68}Al_2S_{3.78}$, C_p exhibits characteristic behavior of 2-*d* antiferromagnet.

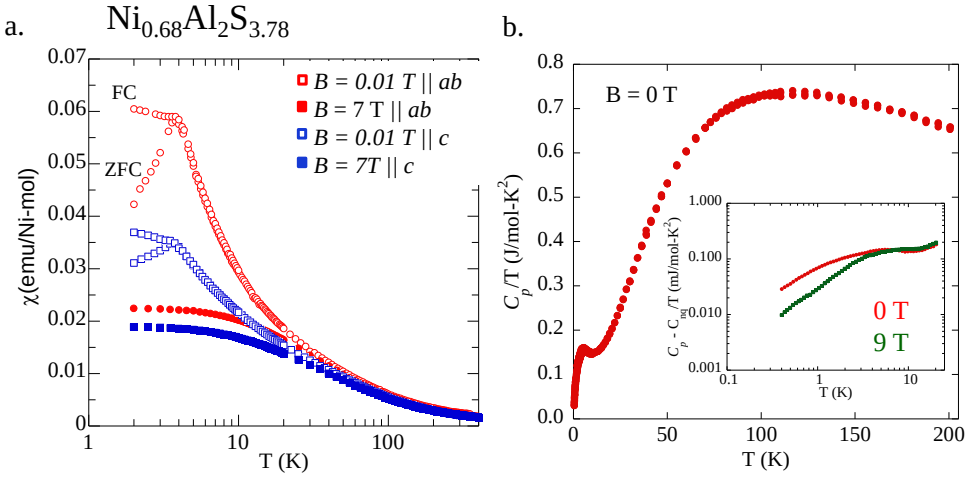

Figure 4.6 **a.** ZFC and FC temperature dependent magnetic susceptibility of $Ni_{0.68}Al_2S_{3.78}$ at 0.01 and 5 T along both the *ab*-plane and the *c*-axis. **b.** The total specific heat, C_p/T, as a function of T is plotted at 0 T. (inset) The low temperature data between 0.04 and 30 K at 0 and 9 T along the *c*-axis.

4.3.10 Comparison of $M^{2+}Al_2S_4$ (M^{2+} = Mn^{2+}, Fe^{2+}, Co^{2+}), $Ni_{0.68}Al_2S_{3.78}$, $FeGa_2S_4$, and $NiGa_2S_4$.

The $M^{2+}Al_2S_4$ (M^{2+} = Mn, Fe, Co) and $Ni_{0.68}Al_2S_{3.78}$ phases are structurally very similar to the $M^{2+}Ga_2S_4$ (M^{2+} = Mn^{2+}, Fe^{2+}, Co^{2+}, Ni^{2+}) phases as all phases are built of the same structural moieties, edge-sharing octahedra which share corners with corner-sharing tetrahedra. The magnetic frustration exhibited by $M^{2+}Al_2S_4$ and $Ni_{0.68}Al_2S_{3.78}$ can be attributed to a combination of the geometrical frustration due to the antiferromagnetic correlations of (M^{2+} = M^{2+} = Mn^{2+}, Fe^{2+}, Co^{2+}) and Ni^{2+} moments on a triangular sublattice and the 2-dimensional magnetic lattice due to the vacancy of every other octahedral slab. The magnetic behavior of $M^{2+}Al_2S_4$ and $Ni_{0.68}Al_2S_{3.78}$ is significantly more complicated than $M^{2+}Ga_2S_4$ (M^{2+} = Mn^{2+}, Fe^{2+}, Co^{2+}, Ni^{2+}) due to the magnetic dilution by mixing of M^{2+} and Al^{3+} in two triangular sublattices, the octahedral and tetrahedral sublattices, of $M^{2+}Al_2S_4$ (M^{2+} = Mn^{2+}, Fe^{2+}, Co^{2+}) and due to the partial occupancy of Ni^{2+} in $Ni_{0.68}Al_2S_{3.78}$ in the triangular octahedral sublattice. The mixing of M^{2+} and Al^{3+} in the $M^{2+}Al_2S_4$ ((M^{2+} = Mn^{2+}, Fe^{2+}, Co^{2+}) results in weak magnetic anisotropy which increases the effective dimensionality of the $M^{2+}Al_2S_4$ and also serves to heighten the effects of site disorder as compared to geometrical frustration and low dimensionality. The magnetic behavior of the structurally ordered $M^{2+}Ga_2S_4$ (M^{2+} = Fe, Ni) phases can be used to roughly estimate the effects of disorder on magnetic correlations in $M^{2+}Al_2S_4$ (M^{2+} = Mn, Fe, Co), thereby isolating the geometrical frustration and dimensionality parameters from the site disorder parameter in these structurally related phases. Here we see that magnetic frustration increases with the addition of site disorder in $M^{2+}Al_2S_4$ (M^{2+} = Fe^{2+}, Ni^{2+}) due either to mixing of Fe^{2+} and Al^{3+} in $FeAl_2S_4$ or to the partial occupancy of Ni^{2+} and S^{2-} in $Ni_{0.68}Al_2S_{3.78}$[32] by roughly ~ 55% and ~31%, respectively, as compared to the structurally ordered $M^{2+}Ga_2S_4$ (M^{2+} = Fe^{2+}, Ni^{2+}) phases. The frustration across the series $M^{2+}Al_2S_4$ (M^{2+} = Mn^{2+}, Fe^{2+}, Co^{2+}), as indicated the frustration

parameter, $|\theta_W|/T^*$, also increases with increasing structural distortion as evidenced by the increase in distortion in both the tetrahedral and octahedral environments with decreasing ionic M^{2+} radius. The additional magnetic frustration in MAl$_2$S$_4$ as compared to MGa$_2$S$_4$ can be attributed to the inhomogeneous environment surrounding the magnetic moments similar to the spin glass behavior in CoAl$_{2-x}$Ga$_x$O$_4$.[25]

4.4 Conclusions

No magnetic long range order was observed down to 0.4 K for MAl$_2$S$_4$ (M^{2+} = Mn^{2+}, Fe^{2+}, Co^{2+}). Instead, we observed bifurcation between ZFC and FC measurements below the spin freezing temperature, T^*, in magnetic susceptibility of MAl$_2$S$_4$ (M^{2+} = Mn^{2+}, Fe^{2+}, Co^{2+}) and Ni$_{0.68}$Al$_2$S$_{3.78}$ characteristic of spin glass systems. The spin glass behavior seen at 0.1 T is suppressed with increasing applied field and completely disappears at 5 T or 7 T. A broad peak in C_P below T^* is attributable to the development of short range order.

MnAl$_2$S$_4$ (S = $^5/_2$), CoAl$_2$S$_4$ (S = $^3/_2$), FeAl$_2$S$_4$ (S = 2), and Ni$_{0.68}$Al$_2$S$_{3.78}$ (S = 1) show spin glass behavior below T^* in ZFC and FC susceptibility measurements at 0 T. In particular, the frustration parameters $|\theta_W|/T^*$ are large for MnAl$_2$S$_4$, CoAl$_2$S$_4$, FeAl$_2$S$_4$, and Ni$_{0.68}$Al$_2$S$_{3.78}$. Theoretically, the 2-*d* Heisenberg spin glass system is not expected to show any spin freezing at finite temperature. The nearly Heisenberg (isotropic) nature of Mn^{2+} (S = $^5/_2$) spins, strong site disorder, and two-dimensionality should be the origin of the strong suppression of the spin glass freezing.

For FeAl$_2$S$_4$ (S = 2), C_P exhibits T^2-dependence with almost no difference in low-temperature C_P between 0 T and 9 T. This is different from the typical T-linear dependence seen in the Mn- and Co- analogues and is consistent with the fact suggested by the impurity effects on NiGa$_2$S$_4$, that the integer size of the Heisenberg spins is important to stabilize the 2-*d* spin wave-

like coherent behavior.[16] Future studies involve microscopic magnetic structure determination by neutron diffraction studies.

A possible explanation for the previously unreported Fe^{2+}-, Co^{2+}-, and Ni^{2+}- analogues is these compounds lie on the edge of structural stability of the $M^{2+}Al_2S_4$ (M^{2+} = divalent metal) phase. One obvious reason being the decrease in size from Mn^{2+} to Ni^{2+}. When comparing the tetrahedral angles and octahedral angles as a function of ionic radii, the distortion in both the tetrahedral and octahedral environments decrease as the ionic radii increase. The decrease in size of M^{2+} (M^{2+} = Mn^{2+}, Fe^{2+}, Co^{2+}, and Ni^{2+}) across the series, coincides with change in disorder type from mixing of M^{2+}/Al^{3+} at the octahedral and tetrahedral sites in $M^{2+}Al_2S_4$ (M^{2+} = Mn^{2+}, Fe^{2+}, Co^{2+}) to partial occupancy of Ni^{2+} and S^{2-} in $Ni_{0.68}Al_2S_{3.78}$.[32] This is also consistent with the increasing frustration parameter with decreasing ionic M^{2+} radius.

To rationalize the structural differences between $M^{2+}Al_2S_4$ (M^{2+} = Mn^{2+}, Fe^{2+}, Co^{2+}, and Ni^{2+}) we have consulted structure field maps. The structure field maps compiled using mean values of pseudopotential radii by Haeuseler have been used to successfully predict new compounds of the various $ZnIn_2S_4$-polytypes and to also explain the absence of others.[50] We have included several compounds adopting the $FeGa_2S_4$-type structure the map compiled by Haeuseler in Figure 4.7. The separation between the $ZnIn_2S_4$-type and thiogallate-type structures, as well as the separation between the $ZnIn_2S_4$-type and $FeGa_2S_4$-type structures, is good, but the separation between the thiogallate-type and the $FeGa_2S_4$-type structures is not well resolved. The $FeGa_2S_4$-type $M^{2+}Al_2S_4$ (M^{2+} = Fe^{2+}, Co^{2+}, Ni^{2+}) and $MnAl_2S_4$ ($ZnIn_2S_4$-type) compounds are close to the border separating the $FeGa_2S_4$-type and $ZnIn_2S_4$-type structures. Similar observations have been used to rationalize the lack of compounds of MGa_2S_4-MCr_2S_4 (M = Zn, Cd, Hg) with the $ZnIn_2S_4$-type structure,[50] can explain the previous failed attempts to grow

these compounds,[15] and is consistent with increasing structural instability on moving from Mn^{2+} to Ni^{2+} across the series.

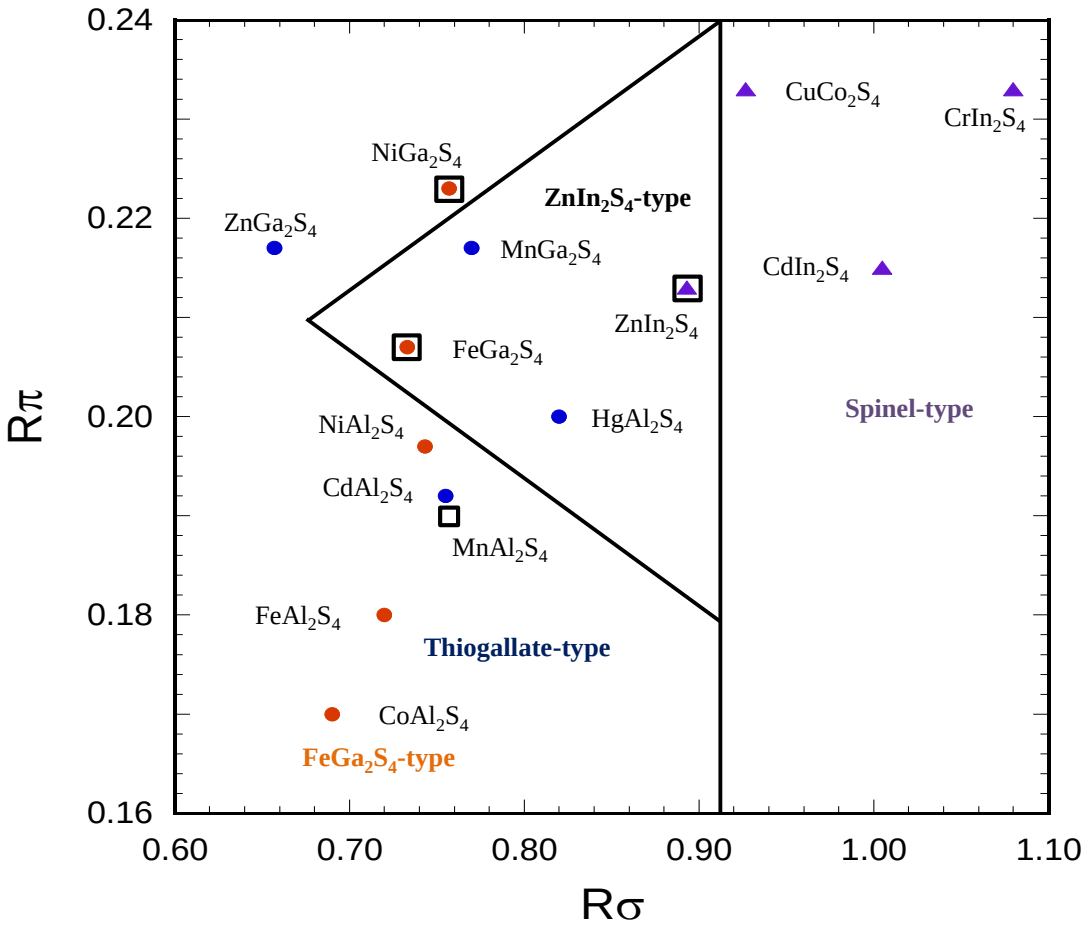

Figure 4.7 A segment of the structure field map for AB_2S_4 (*A* = transition metal; *B* = transition metal or main group metal) compounds compiled by Haeuseler is shown with the $FeGa_2S_4$-type, $ZnIn_2S_4$-type, thiogallate-type, and spinel-type structures. The lines indicate the calculated border between structure types as determined by Haeuseler.

4.5 References

(1) Moessner, R.; Ramirez, A. P., Geometrical frustration. *Phys. Today* **2006,** *2006*, 24-29.

(2) Greedan, J. E., Frustrated rare earth magnetism: spin glasses, spin liquids and spin ices in pyrochlore oxides. *J. Alloys Compd.* **2006,** *408-412*, 444-455.

(3) Levi, B. G., New candidate emerges for a quantum spin liquid. *Phys. Today* **2007,** *2007*, 16-19.

(4) Nakatsuji, S.; Nambu, Y.; Tonomura, H.; Sakai, O.; Jonas, S.; Broholm, C.; Tsunetsugu, H.; Qiu, Y.; Maeno, Y., Spin disorder on a triangular lattice. *Science* **2005,** *309*, 1697-1700.

(5) Affleck, J., *J. Phys. Condens. Matter* **1989,** *1*, 3047.

(6) Collins, M. F.; Petrenko, O. A., *Can. J. Phys.* **1997,** *75*, 605-655.

(7) Nakatsuji, S.; Nambu, Y.; Onoda, S., Novel geometrical frustration effects in the two-dimensional triangular-lattice antiferromagnet $NiGa_2S_4$ and related compounds. *J. Phys. Soc. Jpn.* **2010,** *79*, 011003.

(8) Radaelli, P. G.; Horibe, Y.; Gutmann, M. J.; Ishibashi, H.; Chen, C. H.; Ibberson, R. M.; Koyama, Y.; Hor, Y.-S.; Kiryukhin, V.; Cheong, S.-W., Formation of isomorphic Ir^{3+} and Ir^{4+} octamers and spin dimerization in the spinel $CuIr_2S_4$. *Nature* **2002,** *416*, 155-158.

(9) Schmidt, M.; Ratcliff, W.; Radaelli, P. G.; Refson, K.; Harrison, N. M.; Cheong, S. W., Spin singlet formation in $MgTi_2O_4$: evidence of a helical dimerization pattern. *Phys. Rev. Lett.* **2004,** *92*, 056402.

(10) Fritsch, V., Spin and orbital frustration in $MnSc_2S_4$ and $FeSc_2S_4$. *Phys. Rev. Lett.* **2004,** *92*, 116401.

(11) Hemberger, J.; Lunkenheimer, P.; Fichtl, R.; Krug von Nidda, H. A.; Tsurkan, V.; Loidl, A., Relaxor ferroelectricity and colossal magnetocapacitive coupling in ferromagnetic $CdCr_2S_4$. *Nature* **2005,** *434* (7031), 364-367.

(12) Weber, S.; Lunkenheimer, P.; Fichtl, R.; Hemberger, J.; Tsurkan, V.; Loidl, A., Colossal magnetocapacitance and colossal magnetoresistance in $HgCr_2S_4$. *Phys. Rev. Lett.* **2006,** *96*, 157202.

(13) Dogguy Smiri, L.; Dung, N. H.; Pardo, M. P., Crystal structure of the alpha polytype of $FeGa_2S_4$. *Mater. Res. Bull.* **1980,** *15*, 861-866.

(14) Lappe, F.; Niggli, A.; Nitsche, R.; White, J. G., The crystal structure of In_2ZnS_4. *Z. Kristallogr.* **1962,** *117*, 146-152.

(15) Chaus, I. S.; Sheka, I. A., Reactivity of sulphides. *Russ. Chem. Rev.* **1969,** *38*, 375-388.

(16) Nambu, Y.; Nakatsuji, S.; Maeno, Y.; Okudzeto, E.; Chan, J. Y., Spin dependent impurity effects on the 2D frustrated magnetism of $NiGa_2S_4$. *Phys. Rev. Lett.* **2008,** *101*, 207204.

(17) Myoung, B. R.; Kim, S. J.; Kim, C. S., Crystallographic and magnetic properties of $FeGa_2S_4$. *J. Korean Phys. Soc.* **2008,** *53*, 750-753.

(18) Nakatsuji, S.; Tonomura, H.; Onuma, K.; Nambu, Y.; Sakai, O.; Maeno, Y.; Macaluso, R. T.; Chan, J. Y., Spin disorder and order in quasi-2d triangular heisenberg antiferromagnets: comparative study of $FeGa_2S_4$, $Fe_2Ga_2S_5$, and $NiGa_2S_4$. *Phys. Rev. Lett.* **2007,** *99*, 157203.

(19) Tomita, T.; Nambu, Y.; Nakatsuji, S.; Koeda, S.; Hedo, M.; Uwatoko, Y., Pressure dependence of electrical transport in the triangular antiferromagnetic insulators $FeGa_2S_4$ and $Fe_2Ga_2S_5$. *J. Phys. Soc. Jpn.* **2009,** *78*, 094603.

(20) Takubo, K.; Mizokawa, T.; Nambu, Y.; Nakatsuji, S., Electronic structure study of triangular lattices in $FeGa_2S_4$, $Fe_2Ga_2S_5$, and $NiGa_2S_4$: photoemission spectroscopy and Hartree-Fock calculations. *Phys. Rev. B* **2009,** *79*, 134422.

(21) Rimet, R.; Buder, R.; Schlenker, C., New antiferromagnetic properties of manganese gallium sulfides alpha-$MnGa_2S_4$ and beta-$MnGa_2S_4$. *Solid State Commun.* **1981,** *37*, 693-697.

(22) Pardo, M. P., Etude des systemes Ga_2S_3-CoS et Ga_2Se_3-CoSe. *Mater. Res. Bull.* **1982,** *17*, 1477-1481.

(23) Agnostinelli, E.; Gastaldi, L.; Viticoli, S., Crystallographic and magnetic investigations on cobalt gallium sulfides: alpha-$CoGa_2S_4$ and beta-$CoGa_2S_4$. *J. Phys. Chem. Solids* **1985,** *46*, 1345-1349.

(24) Tsuboi, N.; Ogihara, K.; Suda, Y.; Oishi, K.; Kobayashi, S.; Kaneko, F., Crystal structure and optical properties of defect-chalcopyrite-type $MnGa_2S_4$. *Jpn. Soc. Appl. Phys.* **2005,** *44*, 725-728.

(25) Melot, B. C.; Page, K.; Seshadri, R.; Stoudenmire, E. M.; Balents, L.; Bergman, D. L.; Proffen, T., Magnetic frustration on the diamond lattice of the *A*-site magnetic spinels $CoAl_{2-x}Ga_xO_4$: the role of lattice expansion and site disorder. *Phys. Rev. B* **2009,** *80*, 104420.

(26) Le, M. L. P.; Strobel, P.; Colin, C. V.; Pagnier, T.; Alloin, F., Spinel-type solid solutions involving Mn^{4+} and Ti^{4+}:crystal chemistry, magnetic and electrochemical properties. *J. Phys. Chem. Solids* **2011,** *72*, 124-135.

(27) Menard, M. C.; Ishii, R.; Higo, T.; Nakatsuji, S.; Nishibori, E.; Sawa, H.; Chan, J. Y., High-resolution synchrotron studies and magnetic properties of frustrated antiferromagnets MAl_2S_4 (M^{2+} = Mn^{2+}, Fe^{2+}, Co^{2+}). *Chem. Mater.* **2011,** *23*, 3086-3094.

(28) Bruker *SAINT Version 7.6A Software Reference Manual*, Bruker AXS Inc.: Madison, Wisconsin, USA, 2007.

(29) Sheldrick, G. M. *SADABS v2008/1 semi-empirical absorption and beam correction program*, University of Göttingen, Germany, 2008.

(30) Altomare, A.; Burla, M. C.; Camalli, M.; Cascarano, G.; Giacovazzo, C.; Guagliardi, A.; Polidori, G., SIR92 - a program for automatic solution of crystal structures by direct methods. *J. Appl. Crystallogr.* **1994,** *27*, 435.

(31) Sheldrick, G. M., A short history of SHELX. *Acta Crystallogr. Sect. A.: Found Crystallogr.* **2008,** *A64*, 112-122.

(32) Higo, T.; Ishii, R.; Menard, M. C.; Chan, J. Y.; Yamaguchi, H.; Hagiwara, M.; Nakatsuji, S., Magnetic properties of the quasi-two-dimensional antiferromagnet $Ni_{0.7}Al_2S_{3.7}$. *Phys. Rev. B* **2011,** *In Press.*

(33) Spek, A. L., PLATON, a multipurpose crystallographic tool. *J. Appl. Crystallogr.* **2003,** *36*, 7-13.

(34) Smiri, D.; Dung, N. H.; Pardo, M. P., Structure cristalline du polytype alph-$FeGa_2S_4$ *Mater. Res. Bull.* **1980,** *15*, 861-866.

(35) Flahaut, J., Etude De Quelques Thioaluminates *C. R. Hebd. Acad. Sci.* **1951,** *233*, 1279.

(36) Shannon, R. D.; Prewitt, C. T., Synthesis and structure of phases in the In_2O_3 - Ga_2O_3 system. *J. Inorg. Nuc. Chem.* **1968,** *30*, 1389-1398.

(37) Nowack, E.; Schwarzenbach, D.; Hahn, T., Charge densities in CoS_2 and NiS_2 (pyrite structure). *Acta Cryst.B.* **1991,** *47*, 650-659.

(38) Nowack, E.; Schwarzenbach, D.; Gonschorek, W.; Hahn, T., Deformationsdichten in CoS_2 und NiS_2 mit Pyritstruktur. *Z. Kristallogr.* **1989,** *186*, 213-215.

(39) Kuznetsov, V. G.; Eliseev, A. A., X-ray diffraction determination of the homogeneity boundaries and nature of the beta-NiS phase. *Zh. Strukt. Khim.* **1981,** *2*, 578-584.

(40) Fleet, M. E., The crystal structure of alpha-Ni_7S_6. *Acta Cryst.B.* **1972,** *28*, 1237-1241.

(41) Chang, C. L.; Tao, Y. K.; Swinnea, J. S.; Steinfink, H., Oxygen substitution in Sn and Ni Chevrel phases. *Acta Cryst. C.* **1987,** *43*, 1461-1465.

(42) Trichet, L.; Cousseau, J.; Rouxel, J., The Fe-ZrS_2 and Co-ZrS_2 systems. structure of M_xZrS_2. *C.R. Acad. Sci. C Chim.* **1972,** *274*, 394-397.

(43) van Laar, B.; Rietveld, H. M.; Ijdo, D. J. W., Magnetic and crystallographic structure of Me_xNbS_2 and Me_xTaS_2. *J. Solid State Chem.* **1971,** *3*, 154-160.

(44) Anzenhofer, K.; van den Berg, J. M.; Cossee, P.; Helle, J. N., The crystal structures and magnetic susceptibilities of $MnNb_3S_6$, $FeNb_3S_6$, $CoNb_3S_6$, and $NiNb_3S_6$. *J. Phys. Chem. Solids* **1970,** *31*, 1057-1067.

(45) Lutz, H. D.; Jung, M., Kationenverteilung und Überstrukturordnung in ternären und quaternären Sulfidspinellen $M^{2+}M_3^{+2}S_4$ – Einkristallstrukturuntersuchungen. *Z. Anorg. Allg. Chem* **1989,** *579*, 57-65.

(46) Colgan, D. C.; Powell, A. V., A time-of-flight powder neutron diffraction study of ternary chromium sulfides, $Ni_xCr_{3-x}S_4$. *J. Mater. Chem.* **1997,** *7*, 2433-2439.

(47) Kesler, Y. A.; Smirnov, S. G.; Poklohok, K. V.; Viting, B. N., The crystal chemistry of iron-nickel spinels. *Izv. Acad. SSSR. Neorgan. Mater.* **1991,** *311*, 909-913.

(48) Harada, S., Some new sulfo-spinels containing iron-group transition metals. *Mater. Res. Bull.* **1973,** *8*, 1361-1370.

(49) Cossee, P.; Van Arkel, A. E., Magnetic properties of Co^{2+} ions in tetrahedral interstices of an oxide lattice. *J. Phys. Chem. Solids* **1960,** *15*, 1-6.

(50) Haeuseler, H., Structure field maps for sulfides of composition AB_2X_4. *J. Solid State Chem.* **1990,** *86* (2), 275-278.

CHAPTER 5. STRUCTURE AND MAGNETISM OF THE QUASI-1-*D* $K_4Cu(MoO_4)_3$ AND THE STRUCTURE OF $K_4Zn(MoO_4)_3$*

5.1 Introduction

The low dimensionality and quantum fluctuations found in quantum magnets with S = $^1/_2$ and S = 1 present a unique opportunity to discover new states of matter, including quantum spin liquids[1-2] and 2D frustrated antiferromagnets.[3] Quantum magnets can be generally classified as materials with strong magnetic correlations that fail to show long-range order down to T = 0 K due to quantum fluctuations. The search for model systems to compare experimental results with theoretical predictions has been an exciting quest, and we have focused on the crystal growth and characterization of quantum magnets. This is motivated by the spin-$^1/_2$ quantum magnets which present the simplest models for the study of low dimensional materials with enhanced quantum fluctuations. Specifically many Cu^{2+} (S = $^1/_2$) systems have been found to display quantum behavior such as the quasi-2-*d* quantum antiferromagnet La_2CuO_4,[1] the quantum spin system $SrCu_2(BO_3)_2$,[4] the multiferroic $CuFeO_2$,[5] the spin ladders, $Sr_{m-1}Cu_{m+1}O_{2m}$ which exhibit a 1-*d* chain spin liquid ground state,[6] and the spin-½ kagome antiferromagnet $Cu_3Zn(OH)_6Cl_2$.[7]

Many Mo-oxides adopt low dimensional structures.[8-20] In these phases, there are distortions in the MoO_4 tetrahedra which can be explained by electronic considerations. *M*-Mo-oxide (M^{m+} = transition metal or group 13-14 metal with $m < 6$) compounds containing MoO_4 tetrahedra typically exhibit corner sharing between MoO_4 tetrahedra and *M*-O metal-centered environments.[11, 14-23] In these compounds, Mo-O-*M* interactions are more favorable than Mo-O-Mo interactions due to the very electron-deficient nature of Mo^{6+} (d^0). Therefore increased interactions along one direction (Mo-O-*M*) are enhanced at the expense of the interactions between Mo-O-Mo, along the orthogonal direction. There is also the possibility of second-order

*This work has been submitted to *Inorganic Chemistry:* Menard, M. C.; Ishii, R.; Onuma, K.; Nakatsuji, S.; Chan, J. Y., Structure and magnetism of the quasi-1-*d* $K_4Cu(MoO_4)_3$ and the structure of $K_4Zn(MoO_4)_3$. *Inorg. Chem.* **2011,** *Submitted*.

Jahn-Teller distortions in the Mo^{6+} environment which would also account for the decreased dimensionality. $RbFe(MoO_4)_2$ and $Rb_4Mn(MoO_4)_3$ are two reported structurally related examples of 2-*d* antiferromagnets with spin-$^5/_2$ due to high-spin Fe^{3+} and Mn^{2+}, respectively.[24-25] We have focused on low dimensional compounds with Mo^{6+} and Cu^{2+} which may lead to low dimensional materials with quantum fluctuations. Spin-$^1/_2$ Cu^{2+} allows for the study of interacting, individual spins without spin-orbital coupling, and Mo^{6+} can provide either a nonmagnetic block to isolate each magnetic moment or an anisotropic pathway for the coupling of magnetic ions through superexchange along a preferred direction.

The structure of the K-analogue, $K_4Cu(MoO_4)_3$ has been previously reported from X-ray powder data with two, reversible structural transitions.[26] The high temperature (~ 900 K) phase was reported as a metastable phase with a hexagonal unit cell, and the most stable of the three polymorphs, the mid-range temperature phase (~ 700 K), was reported with an orthorhombic unit cell.[26] The low temperature phase (~ 600 K), although reported as a monoclinic cell, is marked by peak splitting possibly due to twinning and a drastic decrease in crystal quality.[26] All previous reports of the $A_4Cu(MoO_4)_3$ (*A* = K, Rb, Cs) family indicate that the low temperature phase is likely a supercell of the stable, high temperature hexagonal polymorph and the orthorhombic phase is a structural variant of the hexagonal polymorph, termed pseudo-hexagonal.[26] Full structural and property characterization of these phases was not accomplished due to past difficulties in growing high-quality single crystals and in handling hygroscopic crystals. Recently we discovered $Rb_4Cu(MoO_4)_3$, a quasi-1-*d* quantum antiferromagnet with quantum fluctuations.[11] When comparing quasi-1-*d* quantum antiferromagnets, $A_4Cu(MoO_4)_3$ (*A* = K, Rb), the structural differences that affect the strength of magnetic correlations between Cu^{2+} ions can be investigated to isolate the dimensionality and structural disorder parameters. Here

we report the growth and characterization of single crystals of the orthorhombic phase of $K_4Cu(MoO_4)_3$, a new quasi-1-*d* quantum antiferromagnet, and the structure of the nonmagnetic reference, $K_4Zn(MoO_4)_3$. We also compare the isostructural $A_4Cu(MoO_4)_3$ (*A* = K, Rb) compounds to examine the structural differences that affect the strength of magnetic correlations between Cu^{2+} ions.

5.2 Experimental

5.2.1 Synthesis of $K_4M(MoO_4)_3$ (*M* = Cu, Zn)

Polycrystalline samples of $K_4M(MoO_4)_3$ (*M* = Cu, Zn) were synthesized via the ceramic reaction method according to the chemical reaction,

$$2K_2CO_3 + MO + 3MoO_3 \rightarrow K_4M(MoO_4)_3 + 2CO_2 \uparrow \ (M = Cu, Zn).$$

Due to the hygroscopic nature of K_2CO_3, the reactants were dehydrated by heating at 300 °C for over 3 h before grinding. The mixture was pressed into a pellet and calcined at 480 °C for 40 h. The procedure was repeated 3 times to obtain a homogeneous phase. Single crystals were grown using $K_2Mo_2O_7$ as the flux and polycrystalline $K_4M(MoO_4)_3$ (*M* = Cu, Zn) as the charge with a charge-flux molar ratio of 1:1. Melt solutions were kept under oxygen atmosphere in a fused silica tube at 590-600 °C for 40 h, followed by cooling to 500 °C at 1 °C/h. Bluish-green, transparent, hexagonal $K_4Cu(MoO_4)_3$ crystals and colorless, transparent, thin $K_4Zn(MoO_4)_3$ crystals were obtained for M = Cu and Zn, respectively. X-ray powder diffraction was performed to ensure phase purity with a Rigaku RINT 2100 diffractometer (Cu Kα λ = 1.54056 Å).

5.2.2 Structure Determination of $K_4M(MoO_4)_3$ (*M* = Cu, Zn)

Crystals of approximately 0.03 x 0.03 x 0.03 mm^3 and 0.05 x 0.11 x 0.12 mm^3 of $K_4M(MoO_4)_3$ (*M* = Cu, Zn) sizes, respectively, were mounted with epoxy onto a glass fiber,

coated with Paratone-N oil to protect the hygroscopic samples from air and moisture, and placed on a Nonius Kappa CCD X-ray diffractometer (Mo Kα λ = 0.71073 Å). Single-crystal X-ray diffraction data of $K_4M(MoO_4)_3$ (*M* = Cu, Zn) were collected at 390 K. The temperature was regulated with a warm stream of dry air produced by an Oxford cryostream. The unit cell parameters were determined from images taken at a rotation of 15 °φ. The structure was solved by SIR92[27] and refined by direct methods against F^2 by full-matrix least-squares techniques using SHELXL97.[28] The data were corrected for absorption, and the model was refined with anisotropic displacement parameters. Crystallographic data, atomic positions, and selected bond distances are provided in Tables 5.1, 5.2, and 5.3, respectively. The lattice dimensions of $K_4Zn(MoO_4)_3$ are similar to previously published orthorhombic $K_4Zn(MoO_4)_3$, which was modeled in the space group $P2_12_12_1$.[15] Modeling in the space group $P2_12_12_1$ resulted in missing symmetry when checked with PLATON.[29] Therefore we report the orthorhombic phases $K_4M(MoO_4)_3$ (*M* = Cu, Zn) modeled in the space group P*nma*.

Investigation of the structural transitions in $K_4Cu(MoO_4)_3$ yielded an apparent structural transition around 290 K. The reversible transition is similar to the previously reported monoclinic phase (~ 12 x 12 x 23 $Å^3$).[26] This transition is marked by a drastic decrease in crystal quality ($\chi^2 > 5$ and mosaicity ~ 2) and peak splitting. This phase is stable down to 90 K. Due to the complexity of the structure and to the complications arising from poor crystal quality of the low temperature phase, several attempts to solve the low temperature phase of $K_4Cu(MoO_4)_3$ were unsuccessful. We did not observe the reported hexagonal phase in $K_4Cu(MoO_4)_3$ up to 390 K, which is the high temperature limit for our structural determination via single crystal X-ray diffraction, and the experimentally observed phase transition temperatures in $A_4Cu(MoO_4)_3$ (A^+ =

K^+, Rb^+, Cs^+) are significantly different from those previously reported by Klevtsov shown below in Figure 5.1.[26]

5.2.3 Property Measurements

The magnetic susceptibility of single crystals were measured down to 1.9 K under magnetic fields *B* up to 7 T and the field- dependent magnetization at 2 K was measured up to 7

Table 5.1 Crystallographic Data Table for $K_4Cu(MoO_4)_3$ and $K_4Zn(MoO_4)_3$ (Orthorhombic, P*nma*)

Crystal data		
Composition	$K_4Cu(MoO_4)_3$	$K_4Zn(MoO_4)_3$
a (Å)	10.3520(6)	10.68800(10)
b (Å)	22.8070(7)	22.0220(10)
c (Å)	5.9380(10)	6.1050(10)
V (Å^3)	1402.0(3)	1436.9(3)
Z	4	4
Crystal size (mm^3)	0.03 x 0.03 x 0.03	0.05 x 0.11 x 0.12
Data Collection		
Temperature (K)	390	390
Measured reflections	4346	3843
Independent reflections	2469	2160
Reflections with I >2σ(I)	1623	1600
R_{int}	0.0371	0.0202
h	-15 → 15	-14 → 15
k	-33 → 34	-30 → 31
l	-8 → 8	-8 → 8
Refinement		
θ range (˚)	3.55-32.04	1.85-30.04
[a]$R_1[F^2>2\sigma F^2)]$	0.0397	0.0391
[b]$wR_2(F^2)$	0.0974	0.1177
Parameters	107	107
GoF on F^2	1.061	1.149
μ (mm^{-1})	5.355	5.414
$\Delta\rho_{max}$ (eÅ^{-3})	0.831	3.312
$\Delta\rho_{min}$ (eÅ^{-3})	-0.851	-1.232
Extinction coefficient (x10^{-4})	13(3)	8(2)

[a]$R_1 = \Sigma||F_0| - |F_c||/\Sigma|F_0|$

[b]$wR_2 = [\Sigma w(F_o^2 - F_c^2)^2/\Sigma w(F_0^2)^2]^{1/2}$; $P = (F_o^2 + 2F_c^2)/3$; $w = 1/[\sigma^2(F_o^2) + 0.0422P^2 + 1.2985P]$, $w = 1/[\sigma^2(F_o^2) + (0.0615P)^2 + 1.5504P]$, for $K_4Cu(MoO_4)_3$ and $K_4Zn(MoO_4)_3$, respectively.

Table 5.2 Atomic Positions of $K_4Cu(MoO_4)_3$ and $K_4Zn(MoO_4)_3$

Atom	Wyckoff	*x*	*y*	*z*	Occ.[a]	U_{eq} (Å^2)[b]
K1	8*d*	0.66644(11)	0.47425(5)	0.99930(17)	1.00	0.0422(3)
K2	8*d*	0.33352(13)	0.34137(5)	0.9528(2)	1.00	0.0453(3)
Cu	4*c*	0.50186(7)	¼	0.52051(12)	1.00	0.02838(19)
Mo1	8*d*	0.00243(3)	0.408274(16)	0.01607(6)	1.00	0.02413(13)
Mo2	8*d*	0.67114(7)	0.27229(3)	0.05702(12)	0.50	0.02833(19)
O1	8*d*	0.0896(4)	0.56163(16)	0.1969(6)	1.00	0.0637(11)
O2	4*c*	0.5296(5)	¼	0.9273(9)	1.00	0.0577(15)
O3	8*d*	0.0615(4)	0.57078(17)	0.7272(6)	1.00	0.0676(12)
O4	8*d*	0.0013(4)	0.33104(16)	0.9812(7)	1.00	0.0748(18)
O5	8*d*	0.1583(4)	0.43451(18)	0.9929(7)	1.00	0.0640(12)
O6	4*c*	0.8076(5)	¼	0.9174(9)	1.00	0.0566(14)
O7	4*c*	0.1709(4)	¼	0.1511(7)	1.00	0.0431(11)
O8	8*d*	0.6774(10)	0.3483(4)	1.0366(14)	0.50	0.067(3)
K1	8*d*	0.33335(13)	0.47447(7)	0.4989(2)	1.00	0.0410(3)
K2	8*d*	0.33314(18)	0.65770(6)	0.5213(2)	1.00	0.0440(4)
Zn	4*c*	0.03189(8)	¼	0.61270(15)	1.00	0.0312(2)
Mo1	8*d*	0.00088(4)	0.593417(19)	0.49846(7)	1.00	0.02391(17)
Mo2	8*d*	0.17304(8)	0.72768(4)	0.99479(14)	0.50	0.0267(2)
O1	4*c*	0.4764(6)	¼	0.5753(12)	1.00	0.0528(17)
O2	8*d*	-0.0010(5)	0.6741(2)	0.5228(9)	1.00	0.0544(14)
O3	4*c*	0.7127(5)	¼	0.8044(11)	1.00	0.0471(15)
O4	8*d*	0.1543(4)	0.5674(3)	0.5021(10)	1.00	0.0676(18)
O5	8*d*	0.4283(6)	0.5699(2)	0.2406(9)	1.00	0.0652(15)
O6	8*d*	0.4226(6)	0.5630(2)	0.7785(9)	1.00	0.0653(15)
O7	4*c*	0.7800(6)	¼	0.2601(10)	1.00	0.0521(16)
O8	8*d*	0.3350(14)	0.3516(5)	0.4811(18)	0.50	0.062(3)

[a]Occupancy

[b]U_{eq} is defined at one third of the trace of the orthogonalized U_{ij} tensor.

T with a MPMS SQUID magnetometer to investigate the magnetic properties of $K_4Cu(MoO_4)_3$. The experimental effective moment p_{eff}, *g*-value, Weiss temperature Θ_W, and constant term χ_0 are shown below in Table 5.4.

Table 5.3 Bond Distances (Å) of $K_4Cu(MoO_4)_3$ and $K_4Zn(MoO_4)_3$

Cu (distorted square planar)		Zn (tetrahedra)	
Cu-O4 (x2)	1.848(4)	Zn-O4 (x2)	1.893(5)
Cu-O7	2.025(4)	Zn-O7	1.995(7)
Cu-O6	2.045(5)	Zn-O6	1.997(6)
Cu-O2	2.433(5)		
Mo1 (tetrahedra)			
Mo1-O4	1.774(4)	Mo1-O5	1.732(5)
Mo1-O5	1.727(4)	Mo1-O3	1.733(5)
Mo1-O3	1.729(3)	Mo1-O1	1.738(5)
Mo1-O1	1.725(3)	Mo1-O4	1.784(5)
Mo2 (distorted tetrahedra)			
Mo2-Mo2	1.0168(14)	Mo2-Mo2	0.9831(18)
Mo2-O7	1.806(4)	Mo2-O2	1.707(6)
Mo2-O6	1.715(4)	Mo2-O7	1.742(6)
Mo2-O2	1.732(5)	Mo2-O8	1.750(10)
Mo2-O8	1.738(8)	Mo2-O6	1.799(6)
K1-O			
K1-O5	2.761(4)	K1-O8	2.708(11)
K1-O3	2.799(4)	K1-O3	2.761(5)
K1-O1	2.803(4)	K1-O1	2.801(5)
K1-O8	2.884(8)	K1-O5	2.817(5)
K1-O1	2.900(4)	K1-O5	3.158(7)
K1-O6	2.908(5)	K1-O3	3.158(7)
K1-O5	3.061(5)	K1-O1	3.172(7)
K1-O5	3.149(4)	K1-O1	3.210(6)
K1-O1	3.304(4)	K1-O3	3.217(7)
K2-O			
K2-O1	2.800(4)	K2-O2	2.716(4)
K2-O3	2.802(4)	K2-O1	2.761(6)
K2-O5	2.803(4)	K2-O5	2.776(5)
K2-O2	2.913(4)	K2-O3	2.781(5)
K2-O7	2.926(3)	K2-O6	2.886(5)
K2-O6	3.041(4)	K2-O7	2.937(5)
K2-O4	3.117(4)	K2-O4	3.320(6)
K2-O8	3.329(9)	K2-O8	3.339(13)

Table 5.4 Magnetic properties of $K_4Cu(MoO_4)_3$

	$K_4Cu(MoO_4)_3$		$Rb_4Cu(MoO_4)_3$	
	B // *ac*	*B* // *b*	*B* // *ac*	*B* // *b*
μ_{eff} (μ_B)	1.89(1)	1.79(1)	1.91	1.79
θ_W (K)	-2.32(1)	-1.89(1)	-5.01	-5.15
J	4.6	3.8	10.0	10.3

5.3 Results and Discussion

5.3.1 Crystal Structure of $K_4Cu(MoO_4)_3$

$K_4Cu(MoO_4)_3$, shown in Figure 5.2, is modeled in the orthorhombic P*nma* space group with lattice dimensions of *a* = 10.3520(6) Å, *b* = 22.8070(7) Å, *c* = 5.9380(10) Å. Although the structure determination is reported at 390 K, the transition from the low temperature phase to orthorhombic phases occurs at 280 K. The data collected at 390 K are reported here because crystal quality increased with increasing temperature and lower temperature data collections were not of sufficient quality to obtain an acceptable structural solution. To ensure phase stability of the orthorhombic phase at room temperature, powder X-ray diffraction was performed and the data were indexed to the 390 K single crystal model.

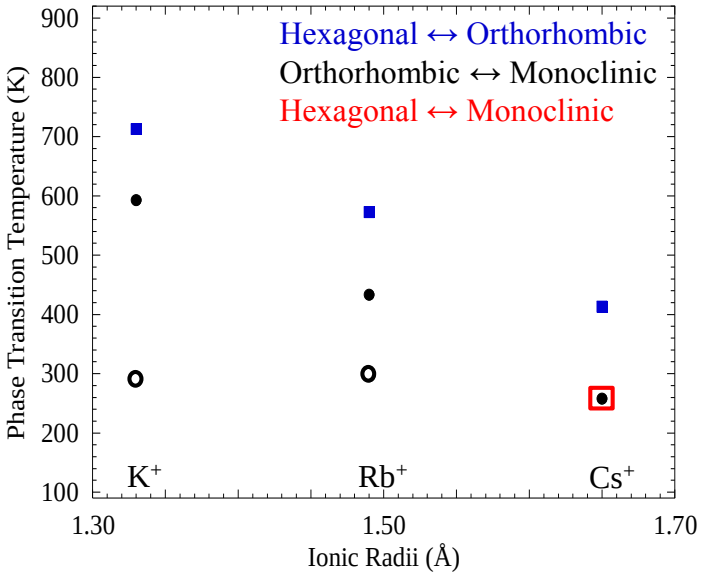

Figure 5.1 Phase transition temperatures (K) of $A_4Cu(MoO_4)_3$ (A^+ = K^+, Rb^+, Cs^+) as a function of ionic radii (Å). Closed markers represent transition temperatures previously reported and open markers represent transition temperatures determined experimentally.

$K_4Cu(MoO_4)_3$, shown in Figure 5.2a, is isostructural with the recently published $Rb_4Cu(MoO_4)_3$.[11] The structure can be described as distorted square planar CuO_4 polyhedra surrounded to two slightly distorted MoO_4 tetrahedra along the *c* direction and two distorted MoO_4 tetrahedra along the *ab*-plane, with partially occupied Mo2 (0.5) and O8 (0.5), as shown in Figure 5.2b. The Mo1-O distances of the slightly distorted MoO_4 tetrahedra range from 1.725(3) to 1.774(4) Å, which are similar to those found in $Rb_4Cu(MoO_4)_3$ (from 1.731(6) to 1.780(6) Å). The Mo2-O distances of the distorted, partially occupied MoO_4 tetrahedra range from 1.715(4) to 1.806(4) Å, which are roughly equivalent with those found in $Rb_4Cu(MoO_4)_3$ (1.674(14) to 1.806(12) Å). However the Mo2-O7 (1.806(4) Å) bond distance in the distorted tetrahedra is significantly longer than the other three Mo2-O bond distances (~1.72 Å).

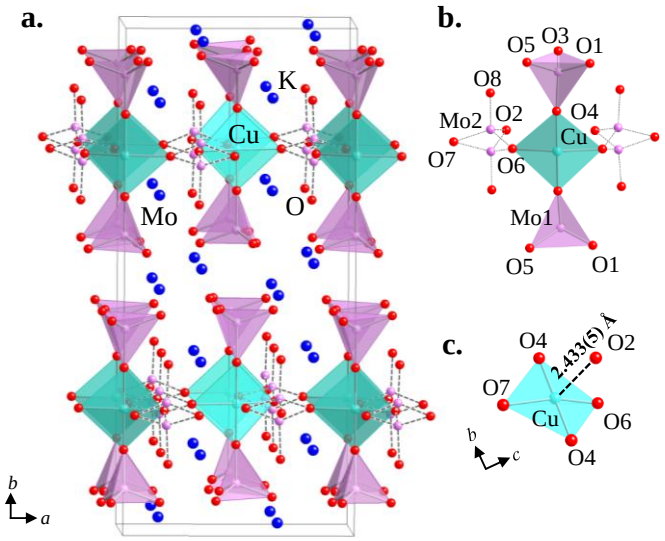

Figure 5.2 **a.** The crystal structure of $K_4Cu(MoO_4)_3$ with blue, green, pink, and red spheres representing K, Cu, Mo, and O atoms, respectively. **b.** The distorted Cu^{2+} square planar environment with the surrounding Mo-centered moieties. **c.** A view of the puckered Cu^{2+} square planar environment. The dashed lines represent bonds from partially occupied Mo atoms.

The Cu^{2+} square planar environment is illustrated in Figure 5.2c. The two Cu-O1 bonds (1.848(4) Å) of $K_4Cu(MoO_4)_3$, oriented along the *b*-direction, are shorter than the other two Cu-O bonds (Cu-O2 with 2.025(4) Å and Cu-O3 with 2.045(5) Å), see Figure 5.2b. The distortions in the MoO_4 tetrahedra and the CuO_4 square planar polyhedra in $K_4Cu(MoO_4)_3$ can be understood by electronic considerations. Mo^{6+} is more electron deficient (electronegative) than Cu^{2+} so Mo-O-Cu interactions are more

favorable than Mo-O-Mo interactions. This is consistent with the longer Cu-O contacts in the *ac*-plane and also the shorter Cu-O contacts along the *b*-axis.

Figure 5.3 shows the Cu-Mo-O chains in both $A_4Cu(MoO_4)_3$ (*A* = K, Rb). The ~ 2.3% shorter distance between chains in $K_4Cu(MoO_4)_3$, as compared to $Rb_4Cu(MoO_4)_3$, is consistent with the decrease in lattice parameter *c* between the two analogues on moving from $Rb_4Cu(MoO_4)_3$ (6.078(4) Å) to $K_4Cu(MoO_4)_3$ (5.938(4) Å). The Cu-O distances of the distorted square planar CuO_4 polyhedra in $K_4Cu(MoO_4)_3$ range from 1.848(4) to 2.045(5) Å with O-Cu-O angles of 90.01(12)°, 89.87(13)°, 179.3(3)° and 160.176(3)°. As discussed with respect to $Rb_4Cu(MoO_4)_3$, similar coupling between Cu^{2+} moments is possible through the superexchange

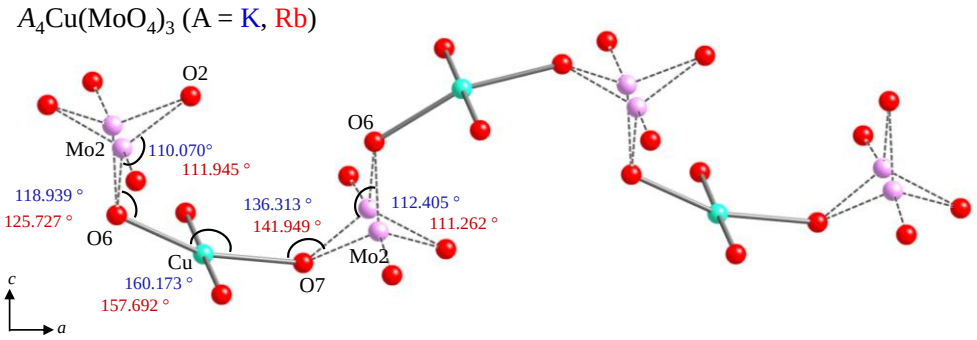

Figure 5.3 The Cu^{2+} quasi-1-*d* chains of both $K_4Cu(MoO_4)_3$ and $Rb_4Cu(MoO_4)_3$ are shown with the bond angles for $K_4Cu(MoO_4)_3$ in blue and $Rb_4Cu(MoO_4)_3$ in red. The dashed lines represent bonds from partially occupied Mo atoms.

mechanism.[11] The Cu^{2+} square planar environment in $K_4Cu(MoO_4)_3$ is shown in Figure 5.2c. The distance of Cu-O2 (2.432(5) Å) is slightly longer in $K_4Cu(MoO_4)_3$ compared to 2.400(15) Å found in $Rb_4Cu(MoO_4)_3$. This increase in distance between Cu and O2 and the orthogonal orientation between the $d_{x^2-y^2}$ orbital of Cu^{2+} and the p_z orbital of O^{2-} indicates that the superexchange pathway from Cu through O2 is weaker than that found in $Rb_4Cu(MoO_4)_3$, which should make $K_4Cu(MoO_4)_3$ more one-dimensional than $Rb_4Cu(MoO_4)_3$. The *M*-O-*M* bond

angles (*M* = Cu or Mo) are shown in Figure 5.3 with angles along the Cu-O-Mo chains in the K- and Rb-analogues represented in blue and red, respectively. The O-Cu-O bond angles of the Cu^{2+} square planar environment are ~ 2 % larger than the equivalent angles of the Rb-analogue which is also consistent with weaker orbital overlap between Cu and O2. The Mo-O-Cu bond angles along the chain are smaller (~ 5 %) in $K_4Cu(MoO_4)_3$ compared to those in $Rb_4Cu(MoO_4)_3$ indicating the K-analogue structurally is more distorted than the Rb-analogue which results in weaker orbital overlap between the *d*-orbitals of Mo^{6+} and Cu^{2+} and the *p*-orbital of O^{2-}. Therefore magnetic correlations between neighboring Cu^{2+} ions in $K_4Cu(MoO_4)_3$ are overall weaker than those in $Rb_4Cu(MoO_4)_3$.

5.3.2 Magnetic Properties of $K_4Cu(MoO_4)_3$

The temperature dependence of the magnetic susceptibility was measured at B = 0.01 T and 7 T for B // ac and B // b in the range of 2 – 350 K with the low temperature data (0 – 50 K) shown in Figure 5.4a. The magnetic susceptibility was measured across the structural transition (~ 280 K) with no indication of a magnetic transition, similar to the magnetic susceptibility of $Rb_4Cu(MoO_4)_3$.[11] The temperature-dependent polymorphs of $Rb_4Cu(MoO_4)_3$ are structurally very similar to each other and are built of the same structural moieties.

The magnetic susceptibility data were corrected for core electron diamagnetism in $K_4Cu(MoO_4)_3$, and the diamagnetic contribution to the magnetic susceptibility has been determined to be χ_{dia} = -288 x10^{-6} emu/mol.[30] No bifurcation was observed between ZFC and FC magnetic susceptibility measurements down to 0.01 T, which indicates that $K_4Cu(MoO_4)_3$ does not show the spin freezing behavior characteristic of a spin-glass system. The $\chi(T)$ data were fit with $\chi(T) = \chi_0 + C/(T - \Theta_W)$ (C = Curie-Weiss constant) for 30 – 350 K. χ_0 is a constant, representative of any diamagnetic and background contributions to the magnetic

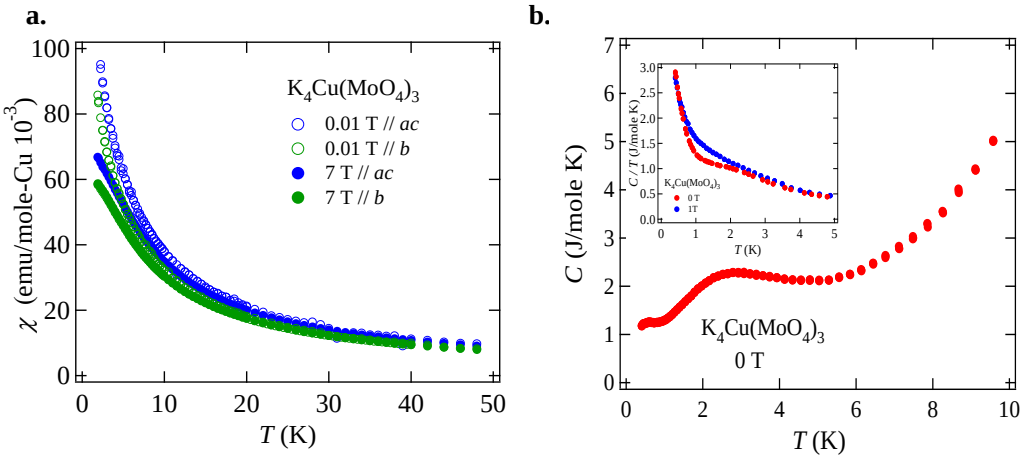

Figure 5.4 **a.** Magnetic susceptibility of $K_4Cu(MoO_4)_3$ is plotted below 50 K. Blue (Green) open and closed circles show magnetization *B // ac* and *B // b* in 0.01 T and 7 T, respectively. **b.** Specific heat of $K_4Cu(MoO_4)_3$ from 0.4 to 10 K is plotted at 0 T. The inset shows C/T as a function of T at 0 and 1 T.

susceptibility. The Weiss temperatures are negative for both directions, and indicate antiferromagnetic interactions between neighboring Cu^{2+} ions. While p_{eff} for *B // ac* is close to the theoretical value 1.73 μ_B for Cu^{2+} spin-$^1/_2$, p_{eff} for *B // b* is larger than expected which can be attributed to spin-orbital coupling. p_{eff} for *B // b* are consistent with that found for $Rb_4Cu(MoO_4)_3$.[11] However the p_{eff} for *B // ac* are slightly smaller than those for $Rb_4Cu(MoO_4)_3$. The magnetic anisotropy in $K_4Cu(MoO_4)_3$ is smaller than that found in $Rb_4Cu(MoO_4)_3$, which is consistent with weaker orbital overlap along the Cu-O-Mo chains as discussed in the structure section above. θ_W for *B // ac* and *B // b* is smaller in $K_4Cu(MoO_4)_3$ than those of $Rb_4Cu(MoO_4)_3$. The exchange interactions in $K_4Cu(MoO_4)_3$ are estimated to be $J \sim 4.6$ K and ~ 3.8 K from $\theta_W = -[zs(s + 1)J]/3$ ($z = 2$ is the number of nearest-neighbor magnetic ions) for a spin-½ 1-*d* antiferromagnetic chain. The broad peak in χ associated with the development of short-range order is not observed down to 2 K due to the small exchange interaction in $K_4Cu(MoO_4)_3$. The characteristic broad peak in $\chi(T)$ for a 1-*d* antiferromagnetic chain is known to appear at $T \sim 0.6\ J \sim \theta_W$.[37] The absence of a leveling off feature at the lowest temperature (2 K) of the susceptibility

measurement at 0.01 T suggests a small inclusion (~ several %) of Curie component of S = $^1/_2$. For quantum spin chain system, this type of "free" spin may often appear due to the imperfections of the structure, such as defects, edge of the chain, etc.

Finally, Figure 5.4b shows the specific heat *C/T* of $K_4Cu(MoO_4)_3$ as a function of *T* at 0 T. No sharp anomaly indicating a magnetic long-range order is observed down to 0.4 K. The weak low-*T* enhancement of *C/T* below 1 K is seen in the inset of Figure 7, and is attributable to the Schottky contribution from the free moment of (Cu^{2+}) S = $^1/_2$ with a volume fraction is 9.9 %.[31] Notably, there is a broad peak at ~ 2.3 K (~θ_W), which may be attributed to the development of short-range ordering. Indeed, the 1-*d* quantum spin chain systems are expected to form a broad peak in *C*(*T*) at *T* ~ 0.5*J*, and it is indeed the case here, providing evidence that most likely the system forms a quantum spin liquid state below ~ 2.3 K.[32]

5.4 Conclusion

We report the crystal structure and magnetic properties of a new quasi-1-*d* quantum antiferromagnet, $K_4Cu(MoO_4)_3$, and the crystal structure of its nonmagnetic reference, $K_4Zn(MoO_4)_3$. In comparison with the increased structural distortion along the Cu-O-Mo chains results in weaker orbital overlap between chains due to the increased Cu-O2 distance and along the Cu-O-Mo chains due to decreased Cu-O-Mo bond angles and the increase in distortion along the chains weakens the magnetic exchange interaction in $K_4Cu(MoO_4)_3$ (*J* ~ 4-5 K) as compared to $Rb_4Cu(MoO_4)_3$ (*J* ~ 10 K). This decrease in the coupling *J* results in suppression below 2 K of the broad peak expected for 1-*d* spin chains in magnetic susceptibility and is confirmed in specific heat measurements.[33] Therefore both $K_4Cu(MoO_4)_3$ and $Rb_4Cu(MoO_4)_3$ can be described as quantum spin-½ 1-*d* antiferromagnets with a likely quantum spin liquid ground state. Structural and magnetic comparison of $A_4Cu(MoO_4)_3$ (*A* = K, Rb) serves to isolate the

effects of low dimensionality from structural distortion on magnetic behavior and illustrates that structural distortion may be used as a tunable parameter when investigating quantum fluctuations.

5.5 References

(1) Anderson, P. W., The resonating valence bond state in La_2CuO_4 and superconductivity. *Science* **1987,** *235*, 1196-1198.

(2) Tsujimoto, Y.; Kitada, A.; Uemura, Y. J.; Goko, T.; Aczel, A. A.; Williams, T. J.; Luke, G. M.; Narumi, Y.; Kindo, K.; Nishi, M.; Ajiro, Y.; Yoshimura, K.; Kageyama, H., Two-dimensional s = 1 quantum antiferromagnet $(NiCl)Sr_2Ta_3O_{10}$. *Chem. Mater.* **2010,** *22*, 4625-4631.

(3) Nakatsuji, S.; Nambu, Y.; Tonomura, H.; Sakai, O.; Jonas, S.; Broholm, C.; Tsunetsugu, H.; Qiu, Y.; Maeno, Y., Spin disorder on a triangular lattice. *Science* **2005,** *309*, 1697-1700.

(4) Knetter, C.; Muller-Hartmann, E.; Uhrig, G. S., Symmetries and triplet dispersion in a modified Shastry-Sutherland model for $SrCu_2(BO_3)_2$. *J. Phys.-Condens. Mat.* **2000,** *12*, 9069-9083.

(5) Kimura, T.; Lashley, J. C.; Ramierz, A. P., Inversion-symmetry breaking in the noncollinear magnetic phase of the triangular-lattice antiferromagnet $CuFeO_2$. *Phys. Rev. B* **2006,** *73*, 220401.

(6) Dagotto, E.; Rice, T. M., Surprises on the way from one- to two-dimensional quantum magnets: the ladder materials. *Science* **1996,** *271* (5249), 618-623.

(7) Colman, R. H.; Ritter, C.; Wills, A. S., Toward perfection: kapellasite, $Cu_3Zn(OH)_6Cl_2$, a new model s = 1/2 kagome antiferromagnet. *Chem. Mater.* **2008,** *20*, 6897-6899.

(8) Alves, L. M. S.; Damasceno, V. I.; dos Santos, C. A. M.; Bortolozo, A. D.; Suzuki, P. A.; Filho, H. J. I.; Machado, A. J. S.; Fisk, Z., Unconventional metallic behavior and superconductivity in the K-Mo-O system. *Phys. Rev. B* **2010,** *81*, 174532.

(9) Torardi, C. C.; McCarley, R. E., Some reduced ternary and quaternary oxides of molybdenum. a family of compounds with strong metal-metal bonds. *J. Solid State Chem.* **1981,** *37* (3), 393-397.

(10) Ramanujachary, K. V.; Greenblatt, M., Synthesis and characterization of a new modification of the quasi-low-dimensional compound KMo_4O_6. *J. Solid State Chem.* **1993,** *102*, 69-78.

(11) Ishii, R.; Gautreaux, D.; Onuma, K.; Machida, Y.; Maeno, Y.; Nakatsuji, S.; Chan, J. Y., Low-dimensional structure and magnetism of the quantum antiferromagnet $Rb_4Cu(MoO_4)_3$ and the structure of $Rb_4Zn(MoO_4)_3$. *J. Am. Chem. Soc.* **2010,** *132*, 7055-7061.

(12) da Luz, M. S.; dos Santos, C. A. M.; Moreno, J.; White, B. D.; Neumeier, J. J., Anisotropic electrical resistivity of quasi-one-dimensional $Li_{0.9}Mo_6O_{17}$ determined by the montgomery method. *Phys. Rev. B* **2007,** *76* (23), 233105.

(13) Greenblatt, M., Molybdenum oxide bronzes with quasi-low-dimensional properties. *Chem. Rev.* **1988,** *88* (1), 31-53.

(14) Trunov, K.; Efremov, V. A.; Velikodnyi, Y. A., Crystal chemistry & properties of double molybdates & tungstates *Nauka, Leningrad* **1986**, 25-170.

(15) Gicquel-Mayer, C.; Mayer, M.; Perez, G., Study of structure of double molybdate $K_4Zn(MoO_4)_3$. *Chem. Minerale* **1980,** *17*, 445-457.

(16) Gicquel-Mayer, C.; Mayer, M.; Perez, G., Structural study of molydate $K_4Zn(MoO_4)_3$. *Chem. Minerale* **1976,** *283*, 533-535.

(17) Solodovnikov, S. F.; Klevtsova, R. F.; Glinskaya, L. A.; Klevtsov, P. V., Crystal structure of $Cs_4Cu(MoO_4)_3$ and $Rb_4Mn(MoO_4)_3$. *Kristallografiya* **1988,** *33*, 1380-1386.

(18) Solodovnikov, S. F.; Klevtsova, R. F.; Klevtsov, P. V., A correlation between the structure and some physical properties of binary molybdates (tungstates) of uni- and bivalent metals. *J. Structural Chem.* **1994,** *35*, 879-889.

(19) Solodovnikov, S. F.; Klevtsova, R. F.; Glinskaya, L. A.; Klevtsov, P. V., Solid-phase synthesis, crystalization & properties of double potassium manganese molybdates. *Zh. Neorg.Khim.* **1994,** *39*, 1942-1947.

(20) Solodovnikov, S. F.; Klevtsova, R. F.; Glinskaya, L. A.; Klevtsov, P. V., Synthesis and crystal-structural study of $Rb_4Mn(MoO_4)_3$ and $Cs_4Cu(MoO_4)_3$. *Kristallografiya* **1988,** *33*, 1380-1386.

(21) Sarma, D. D., A new class of magnetic materials: Sr_2FeMoO_6 and related compounds. *Curr. Opin. Solid St. M.* **2001,** *5*, 261-268.

(22) Huang, Y.-H.; Liang, G.; Croft, M.; Lehtimäki, M.; Karppinen, M.; Goodenough, J. B., Double-perovskite anode materials Sr_2MMoO_6 (*M* = Co, Ni) for solid oxide fuel cells. *Chem. Mater.* **2009,** *21* (11), 2319-2326.

(23) Solodovnikov, S.; Solodovnikova, Z. A., New structure type in the morphotropic series of $A^{2+}M_2^{2+}(MoO_4)_3$: crystal structure of $Rb_2Cu_2(MoO_4)_3$. *J. Structural Chem.* **1997,** *38*, 765-771.

(24) Svistov, L. E.; Smirnov, A. I.; Prozorova, L. A.; Petrenko, O. A.; Demianets, L. N.; Shapiro, A. Y., Quasi-two-dimensional antiferromagnet on a triangular lattice $RbFe(MoO_4)_2$. *Phys. Rev. B* **2003,** *67*, 094434.

(25) Ishii, R.; Tanaka, S.; Onuma, K.; Nambu, Y.; Tokunaga, M.; Sakakibara, T.; Kawashima, N.; Maeno, Y.; Broholm, C.; Gautreaux, D. P.; Chan, J. Y.; Nakatsuji, S., Successive phase transitions and phase diagrams for the quasi-two-dimensional easy-axis triangular antiferromagnet $Rb_4Mn(MoO_4)_3$. *Europhys. Lett.* **2011,** *94*, 17001.

(26) Klevtsov, P. V.; Kim, V. G.; Kruglik, A. I.; Klevtsova, R. F., Synthesis and phase transitions of double molybdates $M_4Cu(MoO_4)_3$ (*M*= Cs, Rb, K). *Kristallografiya* **1989,** *34*, 1475-1479.

(27) Altomare, A.; Burla, M. C.; Camalli, M.; Cascarano, G.; Giacovazzo, C.; Guagliardi, A.; Polidori, G., SIR92 - a program for automatic solution of crystal structures by direct methods. *J. Appl. Crystallogr.* **1994,** *27*, 435.

(28) Sheldrick, G. M., A short history of SHELX. *Acta Crystallogr. Sect. A.: Found Crystallogr.* **2008,** *A64*, 112-122.

(29) Spek, A. L., PLATON, a multipurpose crystallographic tool. *J. Appl. Crystallogr.* **2003,** *36*, 7-13.

(30) Selwood, P. W., *Magnetochemistry*. Interscience: New York, 1956.

(31) Ramirez, A. P.; Cheong, S.-W.; Kaplan, M. L., Specific heat of defects in Haldane systems Y_2BaNiO_5 and NENP: absence of free spin-$^1/_2$ excitations. *Phys. Rev. Lett.* **1994,** *72*, 3108-3111.

(32) Johnston, D. C.; Kremer, R. K.; Troyer, M.; Wang, X.; Klumper, A.; Bud'ko, S. L.; Panchula, A. F.; Canfield, P. C., Thermodynamics of spin S = $^1/_2$ antiferromagnetic uniform and alternating-exchange Heisenberg chains. *Phys. Rev. B.* **2000,** *61*, 9558-9606.

(33) Eggert, S.; Affleck, I.; Takahashi, M., Susceptibility of the spin $^1/_2$ Heisenberg antiferromagnetic chain. *Phys. Rev. Lett.* **1994,** *73*, 332-335.

CHAPTER 6. CONCLUSIONS-WANTED DEFECTS AND DISTORTIONS!

My research focuses on growing and characterizing single crystals of three different types of complex materials: Complex 3-*d* intermetallic compounds, 2-*d* frustrated sulfides, and quasi-1-*d* antiferromagnetic oxides. Continued progress in this area of research will benefit from considerations of crystal growth, structural disorder, and phase formation. Disorder and dimensionality play central roles in both the structural characterization and the correlation of structure to properties. Disorder can also be used as a tunable parameter when substituting elements in a given structure by considering atomic sizes, coordination preferences, and electronegativity differences.

6.1 Crystal Growth of Structurally Disordered Phases

Flux growth is an effective crystal growth method in the search for new, structurally disordered phases. Multiple-step heating/cooling sequences, similar to that used in the growth of $Ln_2Ag_{1-x}Ga_{10-y}$ (*Ln* = La, Ce)[1] and β-$LnNi_{1-x}Ga_4$ (*Ln* = Tb-Er)[2], allow for the growth of new phases that are not accessible by using "heat and beat" methods. The degree of disorder, the narrow homogeneity range, the narrow growth temperature range, and the transformation to more robust phases with annealing attest to the metastable nature of the $Ln_2Ag_{1-x}Ga_{10-y}$ (*Ln* = La, Ce) and β-$LnNi_{1-x}Ga_4$ (*Ln* = Tb-Er) phases compared to the robust, structurally ordered ($BaAl_4$-type) $LnAg_xGa_{4-x}$ (*Ln* = La, Ce)[3] and α-$LnNiGa_4$ (*Ln* = Tb-Er) phases,[2] respectively. Future work in the search for new ternary intermetallic phases could focus on trapping undiscovered, metastable phases through two-step cooling sequences similar to those of $Ln_2Ag_{1-x}Ga_{10-y}$ (*Ln* = La, Ce) and β-$LnNi_{1-x}Ga_4$ (*Ln* = Tb-Er).

Future work in the discovery of new intermetallic phases can also focus on the use of differential thermal analysis (DTA) technique as a screening mechanism. By heating the chosen

elements in the desired mole ratios, the resulting peaks determined by a DTA scan indicate not only the number of different phases but also the optimal growth temperature for each phase.[4] In addition the role of various parameters, such as the type of crucible or flux, can be investigated using the DTA technique. The optimum growth conditions and the role of the crucible type have been determined for TbAl, $Pr_7Ni_2Si_5$, and $YbMn_4Al_8$ phases using DTA.[4] Especially in relatively unexplored phase space, the addition of DTA to our structural characterization toolbox would increase productivity and efficiency by determining the number of different phases and the optimal growth temperature for each desired phase.[4]

6.2 Local Structure Determination and the Characterization of Complex Materials

The characterization of high quality single crystals is always one of the first steps in understanding interactions at the atomic level. Without a good structural model, local structure determination is a very daunting, sometimes impossible task. Therefore classic crystallography methods, such as powder and single crystal X-ray diffraction, and total scattering methods, such as pair distribution function analysis, are needed to see the complete structural picture. Understanding the complete structural picture may not only lead to modifications of desired properties but also to the discovery of new materials.

In studying complex materials, there are two points of view, global and local. The crystal structure determined by powder and single crystal X-ray diffraction represent the global view. The local structure can be unveiled by pair distribution function (PDF) analysis. The PDF method is complementary to powder and single crystal X-ray diffraction (XRD). Local deviations from the ordered atomic arrangement of a crystalline material are seen in powder and single crystal XRD as disorder and are expressed as enlarged, anomalous atomic displacement parameters. Local deviations in PDF analysis are expressed as shifts in the PDF peaks which

allow for the distinction between random and correlated deviations.[5] The PDF is a Fourier transform of the total scattering intensity (G(r)) of a crystalline material as a function of distance (r) from a reference atom.[5] Atomic distances are determined from peak positions. The local atomic environment is determined by peak area. The degree of disorder is determined by the peak width. The particle size and coherence are determined by r_{max} (the maximum distance (Å) of interaction).

The pair distribution function has been applied to complex materials illuminating unexpected behavior not discernible from the average crystal structure. The characterization of disordered phases using the PDF method may illuminate the differences in the local environment of structurally related phases and allow for detailed analysis of structure and property relations.[5] For example, the O-O distances in the local Cu environment of $Tl_2Ba_2CaCu_2O_8$ do not increase at high temperature as predicted due to thermal vibrations but peak around the superconducting temperature.[6] Microscopic phase separation has been observed in neutron powder PDF measurements of the superconducting $La_{2-x}Sr_xCuO_4$ (T_C = 33 K) indicating regions of metallic and insulating stripes which may be required for superconductivity.[7-8] In addition to correlating structure to properties, materials with competing interactions are often very sensitive to small changes and have complex structures. For example, the local structure of $La_{1-x}Sr_xMnO_3$ determined by pulsed neutron powder diffraction indicates Jahn-Teller distortions of the Mn octahedra become positionally disordered below the metal-to-insulator transition temperature.[9-10] By determining the local structure of disordered phases such as $Ce_2Ag_{1-x}Ga_{10-y}$ and β-$Ln Ni_{1-x}Ga_4$ (*Ln* = Tb-Er), we can better understand the effects of structural disorder and perhaps lend support to our structural description of inhomogeneous intergrowth phases consisting of disordered variants of simple structures.

6.3 Stumbling onto a Gold Mine - Serendipitous Growth of $ThSi_2$- and AlB_2-types of $CeAg_ySi_{2-x}Ga_{x-y}$ Phases

As often happens in solid state chemistry, the growth of $ThSi_2$- and AlB_2-types $CeAg_ySi_xGa_{2-x-y}$ phases was a serendipitous result of the optimization of the growth of $Ce_2Ag_{1-x}Ga_{10-y}$ by varying the reaction profile.[1] Following the serendipitous growth of these phases, a literature search revealed the existence several related phases shown schematically in Figure 6.1. The growth and characterization of $CeGa_2$ and $CeSi_2$ has the spurred investigation of the following related phases. $CeSi_2$ ($ThSi_2$-type) has been reported as a mixed valent $Ce^{3+/4+}$ compound exhibiting heavy fermion behavior($\gamma \sim 100$ mJ/K^2-molCe) with strong ferromagnetic correlations ($\theta \sim 302$ K) but no long range magnetic ordering down to 100 mK.[11-12] $CeGa_2$ (AlB_2-type) exhibits Kondo-screened Ce^{3+} moments with multiple magnetic transitions due to

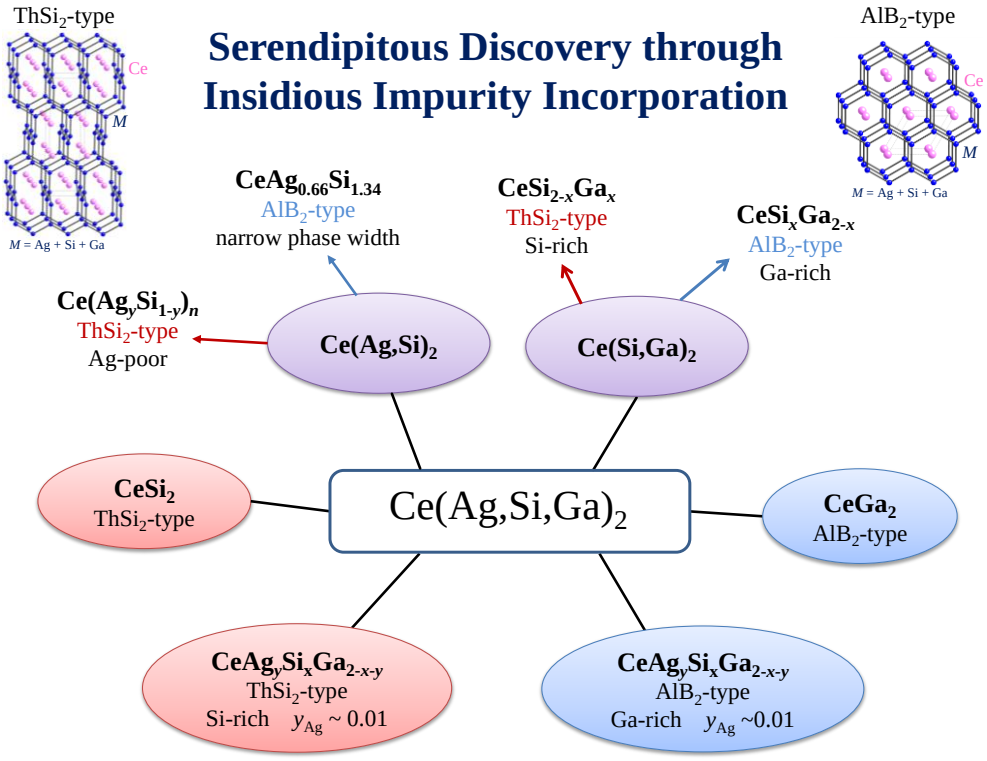

Figure 6.1 This diagram illustrates the competition between $ThSi_2$- and AlB_2-type phases in the $Ce(Ag,Si,Ga)_2$ system.

complex wave modulations of the magnetic moments near 9 K.[13] Following the observation of interesting behavior in these compounds, the next logical step was the growth and characterization of the $CeSi_xGa_{2-x}$ phases (both AlB_2 and $ThSi_2$-types). The Si-rich variant, $CeSi_xGa_{2-x}$ ($ThSi_2$-type) ($0.7 \leq x \leq 2.0$) has a large Sommerfeld parameter and a tunable magnetic ground state that varies with x.[14-16] A structural transition from the $ThSi_2$-type to the AlB_2-type structure occurs ($x \sim 0.6$) with increasing Ga concentration.[14, 17] Polycrystalline magnetic susceptibility and heat capacity measurements on AlB_2-type $CeSi_xGa_{2-x}$ ($0 \leq x \leq 0.6$) indicate a shift from antiferromagnetic to ferromagnetic correlations with increasing Si concentration.[17-18] Ag-doped experiments on $CeSi_2$ have yielded $ThSi_2$- and AlB_2-type $Ce(Ag,Si)_2$ phases. The defect variant of the $ThSi_2$-structure $Ce(Si_{1-y}Ag_y)_n$ ($0.08 < y < 0.30$) orders ferromagnetically below 7 K and antiferromagnetically at 5.7 K for $y = 0.31$.[19] AlB_2-type $CeAg_{0.66}Si_{1.34}$ displays soft ferromagnetism below 5 K.[19] The Ag-doped variant of the AlB_2-type $CeGa_2$ phase has not been reported but a $CeCu_2$-type $Ce(Ag,Ga)_2$ has been reported.[20-21]

Our decision to continue characterizing these phases stems from the presence of heavy fermion behavior in $CeSi_{2-x}Ga_x$ ($ThSi_2$-type),[14-16] the ferromagnetic Ce^{3+} correlations in $ThSi_2$-type $Ce(Si_{1-y}Ag_y)_{2-n}$ for ($0.08 \leq y \leq 0.3$; $0 < n \leq 0.22$),[19] the superconducting state of AlB_2-type $Yb(Si,Ga)_2$ ($1.41 \leq T_C \leq 2.4$ K),[22] and the curious absence of the AlB_2-type $CeAg_xGa_{2-x}$ phase.[21, 23]Interestingly, the effect of Ag atoms on transport and magnetic properties in this family of phases remains an open question due to the lack of magnetic and transport property measurements for these $LnAg_xGa_{2-x}$ (Ln = lanthanide) phases. The structural and physical characterization of $ThSi_2$- and AlB_2-types $CeAg_ySi_xGa_{2-x-y}$ phases are discussed below to highlight the challenges and serendipitous results of crystal growth.

6.3.1 Competition between AlB_2-type and $ThSi_2$-type $CeAg_ySi_xGa_{2-x-y}$ Phases

Our previous work growing the $Ce_2Ag_{1-x}Ga_{10-y}$ phases yielded layered aggregates with typical single crystal size of approximately 0.025 x 0.5 x 0.5 mm^3. We hoped to grow larger single crystals by increasing the dwell time at 1150 °C to 120 h. The reaction profile required heating the sample to 1150 °C at 200 °C/hour, dwelling for 120 hours, cooling to 650 °C at 150 °C/hour, followed by dwelling for 2 days and spinning. Prior to sealing the reaction ampoule, silica wool was placed in the fused-silica tube to serve as a filter during spinning to remove excess flux. Cracking open the reaction ampoule revealed beautiful, silver-colored plate- and rod-shaped crystals covered in melted silica wool. Hot water and dilute HCl were used to remove excess Ga from the surface of the crystals.

Investigation of the reaction conditions necessary for the growth of the $ThSi_2$- versus the AlB_2-type $CeAg_ySi_xGa_{2-x-y}$ phases has illuminated a curious competition between these two phases. The reaction ratio for the growth of AlB_2-type $CeAg_ySi_xGa_{2-x-y}$ is 2:1:0.5:20 moles of Ce:Ag:Si:Ga with all growths containing 30% impurity of the $ThSi_2$-type phase $CeAg_ySi_xGa_{2-x-y}$. The reaction ratio for the $ThSi_2$-type $CeAg_ySi_xGa_{2-x-y}$ is 2:0.5:1:20 moles of Ce:Ag:Si:Ga. All growths with Ag:Si ratios ≤ 1:10 yield only $ThSi_2$-type $CeAg_ySi_xGa_{2-x-y}$. Higher Ag:Si (2:0.5) molar ratios yield poor quality, polycrystalline samples of $BaAl_4$-type $CeAg_xGa_{4-x}$, and lower Ag:Si (1:10) molar ratios yield the $ThSi_2$-type $CeSi_xGa_{2-x}$ phase without Ag incorporation. Currently crystals of both the $ThSi_2$- and AlB_2-type $CeAg_ySi_xGa_{2-x-y}$ are being annealed to investigate the possibility of phase transformation in this system. Phase transformation has been demonstrated in $Ce(Si_{1-x}Ag_x)_{2-y}$[19] and $Ce_2Ag_{1-x}Ga_{10-y}$.[1] $ThSi_2$-type $Ce(Si_{1-x}Ag_x)_{2-y}$ crystals reportedly transformed to AlB_2-type $Ce(Si_{1-x}Ag_x)_{2-y}$ after annealing at 850 °C. While investigating the growth conditions of $Ce_2Ag_{1-x}Ga_{10-y}$, we observed the transformation of crystals

of Ce_2NiGa_{10}-type $Ce_2Ag_{1-x}Ga_{10-y}$ to $BaAl_4$-type $CeAg_xGa_{4-x}$ by annealing at 750 °C.[1] These transformations highlight the metastability of $ThSi_2$-type $Ce(Si_{1-x}Ag_x)_{2-y}$ and Ce_2NiGa_{10}-type $Ce_2Ag_{1-x}Ga_{10-y}$ with respect to AlB_2-type $Ce(Si_{1-x}Ag_x)_{2-y}$ and $BaAl_4$-type $CeAg_xGa_{4-x}$.

The temperature profile was also systematically investigated to determine the optimal conditions for crystal growth of these two phases. The high dwell temperature (1000 or 1150 °C), dwell time at high temperature (72 or 120 h), and spinning temperature (650 or 750 °C) are important for phase formation and for crystal quality. The heating rates, cooling rate, and dwell time prior to spinning have no significant effect on phase formation or crystal quality.

6.3.2 Powder X-ray Diffraction, Single-Crystal X-ray Diffraction, and Elemental Analysis

Crystals of both the $ThSi_2$-type and AlB_2-type $CeAg_ySi_xGa_{2-x-y}$ phases were ground, independently, for characterization by X-ray powder diffraction using a Bruker AXS D8 Advance diffractometer to confirm phase purity. Powder diffraction patterns from different batches were also compared to confirm phase purity. Independent powder diffraction on rods (AlB_2-type) or plates ($ThSi_2$-type) confirmed the phase purity of $ThSi_2$-type and AlB_2-type $CeAg_ySi_xGa_{2-x-y}$ phases, respectively, and indicated that these phases can be separated by crystal morphology.

Silver-colored fragments of single crystals were mounted on the goniometer of a Nonius Kappa CCD diffractometer equipped with Mo Kα radiation (λ = 0.71073 Å) for characterization by X-ray diffraction (XRD). The $ThSi_2$-type $CeAg_ySi_xGa_{2-x-y}$ phase grows as plate-like single crystals (0.5 x 2 x 2 mm^3), and the AlB_2-type $CeAg_ySi_xGa_{2-x-y}$ phase grows as rod-like single crystals (0.3 x 1 x 1 mm^3). Data were collected up to θ = 31 ° at 298 K. SIR92[24] was used to obtain a starting model for all the samples, and SHELXL-97[25] was used for structure refinement. The data for all the samples were corrected for absorption, extinction and refined with

anisotropic displacement parameters. All the refinement models were checked for missing symmetry elements using PLATON.[26] Crystallographic data, atomic positions, and interatomic distances are given in Table 6.1, 6.2 and 6.3, respectively.

Table 6.1 Crystallographic Data of $ThSi_2$-type and AlB_2-type $CeAg_ySi_{2-x-y}Ga_x$

Crystal data		
Composition	$CeAg_{0.01(1)}Si_{0.9(1)}Ga_{1.0(1)}$	$CeAg_{0.01(1)}Si_{0.1(1)}Ga_{1.9(1)}$
Space group	$I4_1/amd$	$P6/mmm$
a (Å)	4.2440(10)	4.2720(12)
c (Å)	14.2820(17)	4.3450(16)
V (Å^3)	257.24(9)	68.67(4)
Z	4	1
Crystal size (mm^3)	0.03 x 0.03 x 0.05	0.02 x 0.02 x 0.003
Data Collection		
Temperature (K)	298(2)	298(2)
Measured reflections	283	222
Independent reflections	129	64
Reflections with I > 2σ(I)	118	59
R_{int}	0.0580	0.0341
h	-5 → 6	-6 → 6
k	-3 → 4	-4 → 4
l	-13 → 19	-6 → 3
Refinement		
θ range (˚)	0.970-31.02	1.00-30.85
$^aR_1[F^2 > 2\sigma F^2)]$	0.0465	0.0447
$^bwR_2(F^2)$	0.1296	0.1287
Parameters	8	5
GooF on F^2	1.556	1.399
μ (mm^{-1})	28.926	34.530
Δp_{max} (e Å^{-3})	1.625	3.835
Δp_{min} (e Å^{-3})	-2.179	-2.103
Extinction coefficient	0.041(6)	0.05(3)

$^aR_1 = \Sigma||F_0| - |F_c||/\Sigma|F_0|$
$^bwR_2 = [\Sigma w(F_o^2 - F_c^2)^2/\Sigma w(F_0^2)^2]^{1/2}$; $P = (F_o^2 + 2F_c^2)/3$; $w = 1/[\sigma^2(F_o^2) + 0.0179P^2 + 5.0629P]$ for $CeAg_{0.01(1)}Si_{0.9(1)}Ga_{1.0(1)}$ and $w = 1/[\sigma^2(F_o^2) + (0.0493P)^2 + 3.1286P]$ for $CeAg_{0.01(1)}Si_{0.1(1)}Ga_{1.9(1)}$.

A Hitachi S-3600N scanning electron microscope with an energy dispersive X-ray spectrometer (SEM-EDXS) was used to analyze the elemental content of single crystals of $ThSi_2$-type and AlB_2-type $CeAg_ySi_xGa_{2-x-y}$ phases. Experimental parameters included an accelerating voltage of 15 kV and a beam-to-sample distance of 15 mm. Several crystals from multiple growths were scanned at 5 areas/crystal for 100 seconds/area. The average composition

was normalized to *Ln* (*Ln* = lanthanide) to yield $CeAg_{0.01(1)}Si_{0.9(1)}Ga_{1.1(1)}$ for $ThSi_2$-type $CeAg_ySi_xGa_{2-x-y}$ and $CeAg_{0.01(1)}Si_{0.1(1)}Ga_{1.9(1)}$ for AlB_2-type $CeAg_ySi_xGa_{2-x-y}$. The composition of each phase obtained by SEM analysis is consistent, within error, with the refined composition determined by single crystal X-ray diffraction studies.

Table 6.2 Atomic Positional & Displacement Parameters of $ThSi_2$-type & AlB_2-type $CeAg_ySi_{2-x-y}Ga_x$

298 K						
Atom	Wyckoff position	*x*	*y*	*z*	Occ.[a]	U_{eq} (Å^2)[b]
$CeAg_{0.01(1)}Si_{0.9(1)}Ga_{1.0(1)}$						
Ce	4*b*	0	¼	$^3/_8$	1.00	0.0109(6)
$^{\dagger}M$	8*e* (Ag (0.5%) + Si (45%) + Ga (54.5%))	0	¼	0.20861(17)	1.00	0.0155(7)
$CeAg_{0.01(1)}Si_{0.1(1)}Ga_{1.9(1)}$						
Ce	1*a*	0	0	0	1.00	0.0106(8)
$^{\dagger}M$	2*d* (Ag (0.5%) + Si (5%) + Ga (94.5%))	⅓	⅔	½	1.00	0.0134(10)

$^{\dagger}M$ = Ag + Si + Ga
[a]Occupancy
[b]U_{eq} is defined at one third of the trace of the orthogonalized U_{ij} tensor.

Table 6.3 Interatomic Distances (Å) of $ThSi_2$-type and AlB_2-type $CeAg_ySi_{2-x-y}Ga_x$

$CeAg_{0.01(1)}Si_{0.9(1)}Ga_{1.0(1)}$		$CeAg_{0.01(1)}Si_{0.1(1)}Ga_{1.9(1)}$	
	Distances (Å)		Distances (Å)
Ce-$^{\dagger}M$ (x4)	3.1859(19)	Ce-$^{\dagger}M$ (x12)	3.2849(7)
Ce-$^{\dagger}M$ (x8)	3.2298(10)	$^{\dagger}M$-$^{\dagger}M$ (x3)	2.4639(7)
$^{\dagger}M$-$^{\dagger}M$ (x1)	2.388(3)		
$^{\dagger}M$-$^{\dagger}M$ (x2)	2.4291(17)		

$^{\dagger}M$ = Ag + Si + Ga

The composition of each growth was checked using EDXS to investigate the homogeneity range of Ag, Si, and Ga in these phases. Consistent with the refined composition determined from single crystal XRD, AlB_2-type $CeAg_ySi_xGa_{2-x-y}$ crystals have the composition $CeAg_{0.01(1)}Si_{0.1(1)}Ga_{1.9(1)}$ and the $ThSi_2$-type $CeAg_ySi_xGa_{2-x-y}$ crystals have the composition $CeAg_{0.01(1)}Si_{0.9(1)}Ga_{1.1(1)}$. Temperature- and field-dependent magnetization was measured

multiple times on single crystals from different growths to investigate the effects of the narrow phase width on magnetic properties.

6.3.3 Structure and Magnetic Properties of $ThSi_2$-type $CeAg_{0.01(1)}Si_{0.9(1)}Ga_{1.1(1)}$

The tetragonal $ThSi_2$-type structure, shown in Figure 6.2a can be described as Ce atoms located in the channels created by a 3D network of *M* (*M* = Ag + Ga + Si) atoms. The *M* atoms are statistically distributed on the 8*e* (*mm*) site. The Ce-*M* interatomic distances (< 3.1 Å) are longer than expected for covalently bonded Ce-*M* contacts (~ 2.8 Å), but the *M*-*M* interatomic distances (2.388(3) Å and 2.4291(17) Å) are consistent with covalently bonded *M*-*M* contacts (2.34 Å ≤ *M*-*M* ≤ 2.59 Å).[27]

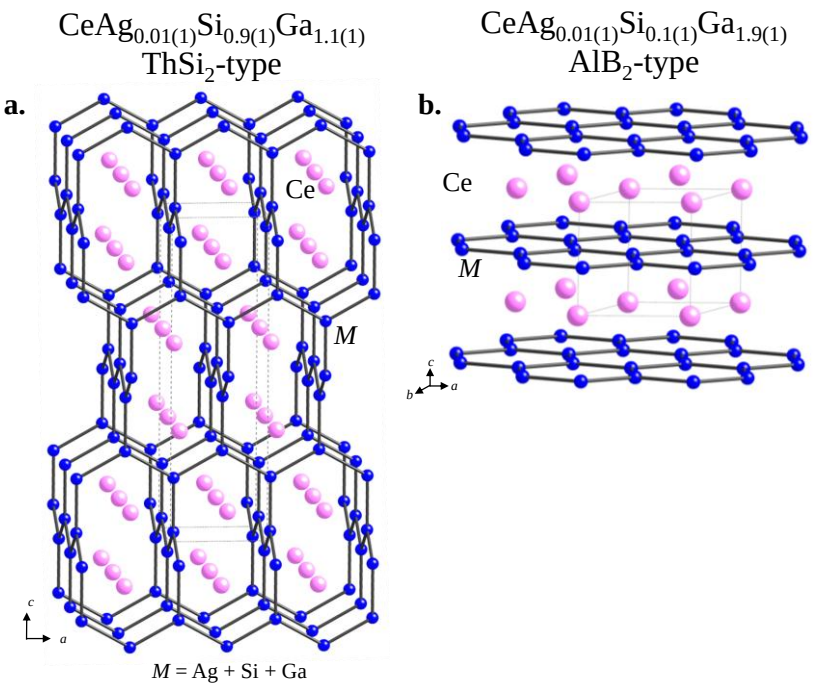

Figure 6.2 The crystal structures of **a.** $CeAg_{0.01(1)}Si_{0.9(1)}Ga_{1.1(1)}$ and **b.** $CeAg_{0.01(1)}Si_{0.1(1)}Ga_{1.1(1)}$ are shown with Ce and *M* (*M* = Ag + Si + Ga) atoms represented by pink and blue spheres, respectively.

Temperature-dependent magnetic susceptibility and field-dependent magnetization measurements of single crystals from multiple growths are shown in Figure 6.3. The $ThSi_2$-type $CeAg_{0.01(1)}Si_{0.9(1)}Ga_{1.1(1)}$ phase is paramagnetic down to 3 K with antiferromagnetic correlations (θ_W = -18.8(6)) between Ce^{3+} moments (μ_{eff} = 1.159(2)). The θ_W and μ_{eff} values are consistent with the antiferromagnetic, Kondo-screened Ce^{3+} moments in Ga-rich ($x \geq 1.5$) $CeSi_xGa_{2-x}$

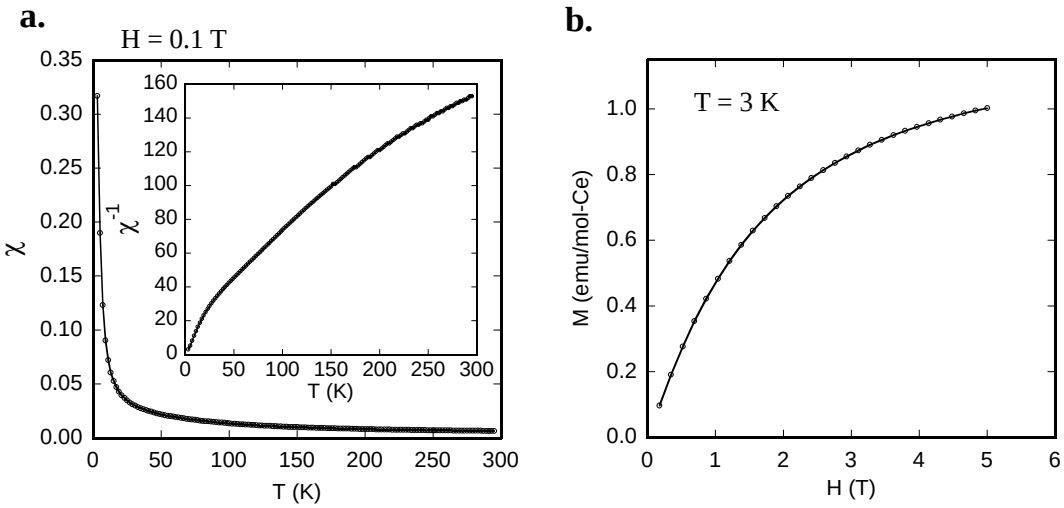

Figure 6.3 **a.** The temperature-dependent magnetic susceptibility of $ThSi_2$-type $CeAg_{0.01(1)}Si_{0.9(1)}Ga_{1.1(1)}$ indicates paramagnetic behavior down to 3 K. **b.** Field-dependent magnetization of $ThSi_2$-type $CeAg_{0.01(1)}Si_{0.9(1)}Ga_{1.1(1)}$ indicates weak antiferromagnetic interactions between Ce^{3+} moments.

phases and indicate that the incorporation of Ag into $ThSi_2$-type $CeSi_xGa_{2-x}$ phase has no significant effect on the physical properties of this phase.[14-15, 17, 28]

6.3.4 Structure and Magnetic Properties of AlB_2-type $CeAg_{0.01(1)}Si_{0.1(1)}Ga_{1.9(1)}$

The hexagonal AlB_2-type structure, shown in Figure 6.2b, can be described as distorted 6^3 networks of $^2_\infty[Ga_{1-x-y}Si_xAg_y]$ planar nets stacked along the *b*-axis with Ce atoms located in the hexagonal prismatic voids between them.[29] The *M* (*M* = Ag + Ga + Si) atoms are statistically distributed on the 2*d* (-6*m*2) site. The Ce-*M* interatomic distances (3.2849(7) Å) are longer than expected for covalently bonded Ce-*M* contacts (~ 2.8 Å), but the *M*-*M* interatomic distances (2.4639(7) Å) are consistent with covalently bonded *M*-*M* contacts (2.34 Å ≤ *M*-*M* ≤ 2.59 Å). The temperature-dependent magnetic susceptibility, χ, of single crystals from multiple growths were measured from 3 – 290 K at H = 0.1 T using a Quantum Design Physical Property Measurement System (PPMS) and indicates paramagnetic behavior down to 3 K as shown in

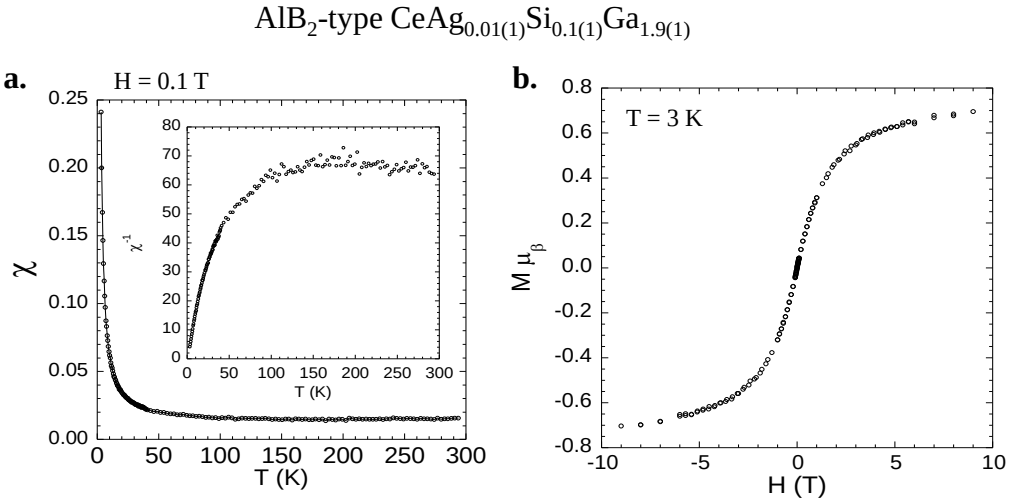

Figure 6.4 a. The temperature-dependent magnetic susceptibility of AlB_2-type $CeAg_{0.01(1)}Si_{0.1(1)}Ga_{1.9(1)}$ indicates paramagnetic behavior down to 3 K and the inverse magnetic susceptibility illustrates the tell-tale signs of intermediate valence of Ce moments. **b.** Field-dependent magnetization of AlB_2-type $CeAg_{0.01(1)}Si_{0.1(1)}Ga_{1.9(1)}$ indicates weak antiferromagnetic interactions between Ce moments.

Figure 6.4a. Above 50 K the inverse magnetic susceptibility data appear non-Curie- Weiss-like as shown in the in-set of Figure 6.4a. This behavior is consistent with intermediate valent Ce moments similar to the ferromagnetic Kondo behavior seen for $ThSi_2$- type $CeSi_2$[11-12] the superconducting AlB_2-type β-$YbAlB_4$,[30] and the superconducting AlB_2-type $YbSi_xGa_{2-x}$.[27] The susceptibility data were fit using a modified Curie-Weiss equation to determine the experimental μ_{eff} and the θ_W. The experimental μ_{eff} is 1.852(4) μ_B, which is approximately 30 % less than the expected effective moment for localized Ce^{3+} (2.54 μ_B), and the θ_W is 1.150(18) K. Since the χ_0 is on the same order of magnitude as the χ, the effective moment was also calculated from a plot of $(\chi-\chi_0)$ versus T to subtract out any diamagnetic contribution or temperature-independent contribution. The experimental μ_{eff} is 1.764(4) μ_B, which is approximately 30 % less than the expected effective moment for localized Ce^{3+} (2.54 μ_B), and the θ_W is 0.60(4) K. The field-dependent magnetization of single crystals was measured from 0 T – 9 T at 3 K. As shown in

Figure 6.4b the magnetization begins to saturate at 9 T with a maximum magnetization of ~ 0.7 μ_B which is approximately one third the expected spin-only saturation moment of Ce^{3+} moments (2.14 μ_B).

6.3.5 Valence Electron Counts and Phase Stability

Some conclusions on the phase stability of the AlB_2-type phase can be drawn regarding the number of available valence electrons per formula unit in a given compound. The structural stability of $Ln(M_{1-x}X_x)_2$ phases (*Ln* = lanthanide or alkaline earth metal; *M* = transition metal; *X* = main group metal) has been linked to the number of valence electrons available per formula unit in a given compound, with the AlB_2-type structure found for valence counts between 8.36 to 9.40 e^-/formula unit and valence electron counts ≥ 10 e^-/formula unit for the $ThSi_2$-type structure.[31] For the $Ce(Si_{1-y}Ag_y)_{2-n}$, $CeSi_{2-n}$, and $CeSi_{2-x}Ga_x$ phases, the AlB_2-type phases have been reported with valence electron counts from 9.0 to 9.6 e^- per formula unit and between 9.7 to 11.0 valence electrons per formula unit for the $ThSi_2$-type phases.[12, 14, 19, 32-33] One possible explanation for the apparent necessity of Si for the growth of the AlB_2-type in $CeAg_ySi_xGa_{2-x-y}$ phase involves the valence electron counts for the $CeAg_xGa_{2-x}$ phase. $CeAg_x,Ga_{2-x}$ ($0.5 \leq x \leq 1.0$) crystallizes in the $CeCu_2$-type structure and has a valence electron count of $7 \leq e^-$/formula unit ≤ 8,[20-21] which is less than the valence electron count observed for AlB_2-type phases. The growth and characterization of the $ThSi_2$- and AlB_2-type $CeAg_ySi_xGa_{2-x-y}$ phases illustrate the fact that serendipity means nothing without the presence of mind to recognize a gold mine.

6.3.6 Serendipity not Simplicity

With the discovery of intermediate valence in AlB_2-type $CeAg_{0.01(1)}Si_{0.1(1)}Ga_{1.9(1)}$ and consideration of the previously reported superconductivity of AlB_2-type $Yb(Ag,Ga)_2$,[22] we tried to grow the Yb-analogues of the $ThSi_2$- and AlB_2-type $CeAg_ySi_xGa_{2-x-y}$ phases. We started using

the same reaction conditions that led to the growth of the $ThSi_2$- and AlB_2-type $CeAg_ySi_xGa_{2-x-y}$ phases and systematically varied the reaction profile and reaction ratio. All attempts failed to produce crystals; the only products were not crystalline according to powder X-ray diffraction measurements. These proposed phases would have the same valence electrons/formula unit as the Ce-analogues, yet all attempts to grow crystals have failed. Interestingly, $YbSi_2$ crystallizes in the AlB_2-type structure, whereas $CeSi_2$ crystallizes in the $ThSi_2$-type structure.[11-12]

In conclusion, although valence electron counts are sometimes used as a rubric for determining phase stability, this convention is not always reliable. The factors affecting phase stability cannot be simplified by quantization of the available valence electrons/formula unit in a given structure-type, particularly in intermetallic phases. Intermetallic phases are intermediate between Zintl,[34] which exhibit large electronegativity differences between substituents and obey the octet rule, and Hume-Rothery phases,[35-36] which exhibit small electronegativity differences between substituents and abide by the valence electron counting convention. Intermetallic phases exhibit large electronegativity differences between substituents but behave as metals with delocalized available valence electrons. However, the determination of the available valence electrons of the transition metals in an intermetallic phase are not always straight-forward.[37] The absence of the $ThSi_2$- and AlB_2-type $YbAg_ySi_xGa_{2-x-y}$ phases is an example that serves to highlight the necessity of judicious exploration in inorganic materials. Combined experimental and theoretical efforts are necessary to better understand the factors that affect phase stability and ultimately move towards a more predictive approach to growing new materials.

6.4 References

(1) Menard, M. C.; Xiong, Y.; Karki, A. B.; Drake, B. L.; Adams, P. W.; Fronczek, F. R.; Young, D. P.; Chan, J. Y., Synthesis, structure, and characterization of $Ln_2Ag_{1-x}Ga_{10-y}$ (*Ln* = La, Ce). *J. Solid State Chem.* **2010,** *183*, 1935-1942.

(2) Menard, M. C.; Drake, B. L.; Thomas, K. R.; Hembree, R. D.; Karki, A.; Li, Y.; Young, D. P.; Ditusa, J.; Zhang, J.; Chan, J. Y., A tale of two polymorphs: growth and characterization of *α-Ln*$NiGa_4$ (*Ln* = Y, Gd-Yb) and *β–Ln*$Ni_{1-x}Ga_4$ (*Ln* = Tb-Er). *Eur. J. Inorg. Chem.* **2011,** *In Press.*

(3) Grin, Y.; Hiebl, K.; Rogl, P.; Eibler, R., Ternary gallides *RE*Ag_xGa_{4-x} (*RE* = La,Ce, Pr, Nd, Sm). *J. Less-Common Met.* **1986,** *115*, 367-372.

(4) Janssen, Y.; Angst, M.; Dennis, K. W.; McCallum, R. W.; Canfield, P. C., Differential thermal analysis and solution growth of intermetallic compounds. *J. Cryst. Growth* **2005,** *285*, 670-680.

(5) Egami, T.; Billinge, S. J. L., *Underneath the bragg peaks-structural analysis of complex materials*. 1st ed.; Elsevier: Oxford, **2003**; Vol. 7.

(6) Toby, B. H.; Egami, T.; Jorgensen, J. D.; Subramanian, M. A., Observation of a local structural change at T_c for $Tl_2Ba_2CaCu_2O_8$ by pulsed neutron diffraction. *Phys. Rev. Lett.* **1990,** *64*, 2414.

(7) Bozcaronin, E. S.; Billinge, S. J. L.; Kwei, G. H.; Takagi, H., Charge-stripe ordering from local octahedral tilts: underdoped and superconducting $La_{2-x}Sr_xCuO_4$ ($0 < x < 0.30$). *Phys. Rev. B* **1999,** *59*, 4445.

(8) Bozcaronin, E. S.; Kwei, G. H.; Takagi, H.; Billinge, S. J. L., Neutron diffraction evidence of microscopic charge inhomogeneities in the CuO_2 plane of superconducting $La_{2-x}Sr_xCuO_4$ ($0 < x < 0.30$). *Phys. Rev. Lett.* **2000,** *84*, 5856.

(9) Proffen, T.; DiFrancesco, R. G.; Billinge, S. J. L.; Brosha, E. L.; Kwei, G. H., Measurement of the local Jahn-Teller distortion in $LaMnO_{3.006}$. *Phys. Rev. B* **1999,** *60*, 9973.

(10) Louca, D.; Egami, T.; Brosha, E. L.; Roder, H.; Bishop, A. R., Local Jahn-Teller distortion in $La_{1-x}Sr_xMnO_3$ observed by pulsed neutron diffraction. *Phys. Rev. B* **1997,** *56*, R8475.

(11) Yashima, H.; Satoh, T.; Mori, H.; Watanabe, D.; Ohtsuka, T., Thermal and magnetic properties and crystal structures of $CeGe_2$ and $CeSi_2$. *Solid State Commun.* **1982,** *41*, 1-4.

(12) Dijkman, W. H.; Moleman, A. C.; Kesseler, E.; de Boer, F. R.; de Chatel, P. F., *$CeSi_2$: a new intermediate-valent compound*. North-Holland Publishing Company: Amsterdam, 1982.

(13) Burlet, P.; Frémy, M. A.; Gignoux, D.; Lapertot, G.; Quezel, S.; Regnault, L. P.; Rossat-Mignod, J.; Roudaut, E., Magnetic properties of the kondo lattice $CeGa_2$. *J. Magn. Magn. Mater.* **1987,** *63-64*, 34-36.

(14) Mori, H.; Sato, N.; Satoh, T., An electronically-driven volume transition in $CeSi_{2-x}Ga_x$. *Solid State Comm.* **1984,** *49*, 955-958.

(15) Moshchalkov, V. V.; Petrenko, O. A.; Semenov, M. V.; Lutsiv, R. V.; Babich, O. I., Effect of composition and pressure changes on the magnetic properties of Kondo lattices $CeSi_{2-x}Ga_x$. *Sov. J. Low Temp. Phys.* **1987,** *13*, 723-725.

(16) Moshchalkov, V. V.; Petrenko, O. A.; Zalyalyutdinov, M. K., The new Kondo lattice compounds: $CeSi_{2-x}Ga_x$. *Physica B* **1990,** *163*, 395-397.

(17) Dhar, S. K.; Pattalwar, S. M.; Vijavaraghavan, R., Structural and magnetic properties of $CeSi_{2-x}Ga_x$ alloys (x = 1.5, 1.75 and 2.0). *Solid State Comm.* **1993,** *87*, 409-411.

(18) Priolkar, K. R.; Pattalwar, S. M.; Mishra, P. K.; Raj, P.; Sathyamoorthy, A.; Dhar, S. K.; Sahni, V. C.; Sarode, P. R.; Prabhu, R. B., Structural and magnetic behavior of $CeSi_{0.6}Ga_{1.4}$. *Solid State Comm.* **1997,** *104*, 71-73.

(19) Cordruwisch, E.; Kaczorowski, D.; Rogl, P.; Saccone, A.; Ferro, R., Constitution, structural chemistry and magnetism in the ternary system Ce-Ag-Si. *J. Alloys Comp.* **2001,** *320*, 308-319.

(20) Adroja, D. T.; Rainford, B. D.; Malik, S. K., CeAgGa: a ferromagnetic Ce-based compound. *Physica B* **1993,** *186-188*, 566-568.

(21) Rossi, D.; Ferro, R., Ternary intermetallic *R*AgGa, *R*AuGa alloys (*R*=light rare earth and Yb). *J. Alloys Compd.* **2001,** *317-318*, 521-524.

(22) Tsujii, N.; Imai, M.; Yamaoka, H.; Jarrige, I.; Oohashi, H.; Tochio, T.; Handa, K.; Ide, J.; Atsuta, H.; Ito, Y.; Yoshikawa, H.; Kitazawa, H., Phase stability and superconducting properties of AlB_2-type $YbGa_xSi_{2-x}$ ($1.12 \leq x \leq 1.49$). *Chem. Mater.* **2010,** *22*, 4690-4699.

(23) Rossi, D.; Macciò, D., Ternary rare earth (*R*) alloys occurring in the RAg_2-RGa_2 section. *J. Alloys Compd.* **1998,** *281*, 222-227.

(24) Altomare, A.; Burla, M. C.; Camalli, M.; Cascarano, G.; Giacovazzo, C.; Guagliardi, A.; Polidori, G., SIR92 - a program for automatic solution of crystal structures by direct methods. *J. Appl. Crystallogr.* **1994,** *27*, 435.

(25) Sheldrick, G. M., A short history of SHELX. *Acta Crystallogr. Sect. A.: Found Crystallogr.* **2008,** *A64*, 112-122.

(26) Spek, A. L., PLATON, a multipurpose crystallographic tool. *J. Appl. Crystallogr.* **2003,** *36*, 7-13.

(27) Emsley, J., *The Elements*. 3rd ed.; Oxford University Press: New York, 1998.

(28) Priolkar, K. R.; Rao, M. N.; Prabhu, R. B.; Sarode, P. R.; Paranjpe, S. K.; Raj, P.; Sathyamoorthy, A., Inelastic neutron scattering in $CeSi_{2-x}Ga_x$ ferromagnetic kondo lattice compounds. *J. Phys.: Condens. Matter* **1998,** *10*, 10557-10564.

(29) Hofmann, W.; Jaeniche, W., Die struktur von aluminiumborid AlB_2. *Z. Phys. Chem. B.-Chem. E.* **1936,** *31* 214-222.

(30) Nakatsuji, S.; Kuga, K.; Machida, Y.; Tayama, T.; Sakakibara, T.; Karaki, Y.; Ishimoto, H.; Yonezawa, S.; Maeno, Y.; Pearson, E.; Lonzarich, G. G.; Balicas, L.; Lee, H.; Fisk, Z., Superconductivity and quantum criticality in the heavy-fermion system β-$YbAlB_4$. *Nat. Phys.* **2008,** *4*, 603-607.

(31) Haszko, S. E., Rare-earth gallium compounds having the aluminum-boride structure. *T. Metall. Soc. Aime.* **1961,** *221*, 201-202.

(32) Yashima, H.; Feng lin, C.; Satoh, T., Fluctuation effect at the magnetic transition of ferromagnetic dense kondo system. *Solid State Commun.* **1986,** *57*, 793-796.

(33) Yashima, H.; Satoh, T., Nonmagnetic-magnetic transition in Ce-Si system. *Solid State Commun.* **1982,** *41*, 723-727.

(34) Kauzlarich, S. M., *Chemistry, structure, and bonding of Zintl phases and ions*. VCH Publishers: New York, **1996**.

(35) Hume-Rothery, W.; Raynor, G. V., *The structure of metals and alloys*. Institute of Metal: London, **1962**.

(36) Hume-Rothery, W., *Phase stability in metals and alloys*. McGraw-Hill: New York, **1976**.

(37) Wallace, The solid state: intermetallic compounds. *Annu. Rev. Phys. Chem.* **1964,** *15*, 109-130.

APPENDIX. PERMISSIONS

Title: Crystal growth and properties of $Ln_2Ag_{1-x}Ga_{10-y}$ (Ln=La, Ce), a disordered variant of the Ce_2NiGa_{10}-structure type.

Author: Melissa C. Menard, Yimin Xiong, Amar B. Karki, Brenton L. Drake, Philip

W. Adams, Frank R. Fronczek, David P. Young, Julia Y. Chan

Publication: Journal of Solid State Chemistry

Publisher: Elsevier

Date: September 2010

Logged in as: Melissa Menard

Account #: 3000427189

Review Order: Please review the order details and the associated terms and conditions

Licensed content publisher: Elsevier

Licensed content publication: Journal of Solid State Chemistry

Licensed content title: Crystal growth and properties of $Ln_2Ag_{1-x}Ga_{10-y}$ (Ln=La, Ce), a disordered variant of the Ce_2NiGa_{10}-structure type.

Licensed content author: Melissa C. Menard, Yimin Xiong, Amar B. Karki, Brenton L. Drake, Philip W. Adams, Frank R. Fronczek, David P. Young, Julia Y. Chan

Licensed content date: September 2010

Licensed content volume number: 183

Licensed content issue number: 9

Number of pages: 8

Type of Use: reuse in a thesis/dissertation

Portion: full article

Format: both print and electronic

Title of your thesis/dissertation: EXOTIC GROUND STATES: A STUDY IN THE STRUCTURAL EFFECTS ON FRUSTRATION AND DIMENSIONALITY

Expected completion date: Aug 2011

Estimated size (number of pages): 115

Elsevier VAT number: GB 494 6272 12

Permissions price: 0.00 USD

Title: High-Resolution Synchrotron Studies and Magnetic Properties of Frustrated Antiferromagnets MAl_2S_4 ($M = Mn^{2+}$, Fe^{2+}, Co^{2+})

Author: Melissa C. Menard et al.

Publication: Chemistry of Materials

Publisher: American Chemical Society

Date: Jun 1, 2011

Logged in as: Melissa Menard

VITA

Melissa C. Menard was born Melissa A. Cormier on May 23, 1981, to parents, Joseph A. Cormier and Melynda A. Lamury in Opelousas, Louisiana. She is the second of three children and the only girl. Melissa graduated from Opelousas Catholic High School in May 1999. She then attended the University of Louisiana at Lafayette and received a Bachelor of Science degree in chemistry with honors on May 2005. After a two year hiatus Melissa came to her senses, married Wesley J. Menard on July 28th, and joined the solid state inorganic research group led by Dr. Julia Chan at Louisiana State University and Agricultural and Mechanical College in 2007.

While studying emergent phenomena in frustrated systems, Melissa attended several national and international scientific meetings. In December 2008, she attended the ICMR Winter School on New Carbon-based Materials and Functional Oxides in Bangalore, India. She presented a poster on the synthesis and characterization of disordered $Ln_2Ag_{1-x}Ga_{10-y}$ (*Ln* = La, Ce) compounds at the National American Chemical Society Meeting in Washington, D.C. In 2010 she presented a poster on the crystal growth of complex intermetallic compounds at the Inorganic Gordon Research Conference at the University of New England, Biddeford, Maine. 2011 was a very busy year with a poster presentation at the American Crystallographic Association Conference in May, the National School on Neutron and X-ray Scattering (NXS) in June, and the 22nd International Union of Crystallography Congress in Madrid, Spain, in August.

Melissa has received several awards including attendance and travel to the Winter School in India in 2008, travel and an invitation to speak at the American Crystallographic Association meeting in May 2011, attendance and travel to the NX school in June 2011, and a fellowship and an invitation to speak at the IUCr Congress in Madrid, Spain, in August 2011. Melissa has also served as a member of the American Chemical Society and the American Crystallographic

Association, served as a science fair judge at both local and state science fairs, and performed many chemical demonstrations at local schools.

Melissa will graduate on December 16, 2011, with a Doctor of Philosophy degree in chemistry. After graduation, she will continue research as a post-doctoral research associate under the guidance of Dr. Esther Takeuchi at the State University of New York at Buffalo.